NASA Contractor Report 4633

Experimental Study of Vane Heat Transfer and Aerodynamics at Elevated Levels of Turbulence

Forrest E. Ames
Allison Gas Turbine
Indianapolis, Indiana

Prepared for
Lewis Research Center
under Contract NAS3–25950

National Aeronautics and
Space Administration
Office of Management
Scientific and Technical
Information Program
1994

Table of Contents

Table of Contents iii
List of Figures v
List of Tables viii
Nomenclature ix
Summary 1

Chapters
1. Introduction 2
   Background 3
   Implications for Heat Transfer 4
2. Experimental Apparatus and Baselining 6
   Facility Description 6
   Turbulence Generators 7
   Pressure Vane Description 8
   Heat Transfer Vane Description 8
   Data Acquisition and Reduction 9
   Data Uncertainties 10
3. Inlet Conditions 25
   Inlet Velocity 25
   Inlet Turbulence 26
   One Dimensional Power Spectra 27
   Turbulent Scales 28
4. Heat Transfer Results 39
   Baseline Results 39
   Stanton Number Results 39
   Heat Transfer Augmentation 42
   Conclusions 42
5. Intrapassage Turbulence 47
   Experimental Measurements 47
   Turbulence Measurements 48
   Summary and Conclusions 51
6. Exit Measurements 67
   Wake Losses 67
   Wake Growth Estimates 69
   Turbulence Parameters 70
   Wake Mixing 71
   Conclusions 73
7. Summary and Conclusions 87
   Inlet Turbulence Characteristics 87
   Heat Transfer 87

Intrapassage Turbulence 88
Wake Characteristics and Development 88
References 90
Appendix A.1 Inlet Turbulence Characteristics 93
Appendix A.2 Vane Pressure Distributions 94
Appendix A.3 Heat Transfer Distributions 103

List of Figures

2.1 Schematic of four vane C3X cascade 16
2.2 C3X vane geometry as setup in cascade 17
2.3 Cascade inlet setup for grid and low turbulence configurations 18
2.4 Schematic of biplanar square mesh grid 19
2.5 Cascade inlet setup for combustor in close position 20
2.6 Schematic of combustor turbulence generator 21
2.7 C3X vane pressure tap locations 22
2.8 Comparison of measured and predicted pressure profile for low turbulence case, Ma_{ex} = 0.27 22
2.9 C3X vane thermocouple locations 23
2.10 C3X vane finite element mesh for conduction analysis 23
2.11 Comparison of baseline heat transfer test with STAN7 calculation, Re_{ex} = 780,000, Ma_{ex} = 0.27 24
3.1 Comparison of total pressure inlet velocities for the four turbulence conditions 30
3.2 Circumferential distribution of inlet velocity based on static pressure Ma_{ex} = 0.27 30
3.3 Comparison of inlet velocity profiles for the four turbulence conditions based on total pressure, U_∞ = 30 m/s 31
3.4 Comparison of inlet turbulence level for the four conditions, U_∞ = 30 m/s 31
3.5 Cross span survey of turbulence components, Comb(1), U_∞ = 30 m/s ... 32
3.6 Cross span survey of turbulence components, Comb(2), U_∞ = 30 m/s ... 32
3.7 Cross span survey of turbulence components for grid, U_∞ = 30 m/s 33
3.8 Cross span distributions of v'^2/v'^2_∞ showing near wall attenuation, U_∞ = 30 m/s 33
3.9 Cross span distributions of v'^2/v'^2_∞ versus y/Lu_∞ showing near wall attenuation, U_∞ = 30 m/s 34
3.10 One dimensional spectra of u' and v' components for Comb(1) showing inertial subrange isotropy, U_∞ = 30 m/s 35
3.11 One dimensional spectra of u' and v' components for Comb(2) showing inertial subrange isotropy, U_∞ = 30 m/s 36
3.12 One dimensional spectra of u' and v' components for grid showing inertial subrange isotropy, U_∞ = 30 m/s 37
3.13 Comparison of v' spectra for various Y showing low wavenumber attenuation, Comb(1) 38
4.1 Comparison of baseline heat transfer test with STAN7 calculation, Re_{ex} = 780,000, Ma_{ex} = 0.27 43
4.2 Comparison of Stanton number distributions showing effects of turbulence, Re_{ex} = 790,000 43

4.3 Comparison of Stanton number distributions showing effects of turbulence, Re_{ex} = 510,000 44

4.4 Influence of turbulence on heat transfer augmentation, Re_{ex} = 790,000. 44
4.5 Influence of turbulence on heat transfer augmentation, Re_{ex} = 510,000. 45
4.6 Influence of Reynolds number on heat transfer augmentation, Comb(1).. 45
4.7 Comparison of absolute level of heat transfer augmentation, Re_{ex} = 790,000 46
4.8 Comparison of absolute level of heat transfer augmentation, Re_{ex} = 510,000 46
5.1 Schematic of cascade showing locations of intrapassage and exit measurements 55
5.2 Intrapassage single wire velocity measurements at survey locations through 4 56
5.3 Intrapassage distribution of u' at locations 1 through 4, Comb(1) 56
5.4 Intrapassage distribution of u' at locations 1 through 4, Comb(2) 57
5.5 Intrapassage distribution of u' at locations 1 through 4, Grid 57
5.6 Development of u' spectra through turbine passage for Comb(1) 58
5.7 Intrapassage distribution of v' at locations 1 through 4 for Comb(1) 59
5.8 Intrapassage distribution of v' at locations 1 through 4 for Comb(2) 59
5.9 Intrapassage distribution of v' at locations 1 through 4 for grid 60
5.10 Comparison of v' distributions at location 1 60
5.11 Comparison of v' distributions at location 4 61
5.12 Development of v' spectra through turbine passage for Comb(1) 62
5.13 One dimensional spectra of u' and v' components for Comb(1) at position 1 showing inertial subrange isotropy, U = 27.4 m/s 63
5.14 One dimensional spectra of u' and v' components for Comb(1) at position 4 showing significant anisotropy, U = 90.3 m/s 64
5.15 Comparison of near wall distributions of v'^2/v'^2_∞ at position 2 65
5.16 Comparison of near wall distributions of v'^2/v'^2_∞ versus y/Lu_∞ at position 2 65
5.17 One dimensional v' spectra at various Y, position 2, Comb(1) 66
6.1 Comparison of exit total pressure loss surveys, position 6, Ma_{ex} = 0.27 81
6.2 Comparison of exit total pressure loss surveys, position 8, lower wake, Ma_{ex} = 0.27 81
6.3 Comparison of exit total pressure loss survey taken, position 8, upper and lower wakes, Ma_{ex} = 0.27 82
6.4 Comparison of single wire wake profiles, position 6, Ma_{ex} = 0.27 82
6.5 Comparison of single wire wake profiles, position 8, Ma_{ex} = 0.27 83
6.6 Comparison of X wire |u'| distributions, position 6, Ma_{ex} = 0.27 83
6.7 Comparison of v' distributions, position 6, Ma_{ex} = 0.27 84
6.8 Comparison of X-wire |u'| distributions, position 8, Ma_{ex} = 0.27 84
6.9 Comparison of v' distributions, position 8, Ma_{ex} = 0.27 85

6.10 Comparison of exit shear stress distributions, position 6, Ma_{ex} = 0.27.. 85
6.11 Comparison of exit shear stress distributions, position 8, Ma_{ex} = 0.27.. 86

List of Tables

2.1	Exit/Passage Traverse Access Coordinates	12
2.2	C3X Vane Coordinates	12
2.3	C3X Vane Pressure Tap Locations	14
2.4	C3X Vane Thermocouple Locations	15
3.1	Inlet Velocity Profile Parameters	29
5.1	Intra Passage Turbulence Data for Position 1	53
5.2	Intra Passage Turbulence Data for Position 2	53
5.3	Intra Passage Turbulence Data for Position 3	54
5.4	Intra Passage Turbulence Data for Position 4	54
6.1a	Exit Loss Parameters, Position 6	75
6.1b	Exit Loss Parameters, Position 8	76
6.2	Wake Growth Analysis for Single Wire Data	77
6.3a	Turbulence Characteristics at Position 6	78
6.3b	Turbulence Characteristics at Position 8	79
6.4	Wake Mixing and Turbulence Parameters	80

Appendices

A.1	Inlet Turbulence Characteristics	93
A.2	Vane Static Pressure Distributions	94
A.3	Vane Heat Transfer Distributions	103

Nomenclature

a	distance from trailing edge tip to origin of wake, see eqn. 6.1
C	airfoil chord length
Cd	drag coefficient, Cd = Drag/(ρ U_∞^2 A), A = projected area
Cf/2	skin friction coefficient, Cf/2 = $\tau 0/(\rho\ U_\infty^2)$
Cp	specific heat at constant pressure
CL	cross stream distance, CL = s cos(α_2)
d	trailing edge diameter
D	leading edge diameter
$\bar{e}$	mass averaged kinetic energy loss coefficient
$\bar{e}_1$	local kinetic energy loss coefficient
$\bar{e}_2$	mixed out kinetic energy loss coefficient
$E_1(k_1)$	one dimensional energy spectrum of u', $E_1(k_1) = U_\infty E_1(f)/2/\pi$
$E_2(k_1)$	one dimensional energy spectrum of v', $E_2(k_1) = U_\infty E_2(f)/2/\pi$
f	frequency, 1/s
K	thermal conductivity
k_1	wavenumber, $k_1 = 2\ \pi\ f/U_\infty$
l	a mixing length, ν_m/v'
L	an unspecified turbulent length scale
Lu	energy scale, Lu = 1.5 $\lvert u' \rvert^3/\varepsilon$
Lx	longitudinal integral scale
Ly	lateral (normal to the surface) integral scale
Ma_{ex}	Mach number based on exit conditions
Nu	Nusselt number, Nu = hD/K
omega	total perssure loss coefficient, $(Pt_{in}-Pt_{ex})/(Pt_{in}-Ps_{ex})$, also ω
P	pressure
Ps	static pressure
Pt	total pressure
Q	surface heat flux boundary condition
Re	Reynolds number
$Re_{\delta 2}$	momentum thickness Reynolds number, $Re_{\delta 2} = \rho_\infty U_\infty \delta 2/\mu$
Re_{ex}	exit Reynolds number, $Re_{ex} = \rho_{ex} U_{ex} C/\mu$
Re_λ	Taylor's Reynolds number, $Re_\lambda = \rho\ u'\lambda/\mu$
s	vane spacing
St	Stanton number, $h/(\rho\ U\ Cp)$
St_0	low turbulence case Stanton number
T	temperature
Tt	stagnation temperature
Tu	turbulence intensity, Tu = u'/U_∞
Tuv	normal component turbulence intensity, Tuv = v'/U_∞
Tu_0	turbulence level at reference position

Nomenclature (Continued)

Tuv	normal component turbulence intensity, Tuv = v'/U_∞
Tu_0	turbulence level at reference position
U	streamwise velocity
u'	RMS streamwise fluctuation velocity
v'	RMS normal fluctuation velocity (normal to streamwise velocity and generally normal to vane surface
w'	RMS spanwise fluctuation velocity
W	width of the wake determined from the locations where the velocity equals one half the peak velocity defect, cm
x	streamwise distance along the airfoil
X_1	distance between the probe tip and the vane tailing edge
Y	normal distance from the vane surface
Z	cross span distance from the endwall

Greek Symbols

α_2	vane turning angle, degrees
δ_1	displacement thickness, $\delta_1 = \int_0^\infty (1 - \rho U/\rho_\infty U_\infty)\, dy$
δ_2	momentum thickness, $\delta_2 = \int_0^\infty \rho U/\rho_\infty U_\infty (1 - \rho U/\rho_\infty U_\infty)\, dy$
δ_3	energy thickness, $\delta_3 = \int_0^\infty \rho U/\rho_\infty U_\infty [1 - \rho U^2/\rho_\infty U_\infty^2)\, dy$
ε	turbulent dissipation
λ	lateral dissipation scale or Taylor microscale, $\lambda = (15\, \nu\, u'^2/\varepsilon)^{1/2}$
μ	dynamic viscosity
ν	kinematic viscosity
ν_m	eddy diffusivity
σ	distance from the wake centerline to location where Udefect = exp(-1) $U_{max,def}$, cm
τ	turbulent time scale, Lu/u'
τ_0	wall shear stress
ω	total perssure loss coefficient, $(Pt_{in}-Pt_{ex})/(Pt_{in}-Ps_{ex})$, also omega
$\overline{\omega}$	mass averaged total pressure loss coefficient

Subscripts

∞	references to free stream conditions
core	average value in region unaffected by wall or wake
in	references to inlet static pressure tap plane location
ex	references to exit static pressure tap plane location

Summary

A four vane subsonic cascade was used to investigate how free stream turbulence influences pressure surface heat transfer. A simulated combustor turbulence generator was built to generate high level (13%) large scale (Lu ≈ 44% inlet span) turbulence. The mock combustor was also moved upstream to generate a moderate level (8.3%) of turbulence for comparison to smaller scale grid generated turbulence (7.8%). The high level combustor turbulence caused an average pressure surface heat transfer augmentation of 56% above the low turbulence baseline. The smaller scale grid turbulence produced the next greatest effect on heat transfer and demonstrated the importance of scale on heat transfer augmentation. In general, the heat transfer scaling parameter $U_\infty Tu_\infty Lu_\infty^{-1/3}$ was found to hold for the turbulence. Heat transfer augmentation was also found to scale approximately on $Re_{ex}^{1/3}$ at constant turbulence conditions.

Some evidence of turbulence intensification in terms of elevated dissipation rates were found along the pressure surface outside the boundary layer. However, based on the level of dissipation and the resulting heat transfer augmentation, the amplification of turbulence has only a moderate effect on pressure surface heat transfer. The flow field turbulence does drive turbulent production within the boundary layer which in turn causes the high levels of heat transfer augmentation.

Unlike heat transfer, the flow field straining was found to have a significant effect on turbulence isotropy. On examination of the one dimensional spectra for u' and v', the effect to isotropy was largely limited to lower wavenumber spectra. The higher wavenumber spectra showed little or no change.

The high level large scale turbulence was found to have a strong influence on wake development. The free stream turbulence significantly enhanced mixing resulting in broader and shallower wakes than the baseline case. High levels of flow field turbulence were found to correlate with a significant increase in total pressure loss in the core of the flow. Documenting the wake growth and characteristics provide boundary conditions for the downstream rotor.

Chapter 1

Introduction

Since the gas turbine industry began cooling turbine components in the early 60's, a large effort has been spent on understanding and predicting surface heat loads on turbine components. While significant progress has been made, the uncertainties in the prediction of vane and blade surface heat loads remain large. In order to produce satisfactory cooling schemes, heat transfer designers are forced to either overcool components, resulting in elevated losses, or iterate on the design over several costly development cycles.

Part of the problem, until recently, has been the failure to fully comprehend the aggressive and complex environment turbine surfaces are subjected to. Flow features such as high levels of combustor and airfoil wake generated turbulence, hot streaks, and secondary flows all contribute to the difficulty in assessing gas path heat loads. Unfortunately, very few studies exist where these features have been studied and comprehensively documented. Consequently, very few heat transfer programs have included relevant and extensively documented inlet conditions as variables in their studies.

One particularly troublesome area in gas turbines is predicting the heat load on the pressure surface of an airfoil. Combustor and wake generated turbulence contributes heavily to the enhancement of film coefficients and the dissipation of film cooling protection. Current predictive schemes do not have turbulent closure models which can model the changes to turbulence near surfaces or in flow fields with high strain rates. In order to develop more accurate predictive capabilities, we must more closely define flow field inlet conditions and more closely model the response of turbulence in turbine flow passages.

In this present study, a range of engine relevant turbulence levels and scales has been generated and the resulting heat transfer to a vane in a linear cascade has been documented. The inlet, intrapassage, and exit flow field and turbulence characteristics have been determined using hot wire anemometry. Unlike previous studies, a combustor-like turbulence generator was used to produce the turbulence in order to approximate the large scale, high intensity turbulence typical of a gas turbine combustor. Additionally, a grid has also been used to generate turbulence in order to demonstrate the effect of scale on heat transfer and aerodynamics.

Background

One of the primary objectives of this study is to gain a better understanding of how turbulence drives the heat transfer process. Turbulence has been found to have a strong effect on stagnation region and pressure surface heat transfer. A recent vane heat transfer study at the von Karman Institute in Belgium [1] found a one hundred percent increase in heat transfer on the laminar portion of the pressure surface with a six percent turbulence level. Yet, turbulence levels at the entrance to turbine nozzles can be much higher than six percent. Bicen and Jones [2] measured turbulence levels, based on the bulk exit velocity, ranging from 13 to 20 percent using a model can-type combustor. Ames and Moffat [3] measured turbulence levels ranging from 15 to 17 percent at the exit of a mock combustor with energy scales, ($Lu = 1.5\ |u'|^3/\varepsilon$) ranging from 33 to 50 percent of the exit height.

Turbulence level alone is not adequate to predict boundary layer heat transfer. Ames reported heat transfer augmentation levels of around 12 percent and less at the entrance region of his heat transfer surface where the turbulence level was 15 to 17 percent. Conversely, Maciejewski and Moffat [4] reported Stanton numbers 80 percent higher than values of a turbulent correlation on a test plate intersecting the flow from a free jet where the turbulence level was 15 percent.

The normal component of turbulence is strongly attenuated at a solid surface and this interaction has great influence in the resulting heat transfer. Hunt and Graham [5] calculated the effect of a wall on isotropic turbulence. They found the normal variance, v'^2, of turbulence attenuated as a function of y/Lx to the two thirds power as the wall was approached and the lateral integral scale, Ly, varied with the distance to the wall. Thomas and Hancock [6] measured the distributions of spectra and variances for grid turbulence near a moving wall in a wind tunnel. The results of Thomas' experiments agree well with Hunt's calculations. From a physical standpoint, the turbulent eddies which are large compared to the distance from the wall are blocked by the presence of the wall. This blocking action causes a reduction in v' and the lateral scale of turbulence normal to the wall. The redirected momentum from v' causes a corresponding increase in the u' and w' components of turbulence near the wall.

For turbulence scales large in comparison to the boundary layer this blocking of v' can begin well outside the boundary level. Ames measured strong attenuation of v' in the flow downstream from a mock combustor. This blocking of v' began well outside the relatively thin boundary layers and continued into the boundary layer until near wall production began to contribute significantly to the v' profile. Ames attributed the low heat transfer augmentation at the beginning of his test surface to the large turbulent scale to boundary layer thickness ratios. Ames was able to correlate his

---

* Superscript numbers refer to references on pages 90 through 92.

data and Blair's [7,8] as a function of turbulence level, energy scale (Lu), and enthalpy thickness Reynolds number. Earlier, Hancock and Bradshaw [9] were able to correlate turbulent boundary layer skin friction as a function of turbulence level and energy scale (Lu). Scale has an important influence on turbine heat transfer since typical turbulence scales are much larger than boundary layer thicknesses.

Scale as well as turbulence level is also important in assessing stagnation region heat transfer. Ames and Moffat [3] determined the stagnation region heat transfer for 3 different diameter constant temperature cylinders at the exit of a mock-combustor. The turbulent scale, Lu, was large in comparison with the cylinder diameters and their data fell well below standard correlations for stagnation region heat transfer (Kestin and Wood [10], Lowery and Vachon [11]). Within their data they found a definite influence of scale on stagnation region heat transfer. They developed a correlation parameter for large scale turbulence based on a simple analysis.

$$Nu/Re_D^{1/2} = f\{Tu*(Lu/D)^{-1/3}*Re_D^{5/12}\}$$

Ames and Moffat were able to correlate their own data and the data of Lowery and Vachon [11] and Smith and Kuethe [12] based on their correlating parameter. Van Fossen and Simoneau [13] and Van Fossen and Ching [14] studied the effect of integral scale, Lx, on stagnation region heat transfer to an elliptical and a cylindrical leading edge. Van Fossen used 5 grids, four square mesh and one wire grid, to generate a range of scales to cylinder diameter ratios. His results ranged from well above Lowery and Vachon's correlation to well below it. Van Fossen was able to correlate his data empirically based on a turbulence level, Reynolds number, and length scale to diameter ratio parameter. His data correlated within +/- 4 percent based on this parameter, except for his wire grid which fell above it. He attributed this difference to the anisotropy of the wire grid turbulence.

Hunt [15] studied the situation of turbulence approaching a cylinder using an analysis based on rapid distortion theory. He found that turbulent eddies smaller than the cylinder diameter were generally amplified by the high strain rates near the cylinder while eddies large in comparison with the cylinder diameter were blocked by the cylinder's presence. Britter, Hunt, and Mumford [16] measured turbulence approaching a cylinder and their results largely confirm Hunt's earlier results.

Implications for Heat Transfer

The studies reviewed in the background section of this report evidenced the influence of turbulence on heat transfer. Turbulence can strongly enhance laminar heat transfer to a cylindrical stagnation region, the pressure surface of an airfoil, transition, and turbulent boundary layer heat transfer. Turbulence behaves differently near a

cylindrical leading edge than it does adjacent to a flat plate. The scale or spectrum of turbulence energy is a characteristic which has an important influence on the effect of turbulence. These studies point to the idea that we need to study the characteristics of turbulence generated in a gas turbine. Both combustor generated turbulence and wake turbulence significantly alter heat transfer and flow development in a turbine. There exists a need to study the influence of combustor and wake-like turbulence on turbine airfoil and endwall heat transfer. Also, in order to be able to predict the influence of this turbulence on heat transfer, we need to study its evolution through turbine passageways and near component surfaces.

The general objective of the present study was to investigate the influence of combustor like turbulence on turbine vane heat transfer. In this study, two levels of combustor like turbulence and one level of grid turbulence were generated and carefully characterized. The resulting heat transfer to a modern vane was then determined. The development of the flow and turbulence through the passageway was then characterized. Finally, the turbulence characteristics and growth of the downstream wake was investigated.

Chapter 2

Experimental Apparatus and Baselining

The experimental apparatus used in this investigation as well as the data acquisition and reduction procedures are documented in this section. This chapter provides detailed information on the geometry of the cascade, vanes, turbulence generators, and heat transfer apparatus. The data acquisition and data reduction procedures are overviewed. This section is intended to provide enough detail on the cascade geometry and the quality of the data to allow use of this data for predictive assessment.

Facility Description

The four vane cascade used in this study is connected to an in draft blower. The blower is rated at 1.13 m^3/s (2400 SCFM) with a pressure rise of 10.34 kPa (1.5 psia). The Plexiglas walled cascade was originally built by Zimmerman [17] for three component laser anemometer measurements. The cascade was modified for the present experiments to allow for access with hot wire anemometry probes and pressure probes. A schematic of the cascade is shown in figure 2.1. The cascade uses four, 4.5 times scale, C3X, vanes. The vanes are a two dimensional slice from a design for a helicopter engine. This vane geometry was previously used by Nealy, et. al. [18], for measurements of heat transfer distributions in a warm cascade rig. The present cascade has a row of 9 inlet static pressure taps spanning two vane passages at 3.68 cm upstream from the inlet plane of the vanes to monitor inlet flow uniformity. In addition, the cascade has a row of exit static pressure taps to monitor exit flow periodicity. The inlet flow uniformity was controlled using the upper and lower bleed flow adjustments. The exit periodicity was set up using the upper and lower tailboards. The probe access ports, which are labelled 1 through 8, accommodated a 14.73 cm long probe used to traverse across the turbine passage and the exit. This probe was pivoted about the access ports using a slider linkage on a lead screw drive table. The location of the probe access points or pivot points is given in table 2.1 and is referenced to the lower right hand corner of figure 2.1. The position numbers referenced in table 2.1 relate to the numbers written over the pivot points in figure 2.1. The inlet access ports, which are also labeled 1 through 8, accommodated inlet total pressure, temperature, and hot wire probes used to reference and survey the inlet conditions. These ports are located 3.68 cm upstream from the vane leading edge plane and are spaced four to a passage.

The vane geometry is shown in figure 2.2 and the coordinates are given in table 2.2. The coordinates in table 2.2 are taken from reference 18 and need to be rotated

180 degrees to have the same orientation as shown in figure 2. The columns labelled arc refer to distance along the surface of the vane from the stagnation point in the direction of the suction surface. This vane has a true chord length of 14.493 cm and an axial chord of 7.816 cm. With a vane spacing of 11.773 cm the passage has a 3.292 cm throat. The calculated air exit angle is 72.38 degrees and the vane height is 7.62 cm. The leading edge diameter of the vane is 2.336 cm and the trailing edge diameter is 0.346 cm. The stagger angle is 55.47 degrees.

Turbulence Generators

Four inlet turbulence boundary conditions were developed for this study. The conditions consisted of a low turbulence base case, a grid generated turbulence case, and two cases with simulated combustor turbulence. Figure 2.3 shows the inlet geometry for the grid generated turbulence. The inlet consisted of an inlet filter to remove dust from the air, two nylon screens to reduce the inlet velocity fluctuations, an eight to one 2-D contraction nozzle to reduce the level of streamwise turbulence intensity, and a 25.4 cm long, rectangular section which held the grid. The rectangular section is connected to the cascade.

A schematic of the biplanar grid as assembled in the rectangular spool section is shown in figure 2.4. The grid was made from 0.125 inch (0.317 cm) square steel bars. The spacing in the spanwise direction is 0.6 inches (1.524 cm) and the spacing up and down is 0.625 inches (1.588 cm) producing a 63 percent open area grid. Three of the spanwise bars are a quarter of an inch (0.635 cm) longer on each end. These long bars stick into plugs to secure the grid in place.

The grid was positioned 12.7 cm upstream from the cascade inlet to document the inlet turbulence characteristics at 16 cm downstream from the grid. In the forward position, 8.89 cm upstream from the cascade inlet, the grid was 15.89 cm upstream from the inlet plane of the vanes. The grid was in this position for the remainder of the heat transfer and aerodynamic tests.

The baseline or low turbulence geometry is similar to the grid geometry. The grid is removed for the low turbulence geometry and solid plugs are installed at the grid plane. The first test section configuration with the simulated combustor is shown in figure 2.5. The combustor is attached directly to the inlet plane of the cascade. The flow conditioning screens are not used in this configuration and the air filter section is connected directly to the inlet of the combustor simulator.

A schematic of the simulated combustor is shown in figure 2.6. The overall length of the turbulence generator is 45.72 cm. The inlet of the simulator is 59.06 cm wide by 42.54 cm high. Air flow is directed from the inlet plenum through the rear and side panels of the simulator liner. Flow through the rear slots combines with flow

through the first row of holes in the side panel to create a recirculation zone inside the simulator liner. The second row of holes in the side panels simulate dilution jets. The simulator takes a two to one contraction from the liner into the inlet of the cascade through a 15.24 cm long nozzle.

The second test section configuration with the simulated combustor is similar to the first except the 25.4 cm long rectangular spool section is inserted between the combustor simulator and the cascade inlet. This distance gives the turbulence in the flow sufficient time to decay to a level similar to that of the grid generated turbulence. However, the combustor simulator has a scale significantly larger than the grid generated turbulence.

Pressure Vane Description

A schematic of the vane used to measure the surface pressure distribution is shown in figure 2.7. The locations of the tubes used for the static pressure taps are indicated by the symbols. The nylon tubes were cast into the vane and static taps were located by drilling through the surface into the tubes. The surface location of the static taps are given in table 2.3 both in terms of X and Y coordinates and also in terms of surface distance. The stagnation point is located between taps 17 and 18.

The baseline pressure distribution for the low turbulence case is given in figure 2.8. The measured pressure distribution, shown with symbols, is compared to a prediction based on an unpublished stream function formulation for compressible flow. In general, the comparison looks quite favorable. The experimentally determined stagnation point is located between the 17th and 18th static pressure tap. The figure shows 18 taps before the stagnation point because the tap on the trailing edge is included on the pressure side rather than the suction side.

Heat Transfer Vane Description

A schematic of the vane used for the heat transfer measurements is shown in figure 2.9. The locations of the thermocouples used for surface temperature measurement are indicated by the symbols. Table 2.4 gives the locations of the thermocouples in terms of X and Y coordinates and in terms of surface distance. The fine gauge chromel - alumel thermocouples were cast into the vane. Not shown on the figure is the 0.025 mm thick Inconel foil used to generate the constant heat flux on the vane. The heating started at an X location of 1 cm on the pressure surface and ended at an X location of 1.45 cm on the suction surface. Prior to the beginning of heating, the foils were connected to a 0.254 mm thick and 6.35 mm wide bus bar using resistance welding. A shallow indentation was milled in the airfoil surface to accommodate the bus bars. The Inconel foil was bonded to the outside of a 0.127 mm Kapton backing material. The Kapton was adhered to the airfoil surface using a high temperature

acrylic adhesive. The resulting foil surface on the vane was aerodynamically smooth and visually attractive.

A finite element analysis (FEA) was made for the epoxy vane in order to reduce the uncertainty in the surface heat flux and temperature due to conduction through the vane. The surface normal heat flux determined from analysis is added to the flux dissipated in the foil. The calculated surface normal heat flux due to conduction is also used to correct for the difference between the measured temperature in the outer surface of the epoxy and the surface temperature. The mesh used for the calculation is shown in figure 2.10. The mesh is 29 elements by 8 elements and was set up on a commercial spread sheet.

A heat transfer baselining test was conducted at the low turbulence condition. The procedure included running the test without heating to obtain the recovery temperatures along the vane. Next, the test was conducted with the vane heated. The heated case surface temperatures were input into the finite element analysis. The FEA analysis provided the extra surface normal heat flux due to conduction through the epoxy vane and the surface temperature which was extrapolated from the vane thermocouples. The heat transfer coefficient was determined from the net surface heat flux and the surface-to-recovery temperature difference. The net heat flux was determined from the foil heat flux plus the conduction heat flux less the radiation heat flux. The radiative heat flux was estimated by assuming the foil had an emissivity of 0.2 and was radiating to a black body with a temperature equal to the inlet temperature. The maximum estimate for radiative loss amounted to about 1.8 percent of the local heat flux.

A comparison between the experimentally determined heat transfer coefficient and a heat transfer coefficient determined from the measured pressure distribution and a finite difference boundary layer calculation (STAN7 [19]) is shown in figure 2.11. The comparison on the pressure surface and the laminar part of the suction surface is excellent. The start up at the stagnation point is a little off and is probably due to the difference between the actual velocity and temperature distributions and the ones input into the boundary layer code. On the suction surface, as the boundary layer develops along the adverse pressure gradient, the code calculates boundary layer separation and cannot continue. The calculated point of separation appears to be near the point where the vane has a laminar separation and then transitions. This comparison between the calculated and predicted heat transfer coefficients along the vane gives confidence in the experimental method.

Data Acquisition and Reduction

This experiment used a PC based data acquisition system. Pressure measurements were made using a Scanivalve and two -- 6.89 kPa pressure transducers

calibrated against an Ametek dead weight tester. Steady state voltage signals were read using an HP 3456A digital multimeter with 100 nanovolt sensitivity and 2.5 microvolt accuracy. Signals were multiplexed using an HP 3497A scanner. The pressure and hot wire probes were traversed using two Unislide lead screw drive tables and an Anahiem Automation stepper motor controller. The hot wire signals were collected using an Analog Devices RTI-860 board with simultaneous sample and hold capability and a 200 kHz throughput (50 kHz per channel in simultaneous mode). The hot wires were powered with two DISA 55M system constant temperature anemometer bridges. The hot wire signal was zeroed and amplified to take advantage of the full 12 bit resolution of the data acquisition card. The probes were calibrated against a low free stream turbulence jet and the calibration was fit to a fourth order polynomial. Jorgensen's decomposition (see Frota [20]) was used to determine the instantaneous velocity vector. For exit measurements with the X-wire, two 20 kHz active low pass filters were used to eliminate the possibility aliasing.

Pressure and thermocouple voltages were read 10 or more times for each data point using an integrating voltmeter. For mean measurements single wire voltages were read 16,384 times at each point at intervals of two or more time constants. Mean X-wire measurements were determined from 8192 independent points. Velocity time records for determining power spectra for both the single wire and X wire were determined from 40 records of 8192 points. Power spectra were calculated for each of the 40 records and then averaged. Dissipation was estimated by fitting a -5/3 slope line through the power spectra in the region of the inertial subrange using the following relationship.

$$E1(k1) = 18/55\ A\ \epsilon^{2/3}\ k_1^{-5/3}$$

Where the constant A is taken as 1.62 for consistency with reference 3. The energy scale is defined as $Lu = 1.5\ |u'|^3/\epsilon$ similar to Hancock and Bradshaw[9] but using the dissipation estimated from the inertial subrange of the spectrum. By defining the dissipation in this manner, the energy scale has a clear relationship with the power spectra.

Data Uncertainties

The data uncertainties were estimated based on the root mean square method (see Kline and McClintok [21]). Determination of total pressure resulted in an absolute uncertainty of about one percent at the inlet and about 0.25 percent at the exit. Determination of the velocity from the pressure at the inlet and exit had an uncertainty of about two percent due to the uncertainty in the local static pressure. The mean velocity as determined by single wire anemometry had an uncertainty of about two percent. The single largest source of uncertainty in U was due to room temperature variations which could range by as much as 9.5 degrees C during some days. The response of the hot wire due to this temperature change was compensated for. The

change in anemometer voltage due to the variation in the electronics temperature was not compensated for. The uncertainty in the turbulence level determined from the single wire was estimated to be about 3 percent. The X-wire velocity had an uncertainty of about 3 percent due to both random fluctuations, room temperature variation, and errors due to binormal fluctuations (w') combined with the probe angle of attack (see Wubben, [22]). The estimated uncertainty in u' and v' was four percent for the X-wire at relatively low angles of attack (less than 7 degrees), increasing for greater values. The estimated uncertainty in the Reynolds shear stress $-\overline{u'v'}$, ranged from +/- 0.03 * |u'| * |v'| to +/- 0.05 * |u'| * |v'| for low angles of attack (less than 7 degrees). Based on Wubben, the error is expected to increase substantially for high levels of the spanwise turbulence, Tu_w, and larger angles of attack. The absolute uncertainty in the heat transfer coefficient was estimated to be +/- 5 percent. The primary sources of uncertainty included the uncertainty in the dissipated heat flux, the uncertainty in the conducted heat flux due to the uncertainty in the epoxy's conductivity, and the uncertainty in surface to adiabatic wall temperature difference due to room air temperature variations and calibration error.

Table 2.1 Exit/Passage Traverse Access Coordinates

Pos No.	X(cm)	X(in)	Y(cm)	Y(in)
1	16.307	6.420	32.169	12.665
2	17.323	6.820	35.217	13.865
3	18.339	7.220	38.265	15.065
4	19.355	7.620	41.313	16.265
5	20.498	8.070	44.742	17.615
6	21.514	8.470	47.790	18.815
7	22.530	8.870	50.838	20.015
8	23.546	9.270	53.886	21.215

Table 2.2 C3X Vane Coordinates

Pos No.	X (cm)	X (in)	Y (cm)	Y (in)	Arc (cm)	Arc (in)
1	0.110	0.0432	11.655	4.5885	0.938	0.3693
2	0.389	0.1533	12.189	4.7988	1.541	0.6067
3	0.766	0.3015	12.676	4.9907	2.157	0.8491
4	1.272	0.5009	13.023	5.1273	2.771	1.0908
5	1.874	0.7379	13.138	5.1723	3.383	1.3321
6	2.471	0.9727	12.994	5.1157	3.997	1.5736
7	2.983	1.1746	12.654	4.9818	4.612	1.8159
8	3.399	1.3380	12.198	4.8022	5.229	2.0587
9	3.738	1.4715	11.682	4.5991	5.846	2.3017
10	4.027	1.5855	11.136	4.3844	6.464	2.5448
11	4.289	1.6884	10.577	4.1640	7.082	2.7880
12	4.533	1.7845	10.009	3.9407	7.699	3.0311
13	4.765	1.8759	9.437	3.7153	8.317	3.2744
14	4.987	1.9634	8.861	3.4884	8.935	3.5176
15	5.202	2.0480	8.281	3.2604	9.552	3.7607
16	5.411	2.1303	7.700	3.0316	10.170	4.0039
17	5.616	2.2109	7.118	2.8022	10.787	4.2470
18	5.817	2.2902	6.534	2.5723	11.405	4.4902
19	6.016	2.3685	5.949	2.3420	12.023	4.7335
20	6.213	2.4459	5.363	2.1115	12.641	4.9766
21	6.407	2.5226	4.777	1.8806	13.259	5.2199
22	6.600	2.5983	4.190	1.6495	13.876	5.4631
23	6.789	2.6730	3.601	1.4179	14.494	5.7065
24	6.976	2.7463	3.012	1.1859	15.112	5.9498
25	7.157	2.8179	2.422	0.9536	15.730	6.1929
26	7.333	2.8872	1.830	0.7205	16.348	6.4360
27	7.502	2.9537	1.236	0.4865	16.965	6.6793
28	7.662	3.0167	0.639	0.2516	17.583	6.9225
29	7.812	3.0754	0.041	0.0162	18.199	7.1651
30	7.816	3.0772	-0.005	-0.0021	18.246	7.1835
31	7.808	3.0741	-0.052	-0.0203	18.293	7.2020
32	7.788	3.0661	-0.093	-0.0368	18.340	7.2203
33	7.757	3.0540	-0.129	-0.0507	18.386	7.2387

Table 2.2 C3X Vane Coordinates (Continued)

Pos No.	X (cm)	X (in)	Y (cm)	Y (in)	Arc (cm)	Arc (in)
34	7.718	3.0386	-0.154	-0.0607	18.433	7.2571
35	7.674	3.0211	-0.168	-0.0662	18.480	7.2754
36	7.627	3.0027	-0.170	-0.0669	18.526	7.2939
37	7.582	2.9849	-0.159	-0.0625	18.573	7.3122
38	7.541	2.9688	-0.136	-0.0534	18.620	7.3307
39	7.508	2.9558	-0.103	-0.0404	18.667	7.3491
40	7.485	2.9468	-0.062	-0.0243	-13.288	-5.2314
41	7.319	2.8814	0.356	0.1401	-12.838	-5.0545
42	7.148	2.8143	0.774	0.3046	-12.387	-4.8768
43	6.974	2.7455	1.189	0.4683	-11.936	-4.6992
44	6.795	2.6752	1.604	0.6313	-11.485	-4.5217
45	6.612	2.6030	2.015	0.7935	-11.034	-4.3442
46	6.424	2.5290	2.425	0.9549	-10.583	-4.1666
47	6.231	2.4531	2.833	1.1153	-10.132	-3.9892
48	6.033	2.3751	3.238	1.2748	-9.681	-3.8116
49	5.830	2.2951	3.641	1.4333	-9.231	-3.6341
50	5.620	2.2127	4.040	1.5906	-8.779	-3.4565
51	5.405	2.1280	4.436	1.7466	-8.329	-3.2790
52	5.183	2.0407	4.829	1.9012	-7.878	-3.1014
53	4.955	1.9507	5.218	2.0542	-7.427	-2.9239
54	4.719	1.8579	5.602	2.2055	-6.976	-2.7464
55	4.476	1.7622	5.982	2.3550	-6.525	-2.5689
56	4.225	1.6633	6.356	2.5025	-6.074	-2.3913
57	3.965	1.5612	6.725	2.6476	-5.623	-2.2139
58	3.697	1.4557	7.087	2.7903	-5.173	-2.0364
59	3.420	1.3466	7.443	2.9303	-4.722	-1.8590
60	3.134	1.2338	7.791	3.0673	-4.271	-1.6815
61	2.837	1.1171	8.131	3.2011	-3.820	-1.5040
62	2.531	0.9966	8.462	3.3313	-3.369	-1.3265
63	2.215	0.8720	8.783	3.4577	-2.919	-1.1491
64	1.888	0.7435	9.093	3.5801	-2.468	-0.9716
65	1.552	0.6110	9.393	3.6981	-2.017	-0.7942
66	1.205	0.4745	9.681	3.8116	-1.566	-0.6166
67	0.849	0.3344	9.958	3.9204	-1.116	-0.4393
68	0.500	0.1968	10.212	4.0203	-0.684	-0.2692
69	0.385	0.1515	10.304	4.0565	-0.537	-0.2112
70	0.282	0.1111	10.409	4.0982	-0.389	-0.1532
71	0.194	0.0763	10.527	4.1446	-0.242	-0.0952
72	0.121	0.0477	10.656	4.1951	-0.094	-0.0371
73	0.065	0.0256	10.792	4.2488	0.053	0.0209
74	0.026	0.0104	10.934	4.3048	0.201	0.0790
75	0.006	0.0025	11.080	4.3623	0.348	0.1370
76	0.000	0.0000	11.166	4.3961	0.434	0.1709
77	0.005	0.0018	11.228	4.4204	0.496	0.1953
78	0.022	0.0085	11.374	4.4780	0.643	0.2532
79	0.057	0.0224	11.517	4.5343	0.791	0.3112

Table 2.3 C3X Vane Pressure Tap Locations

Pos No.	X (cm)	X (in)	Y (cm)	Y (in)	Arc (cm)	Arc (in)
1	0.907	0.357	0.153	0.060	-12.573	-4.950
2	1.653	0.651	0.300	0.118	-11.811	-4.650
3	2.402	0.946	0.436	0.171	-11.049	-4.350
4	3.153	1.241	0.556	0.219	-10.287	-4.050
5	3.907	1.538	0.663	0.261	-9.525	-3.750
6	4.663	1.836	0.753	0.297	-8.763	-3.450
7	5.421	2.134	0.824	0.324	-8.001	-3.150
8	6.181	2.433	0.874	0.344	-7.239	-2.850
9	6.942	2.733	0.902	0.355	-6.477	-2.550
10	7.704	3.033	0.903	0.355	-5.715	-2.250
11	8.466	3.333	0.875	0.344	-4.953	-1.950
12	9.225	3.632	0.817	0.321	-4.191	-1.650
13	9.981	3.929	0.723	0.285	-3.429	-1.350
14	10.730	4.224	0.591	0.233	-2.667	-1.050
15	11.470	4.516	0.422	0.166	-1.905	-0.750
16	12.200	4.803	0.214	0.084	-1.143	-0.450
17	12.927	5.089	0.005	0.002	-0.381	-0.150
18	13.657	5.377	0.167	0.066	0.381	0.150
19	14.138	5.566	0.712	0.280	1.143	0.450
20	14.435	5.683	1.374	0.541	1.905	0.750
21	14.511	5.713	2.084	0.821	2.667	1.050
22	14.230	5.602	2.743	1.080	3.429	1.350
23	13.627	5.365	3.170	1.248	4.191	1.650
24	12.899	5.078	3.363	1.324	4.953	1.950
25	12.139	4.779	3.389	1.334	5.715	2.250
26	11.381	4.481	3.317	1.306	6.477	2.550
27	10.631	4.185	3.193	1.257	7.239	2.850
28	9.885	3.892	3.047	1.199	8.001	3.150
29	9.142	3.599	2.884	1.135	8.763	3.450
30	8.403	3.308	2.709	1.067	9.525	3.750
31	7.666	3.018	2.525	0.994	10.287	4.050
32	6.931	2.729	2.334	0.919	11.049	4.350
33	6.197	2.440	2.140	0.842	11.811	4.650
34	5.465	2.151	1.942	0.765	12.573	4.950
35	4.733	1.863	1.741	0.685	13.335	5.250
36	4.002	1.576	1.536	0.605	14.097	5.550
37	3.273	1.288	1.327	0.523	14.859	5.850
38	2.545	1.002	1.113	0.438	15.621	6.150
39	1.820	0.716	0.891	0.351	16.383	6.450
40	1.099	0.433	0.658	0.259	17.145	6.750
41	0.383	0.151	0.411	0.162	17.907	7.050
42	0.001	0.000	0.153	0.060	18.415	7.250

Table 2.4 C3X Vane Thermocouple Locations

Pos No.	X(cm)	X(in)	Y(cm)	Y(in)	Arc(cm)	Arc(in)
1	1.234	0.486	0.219	0.086	-12.238	-4.818
2	2.009	0.791	0.366	0.144	-11.448	-4.507
3	2.718	1.070	0.488	0.192	-10.728	-4.223
4	3.399	1.338	0.593	0.233	-10.038	-3.952
5	4.110	1.618	0.689	0.271	-9.320	-3.669
6	4.905	1.931	0.777	0.306	-8.519	-3.354
7	5.649	2.224	0.841	0.331	-7.772	-3.060
8	6.513	2.564	0.889	0.350	-6.907	-2.719
9	7.193	2.832	0.905	0.356	-6.226	-2.451
10	7.879	3.102	0.899	0.354	-5.540	-2.181
11	8.684	3.419	0.863	0.340	-4.734	-1.864
12	9.459	3.724	0.791	0.311	-3.955	-1.557
13	10.231	4.028	0.683	0.269	-3.174	-1.250
14	10.983	4.324	0.539	0.212	-2.407	-0.948
15	11.765	4.632	0.343	0.135	-1.598	-0.629
16	12.451	4.902	0.130	0.051	-0.876	-0.345
17	13.216	5.203	0.013	0.005	-0.091	-0.036
18	13.928	5.484	0.376	0.148	0.732	0.288
19	14.323	5.639	1.044	0.411	1.540	0.606
20	14.512	5.713	1.824	0.718	2.392	0.942
21	14.358	5.653	2.512	0.989	3.151	1.241
22	14.008	5.515	2.931	1.154	3.727	1.467
23	13.437	5.290	3.243	1.277	4.397	1.731
24	12.647	4.979	3.396	1.337	5.208	2.050
25	11.890	4.681	3.373	1.328	5.966	2.349
26	11.156	4.392	3.281	1.292	6.706	2.640
27	10.351	4.075	3.140	1.236	7.525	2.963
28	9.484	3.734	2.961	1.166	8.412	3.312
29	8.860	3.488	2.818	1.110	9.055	3.565
30	8.131	3.201	2.641	1.040	9.807	3.861
31	7.376	2.904	2.450	0.965	10.588	4.169
32	6.632	2.611	2.256	0.888	11.360	4.472
33	5.847	2.302	2.046	0.805	12.176	4.794
34	5.138	2.023	1.853	0.729	12.913	5.084
35	4.445	1.750	1.661	0.654	13.635	5.368
36	3.680	1.449	1.445	0.569	14.433	5.682
37	3.117	1.227	1.282	0.505	15.023	5.914
38	2.146	0.845	0.992	0.390	16.040	6.315
39	1.461	0.575	0.776	0.306	16.763	6.600

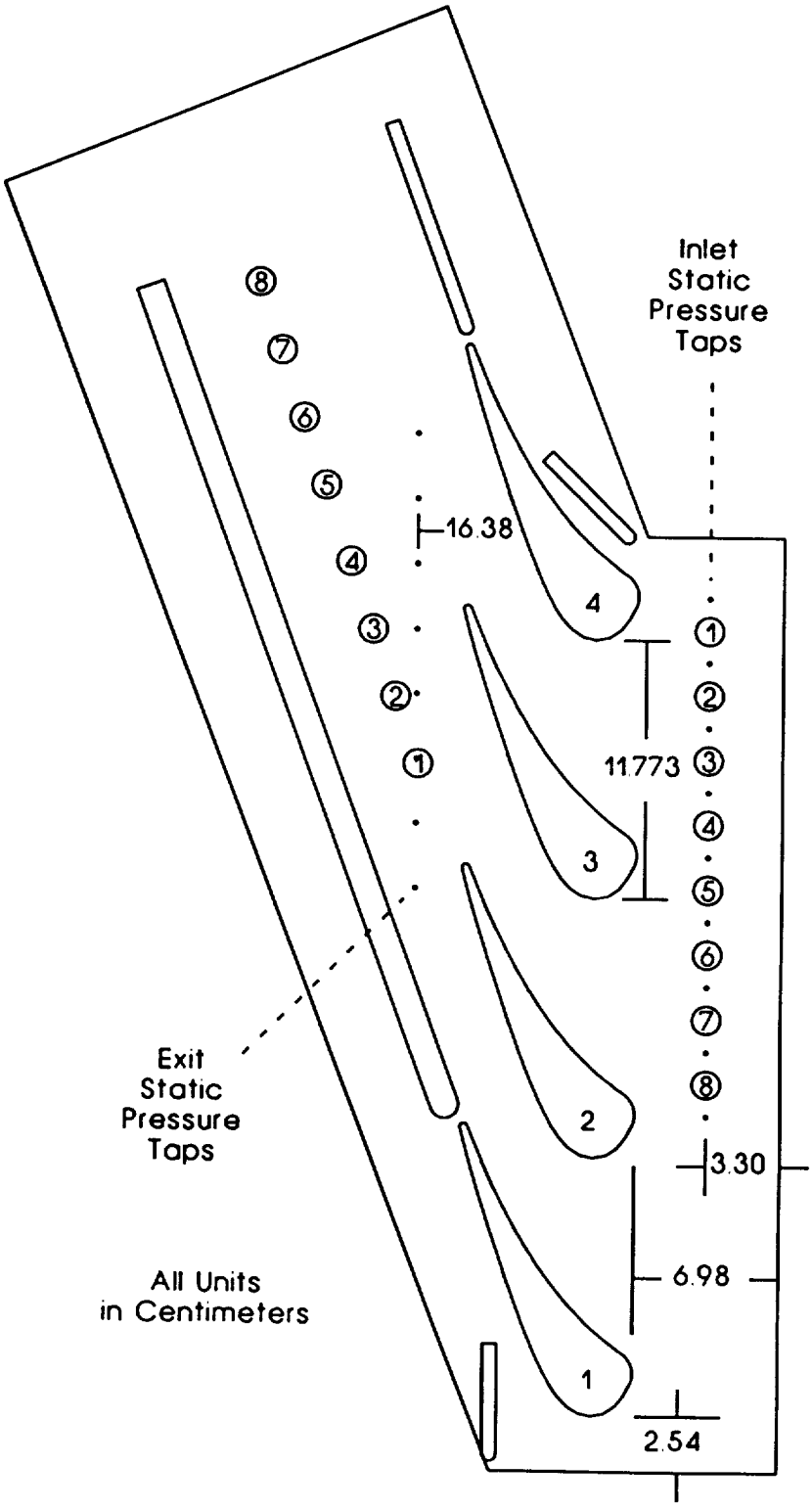

Figure 2.1 Schematic of four vane C3X cascade

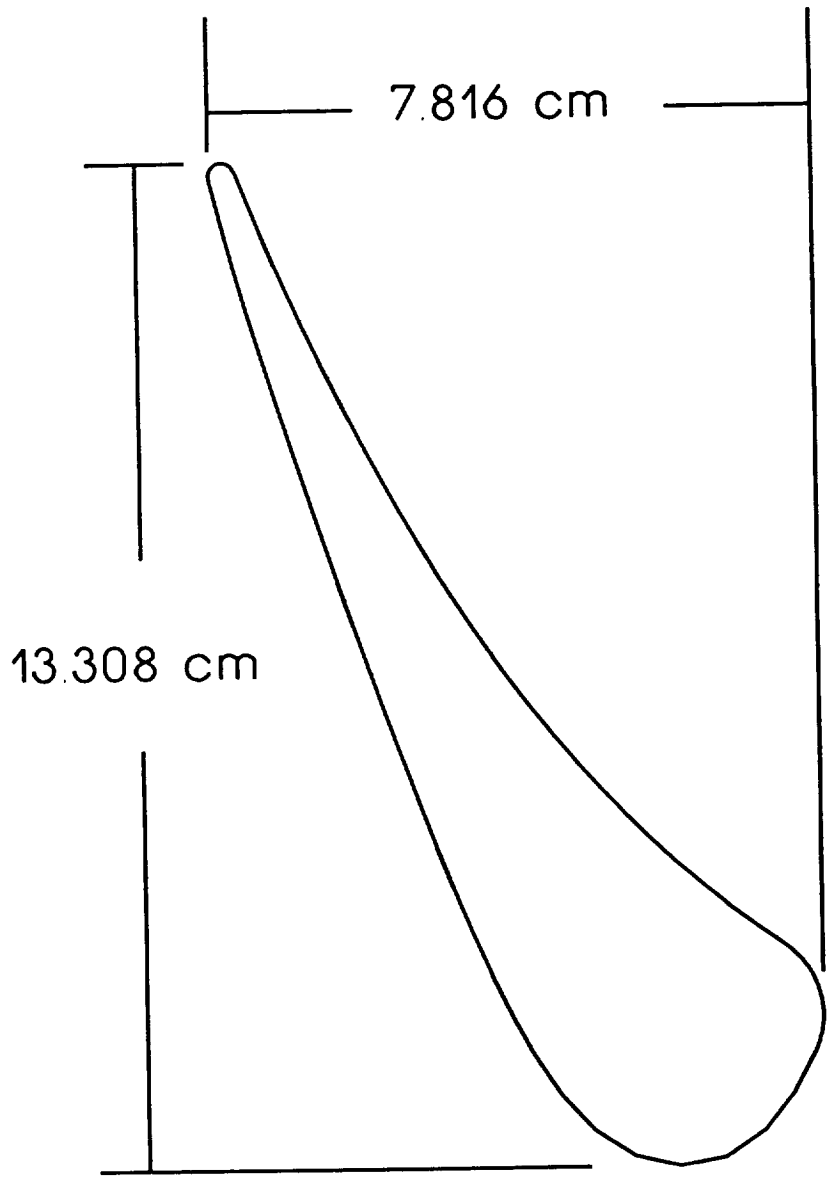

Figure 2.2 C3X vane geometry as setup in cascade

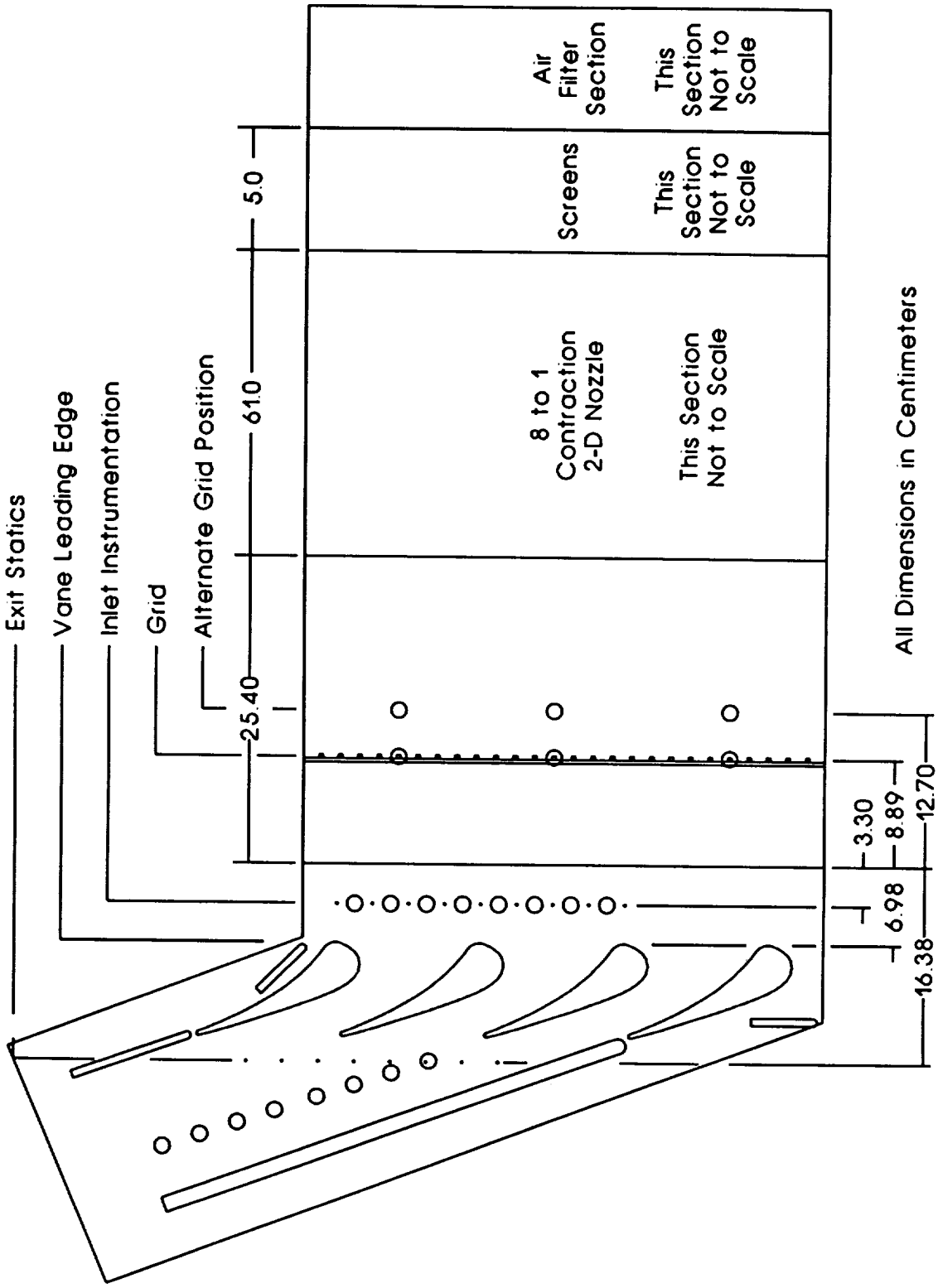

Figure 2.3 Cascade inlet setup for grid and low turbulence

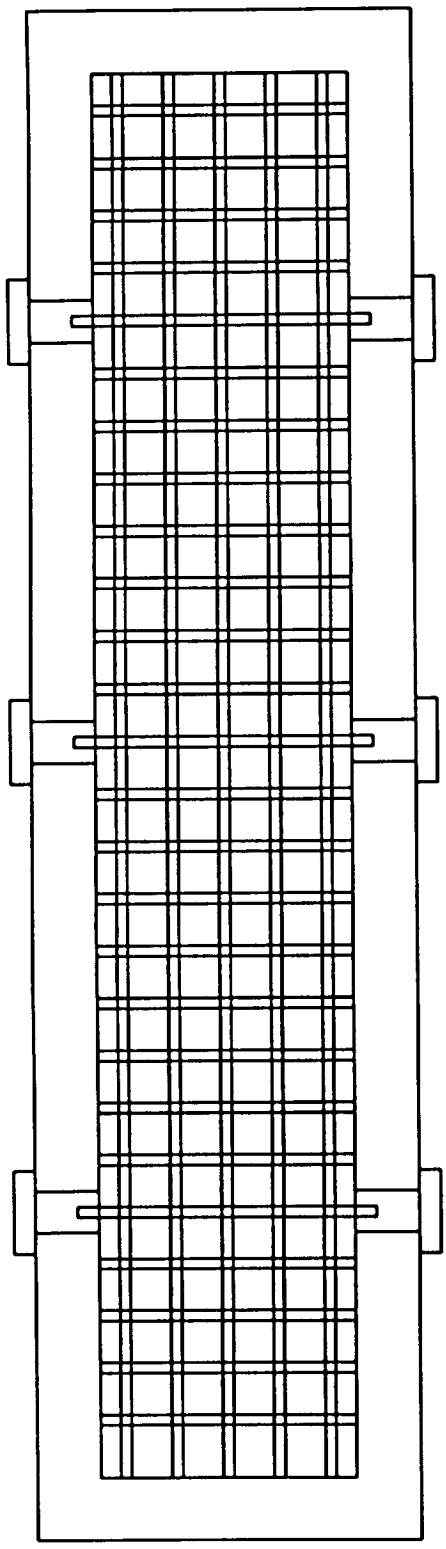

Square Mesh
Grid Design
Spanwise
Spacing = 1.524 cm
Pitchwise
Spacing = 1.588 cm
Bar = 0.318 cm

Figure 2.4 Schematic of biplanar square mesh grid

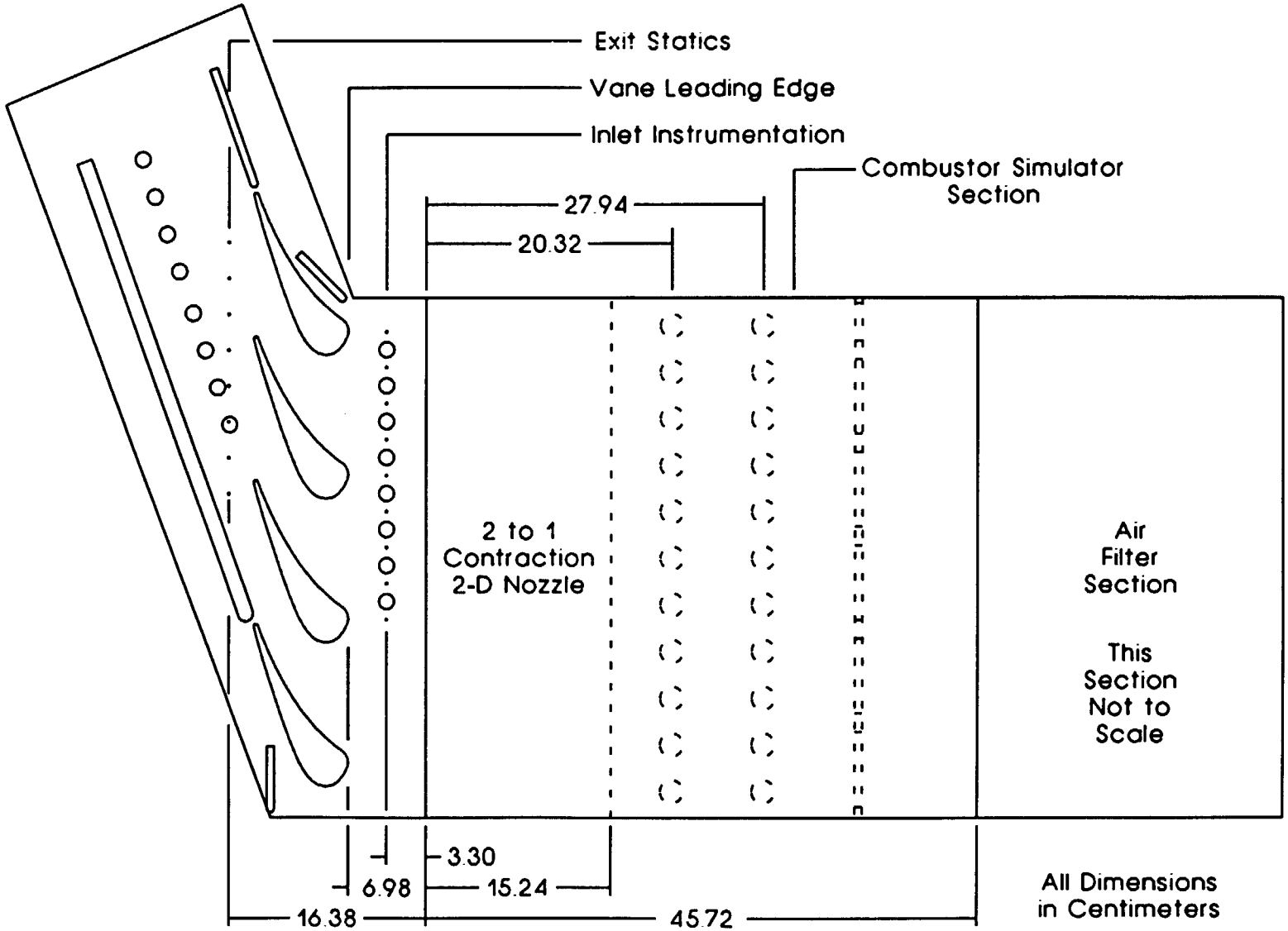

Figure 2.5 Cascade inlet setup for combustor in close position

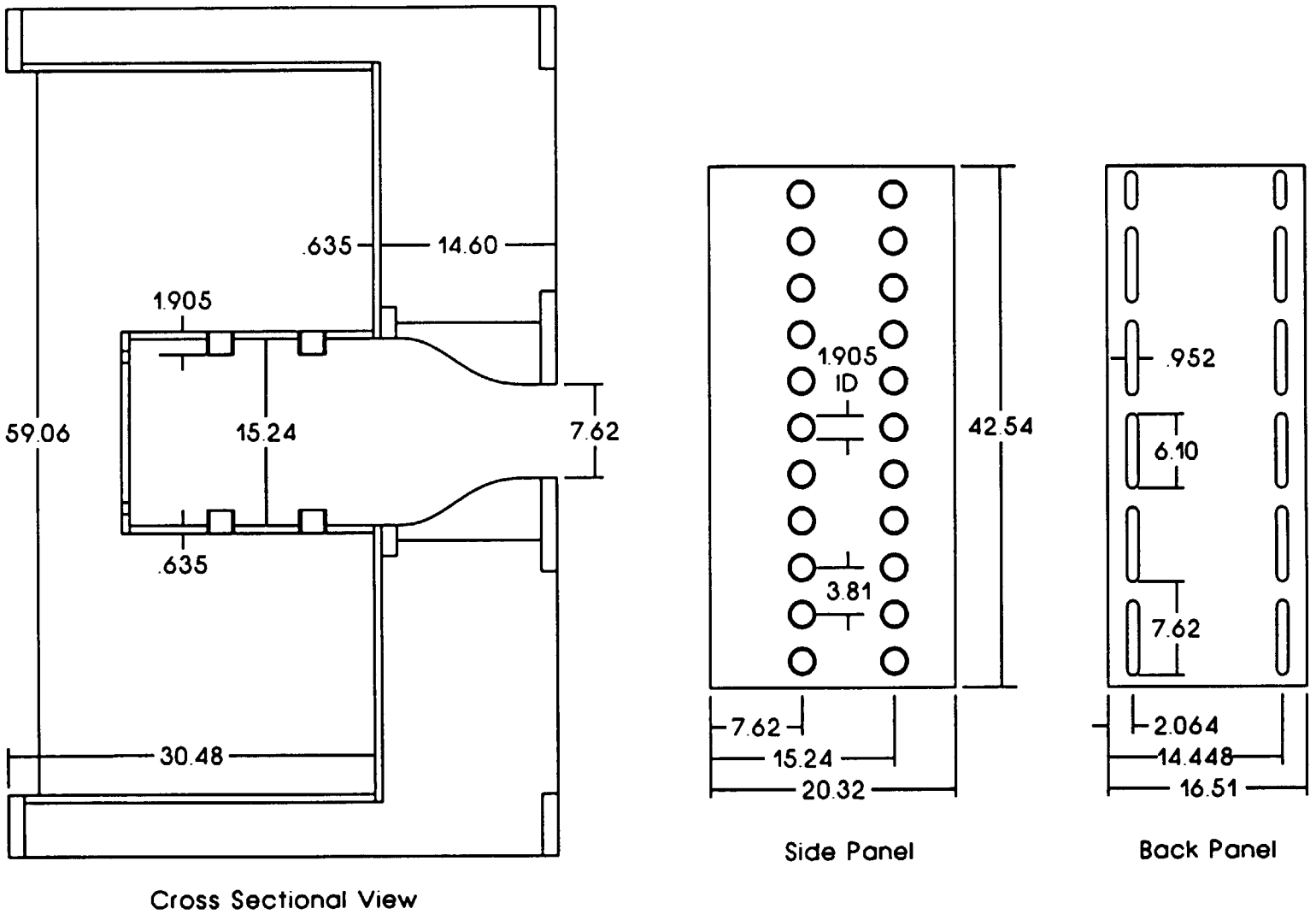

Figure 2.6 Schematic of combustor turbulence generator

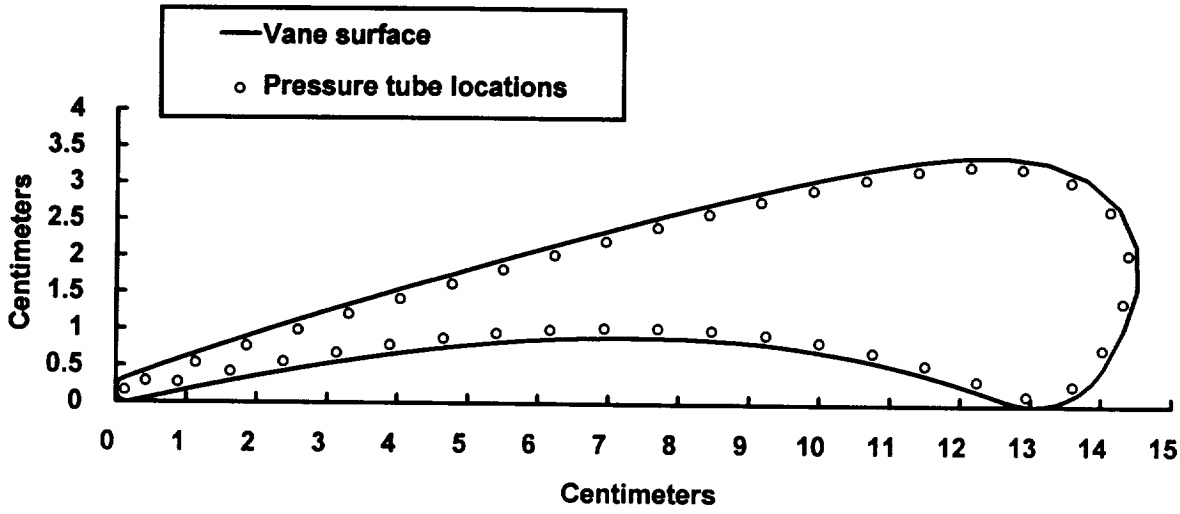

Figure 2.7 C3X vane pressure tap locations

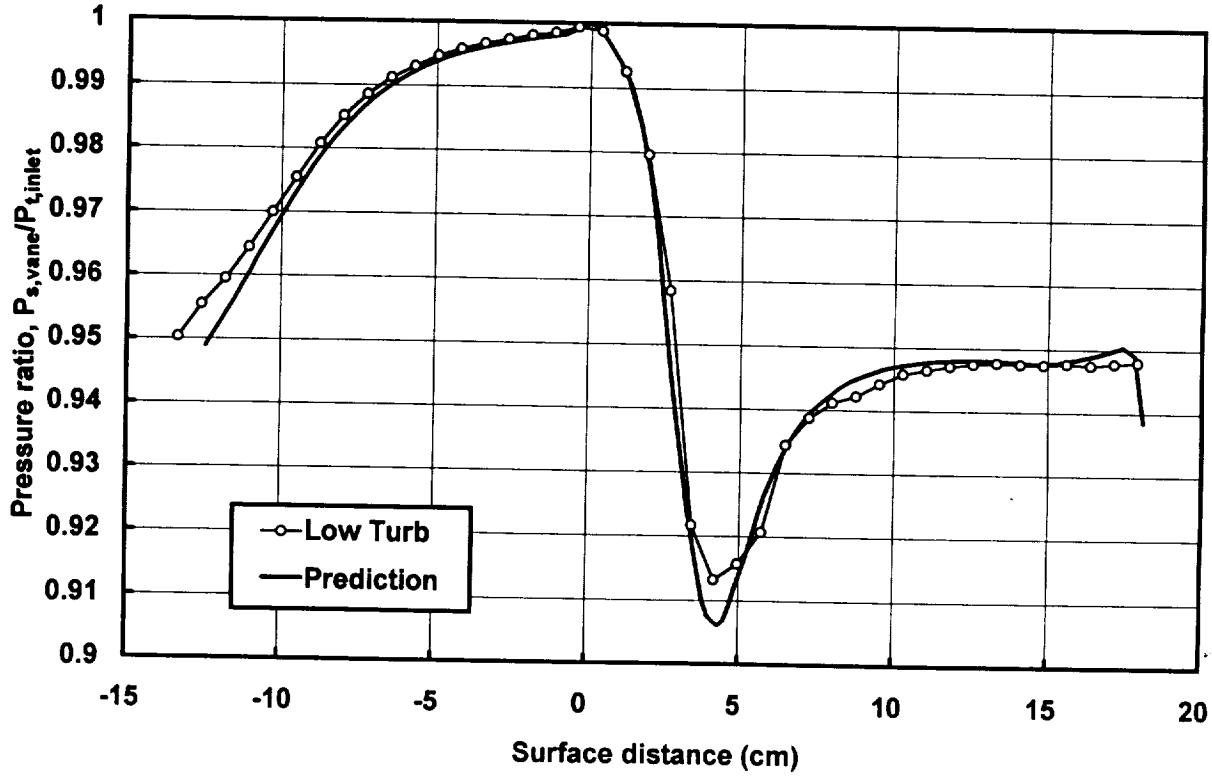

Figure 2.8 Comparison of measured and predicted pressure profiles for low turbulence case, $Ma_{ex} = 0.27$

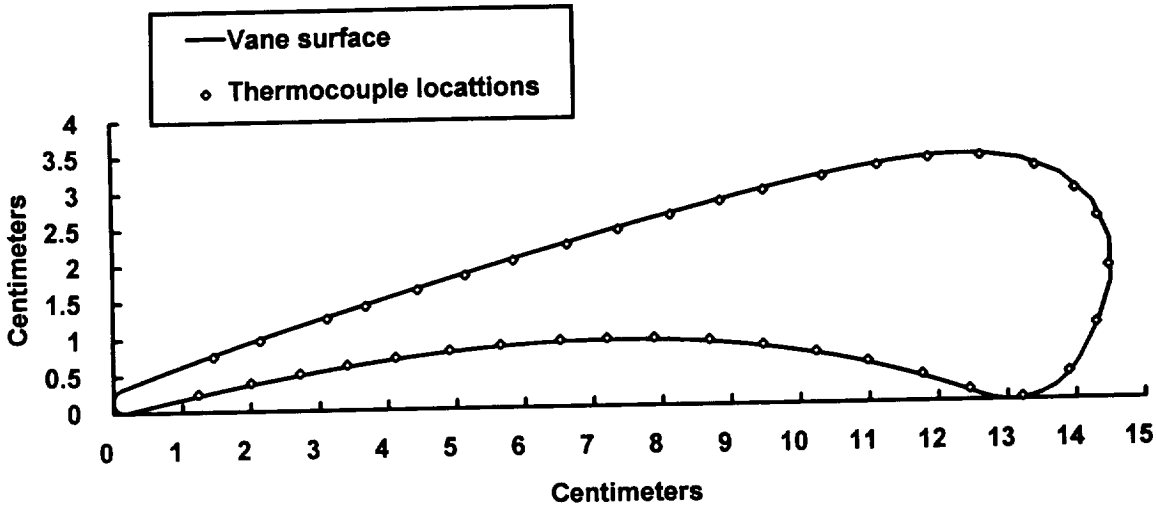

Figure 2.9 C3X vane thermocouple locations

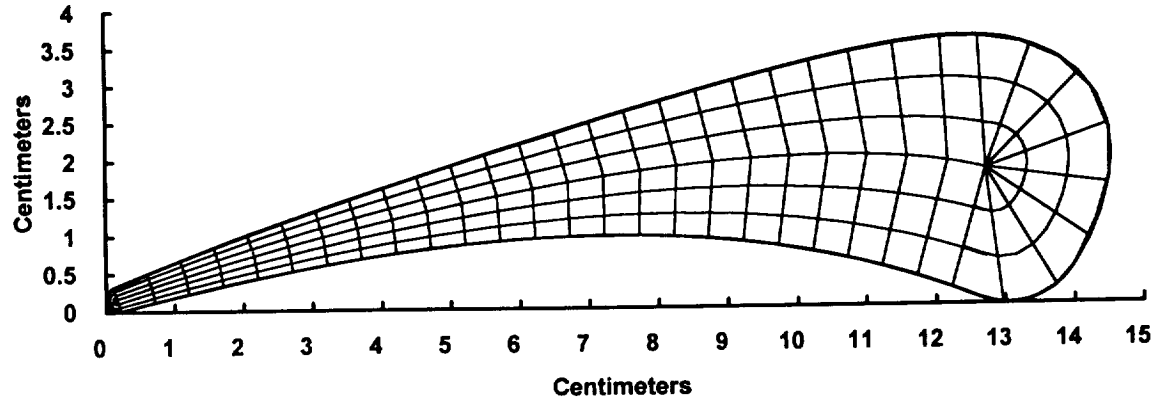

Figure 2.10 C3X vane finite element mesh for conduction analysis

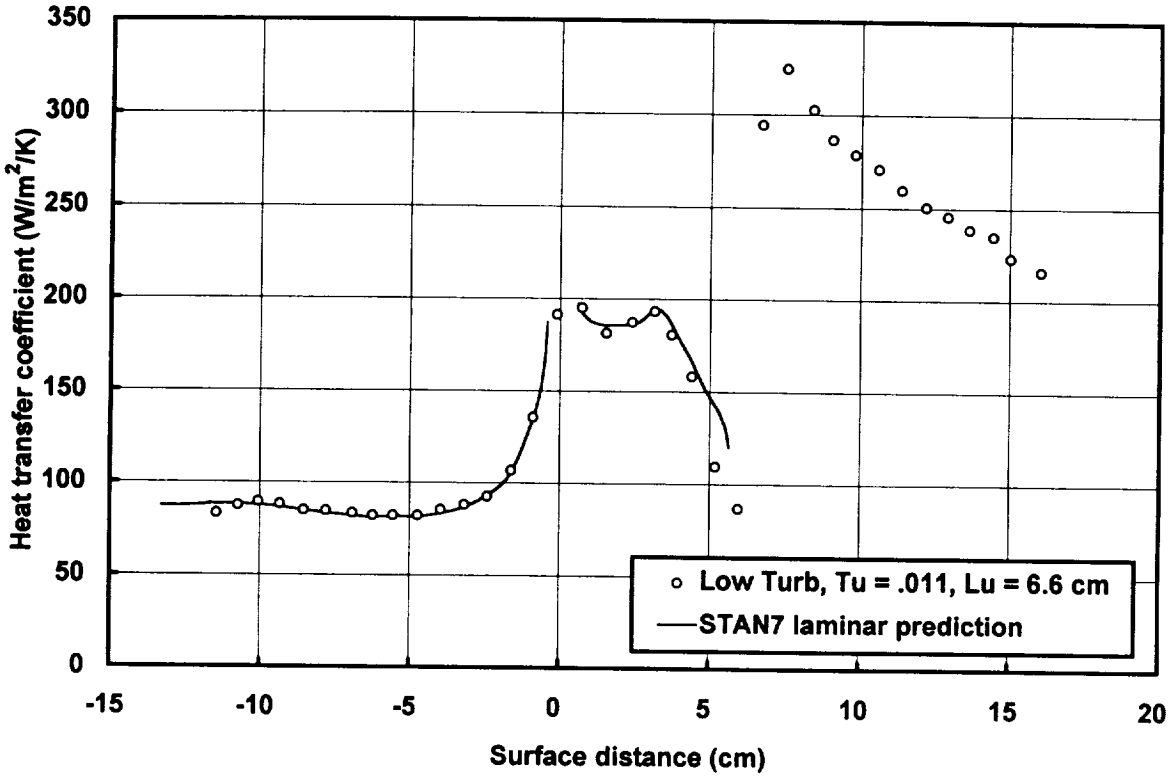

Figure 2.11 Comparison of baseline heat transfer test with STAN7 calculation, Re_{ex} = 780,000, Ma_{ex} = 0.27

Chapter 3

Inlet Conditions

This chapter provides documentation for the inlet conditions into the cascade for this vane turbulence and heat transfer study. Descriptions are given for the inlet velocity, total pressure, and turbulence components distributions. In addition, the inlet turbulence scale, and one dimensional spectra are also discussed.

Inlet Velocity

The cascade inlet velocity distribution was detailed by both total pressure measurements and hot wire measurements. Figure 3.1 shows cross span inlet velocity distributions at one Z position (equivalent to circumferential spacing in an engine) for the four turbulence conditions. All four turbulence inlet conditions had good inlet uniformity. Based on the inlet total pressure measurements, the low turbulence condition total pressure distributions were consistent within about 0.3 percent in the region of the flow outside the boundary layers or the "core" region of the flow. The grid turbulence had the greatest variation with an root mean square average variation in total pressure of 2.8 percent. The two locations of the combustor simulator both had RMS variations in pressure of about one percent. The variation in velocity is very close to one half of the total pressure variation.

Figure 3.2 shows the inlet velocity distribution in the circumferential direction based on the inlet static pressure taps. The inlet plane for the inlet static taps is located 3.68 cm upstream of the leading edge plane of the vanes. A vane shape is shown in the figure to provide the circumferential position of vane 3 relative to the static pressure tap positions. The upper and lower bleed flow adjustment blocks, as pictured in figure 2.1 of chapter 2, are used to establish inlet plane periodicity. Typical uniformity between vanes is within one percent.

Typical inlet boundary layer profiles based on total pressure measurements are shown in figure 3.3 for the highest inlet velocity. Momentum thickness Reynolds numbers, skin friction coefficients, and turbulence levels for the velocity profiles based on inlet total pressure measurements are given in table 3.1. The low turbulence configuration and the configuration with the combustor in the far position had the largest momentum thickness and the lowest skin friction coefficient. Surprisingly, the inlet momentum thickness for the combustor in the close position [comb(1)] was not a great deal different than for the combustor in the far position [comb(2)]. Apparently

the turbulent mixing in the inlet duct is sufficiently high to mix low momentum fluid from the boundary layer into the center of the flow to produce a total pressure loss along the duct. This streamwise total pressure loss is similar to the loss in a fully developed duct flow and explains the slow growth of the inlet momentum thickness. The inlet configuration with the grid had the smallest inlet momentum thickness and the highest skin friction coefficient. Table 3.1 shows a significant difference between momentum thickness Reynolds numbers determined with a total pressure probe and momentum thickness Reynolds numbers determined with a single wire probe. Determining the edge of the boundary layer is uncertain for a boundary layer subjected to a high turbulence level due to the very gradual velocity gradients at the boundary layers edge. The small velocity gradients are also combined with the variations in velocity imposed during the generation of turbulence and not thoroughly mixed out. An additional complication is probe blockage which produces a mild velocity gradient in the hot wire measurements as the probe is withdrawn from the opposite wall. Total pressure measurements do not exhibit this problem. The effect of blockage on the static reference pressures can be removed by referencing taps in the same location but in a different passage. Because of this potential error in the single wire velocity profiles caused by probe blockage in the inlet channel, the total pressure measurements are viewed as the most accurate. Comparison of the skin friction estimates show these values are consistent within ten percent. One discrepancy does exist for the momentum thicknesses determined for the first low turbulence condition. This variation is likely the result of differences in the transition origin which may be due to subtle differences in the alignment between the 8 to 1 contraction nozzle and the inlet spool.

Inlet Turbulence

Typical cross span distributions of the inlet turbulence level are given in figure 3.4. Based on single wire surveys, the streamwise core region (The core region is the region of flow where the turbulence is largely unaffected by the wall.) turbulence levels for the baseline configuration, the grid, the combustor with spool, and the close combustor are 1.0 percent, 7.7 percent, 8.5 percent, and 12.8 percent. It should be noted that the turbulence characteristics determined for both build ups of the turbulence generator were taken 3.68 cm upstream from the vane inlet plane. The grid values were taken with the grid in the aft position but prior to running, the grid was moved forward by 3.68 cm. Therefore, the values quoted for the grid should correspond to the values at the vane inlet plane. The values quoted for the turbulence generator need to be adjusted for the 3.68 cm of additional decay. A simple method to estimate this change in turbulence level which is reasonably accurate over a short distance is $Tu = 1/\{1/Tu_0 + X/(2\ Lu_\infty)\}$. This equation can be developed by integrating the kinetic energy equation for turbulence, assuming that gradients in Y can be neglected and that dissipation can be estimated from the definition of Lu assuming that Lu is constant. Cross span surveys of turbulence components are given in figures 3.5 through 3.7 for the three high turbulence geometries. Figure 3.5 shows the inlet turbulence profiles for

the combustor simulator in the close position [comb(1)]. The turbulence level is about 13.2 percent for the u' component and about 15.5 percent for the v' component which in this case is normal to the endwall. Figure 3.6 shows the inlet turbulence components for the combustor with the 10 inch long spool. The u' component turbulence level is about 8.9 percent while the v' component turbulence has a level of 9.7 percent. Figure 3.7 shows the inlet turbulence components for the grid generated turbulence. The u' component has a level of 7.7 percent while the v' level was 8.0 percent for the grid turbulence. The ratios of v'/u' for the combustor, combustor with spool, and grid are 1.18, 1.09, and 1.04 respectively.

The distribution of v'^2, normalized on its free stream value, is shown in figure 3.8 as a function of Y. The data indicate there is a definite scale effect. The same data are plotted in figure 3.9 as a function of Y/Lu. In this presentation, the data collapse nicely indicating the surface normal distribution of v' is related to the free stream energy scale. Both the grid turbulence and the combustor simulator with spool turbulence have near wall increases in v'^2 due to production in the boundary layer. The combustor simulator turbulence shows attenuation of v'^2 to the lowest Y measuring station. Unlike the lower turbulence conditions, the close combustor's high level of v'^2 and its strong attenuation near the wall masks any influence to v'^2 due to production in the boundary layer. Based on the research of Ames, the normal distribution of v'^2 is important in determining the effect of turbulence on boundary layer heat transfer and skin friction.

One Dimensional Power Spectra

One dimensional power spectra for the inlet turbulence are shown in figure 3.10 through figure 3.12 for the three high turbulence cases. One dimensional spectra for both the streamwise and normal fluctuation velocities are shown for the combustor simulator in its closest position in figure 3.10. Both the u' and v' spectra show a full decade of -5/3 slope in the inertial subrange. The presence of a substantial inertial subrange is typical of spectra with high turbulence Reynolds numbers. A Taylor Reynolds, Re_λ, number of over 100 is necessary for a well developed inertial subrange. The Taylor Reynolds number of this flow is about 270.

Isotropic relations yield that $E_2(k_1) = 4/3\ E_1(k_1)$ [Hinze [23]] in the inertial subrange. In the spectra shown, the values of $E_2(k_1)$ and $E_1(k_1)$ match this relationship within 7 percent. In general, all the single point two component inlet spectra match this relationship within 9 percent. This consistency indicates that although the v' component of turbulence is 18 percent higher than the u' component for this buildup, the small scale eddies show isotropy within experimental accuracy. This small scale isotropy implies that in the inlet region of a first stage turbine, isotropic relationships ought to be reasonably valid.

One dimensional power spectra are shown for the combustor simulator with spool in figure 3.11. Both the u' and v' spectra have about a decade with a -5/3 slope region. The Taylor Reynolds number for this flow is about 250 and the u' and v' spectra match the isotropic relationship in the inertial subrange within 9 percent. Figure 3.12 shows the one dimensional spectra for the grid turbulence. The inertial subrange region is a bit smaller here but within this region the u' and v' spectra agree closely with the isotropic relationship $E_2(k_1) = 4/3\ E_1(k_1)$. The Taylor Reynolds number for this flow is only about 130.

Figure 3.13 shows one dimensional spectra for the v' component of turbulence at a range of distances from the wall for the close combustor condition. The spectra are plotted as a function of wavenumber. As the probe gets closer to the wall, the measured spectra show less and less energy in the lower frequency eddies. Yet, in the smaller wave number eddies, the spectra remain reasonably constant. This figure implies that the near wall distribution of the v' component of turbulence is dependent on the distribution of energy in the smaller wave number spectra. Based on relationships for the inertial subrange, the distribution of the higher frequency spectra is determined from the dissipation rate. The energy scale, Lu, which is based on the dissipation rate can therefore be expected to correlate the near wall distribution of v'^2. Figure 3.9 shows that Lu does correlate the near wall distribution of v'^2. If we assume that the eddy diffusivity in the free stream fluid near the wall scales on v' and y, then the near wall distribution of eddy diffusivity ought to scale on Lu, Tu, and y. Since this free stream fluid is entrained into the boundary layer and has been shown to augment boundary layer heat transfer and skin friction, Lu is a logical scale to use in correlating the effects of turbulence on heat transfer.

Turbulent Scales

Nominally, the energy scale for the combustor turbulence was 3.36 cm, the combustor with spool had an energy scale of 4.34 cm, and the grid turbulence had a scale of 1.36 cm. A complete list of scales determined from the inlet turbulence is given in Appendix A.1.

Table 3.1 Inlet Velocity Profile Parameters

Velocity Profiles from Total Pressure

Condition	Files	U_∞ (m/s)	Cf/2	U_{core} (m/s)	$Re_{\delta 2}$
Low	CI2R8P2	29.88	0.00224	29.73	1183
Low	CI6R8P2	29.84	0.00216	29.83	1392
Grid	I2R8G2P	29.54	0.00269	29.96	841
Grid	I6R8G2P	29.83	0.00272	30.11	769
Comb(2)	I2R8CBSP	27.55	0.00237	28.30	1239
Comb(2)	I6R8CBSP	28.90	0.00240	29.21	1267
Comb(1)	SI2R8P	28.13	0.00259	29.13	1070
Comb(1)	SI6R8P	29.08	0.00232	29.55	1286

Velocity Profiles from Single Wire

Condition	Files	U_∞ (m/s)	Cf/2	U_{core} (m/s)	$Re_{\delta 2}$	Tu
Low	I2R8C2	29.78	0.00294	29.69	514	0.012
Low	I6R8C2	29.44	0.00239	29.51	1139	0.009
Grid	I2R8G2	30.71	0.00268	30.94	802	0.075
Grid	I6R8G2	30.02	0.00269	30.72	792	0.083
Comb(2)	I2R8CBS	29.18	0.00253	29.18	1839	0.095
Comb(2)	I6R8CBS	29.73	0.00254	29.55	1388	0.086
Comb(1)	I2R8CB	29.01	0.00241	29.46	1897	0.142
Comb(1)	I6R8CB	29.71	0.00212	29.54	2588	0.132

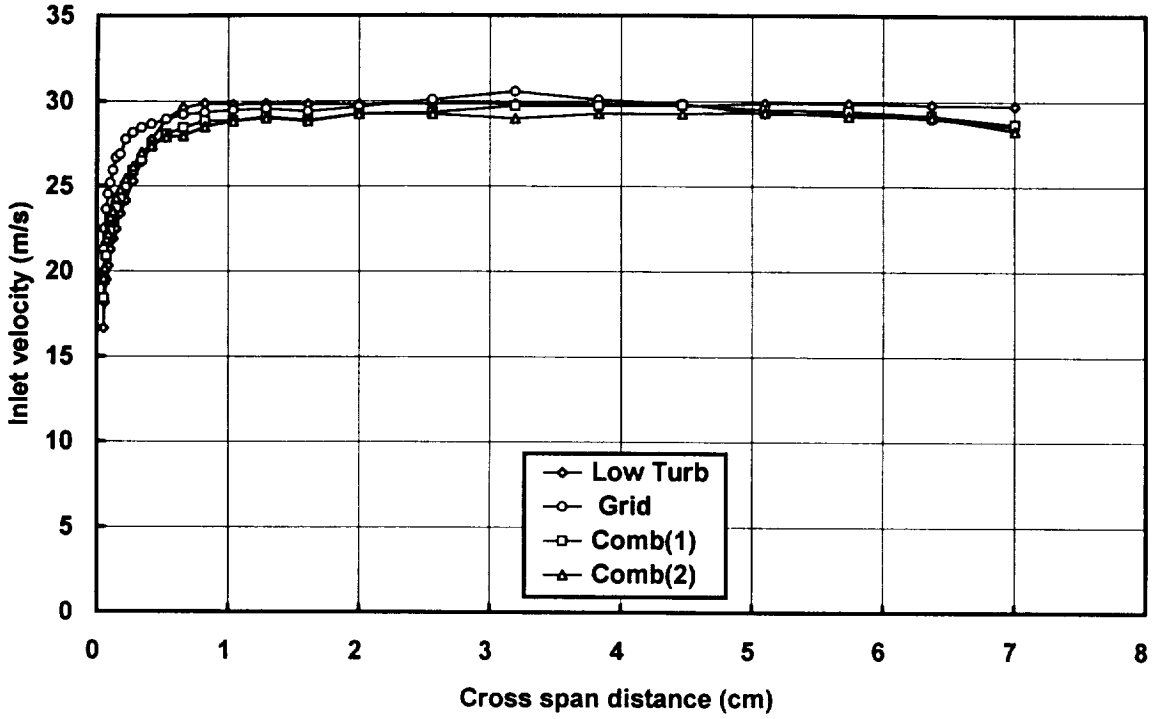

Figure 3.1 Comparison of total pressure inlet velocities for the four turbulence conditions

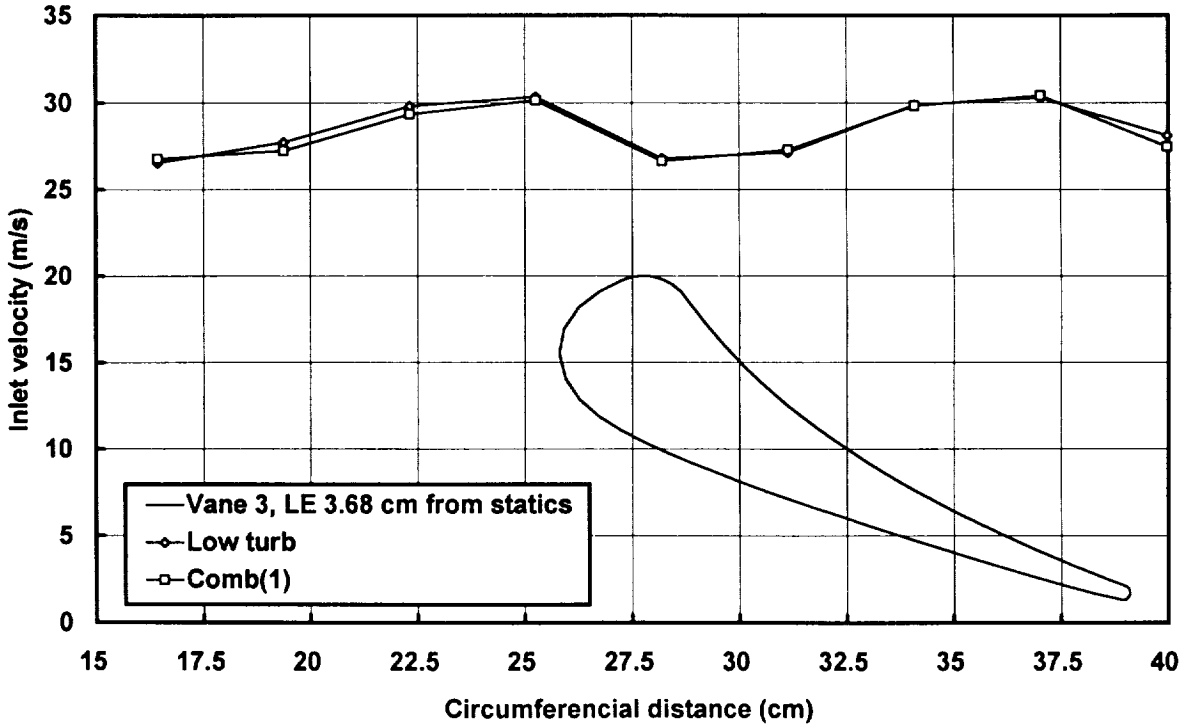

Figure 3.2 Circumferential distribution of inlet velocity based on static pressure, $Ma_{ex} = 0.27$

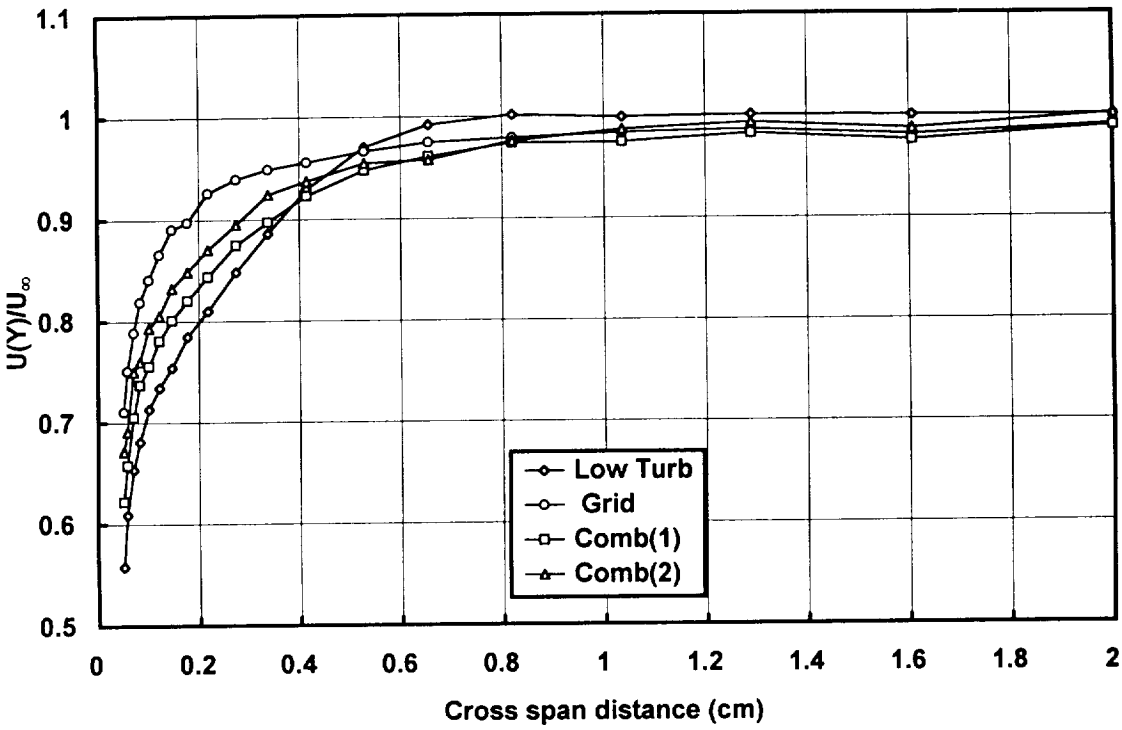

Figure 3.3 Comparison of inlet boundary layer profiles for the four turbulence conditions based on total pressure, U_∞ = 30 m/s

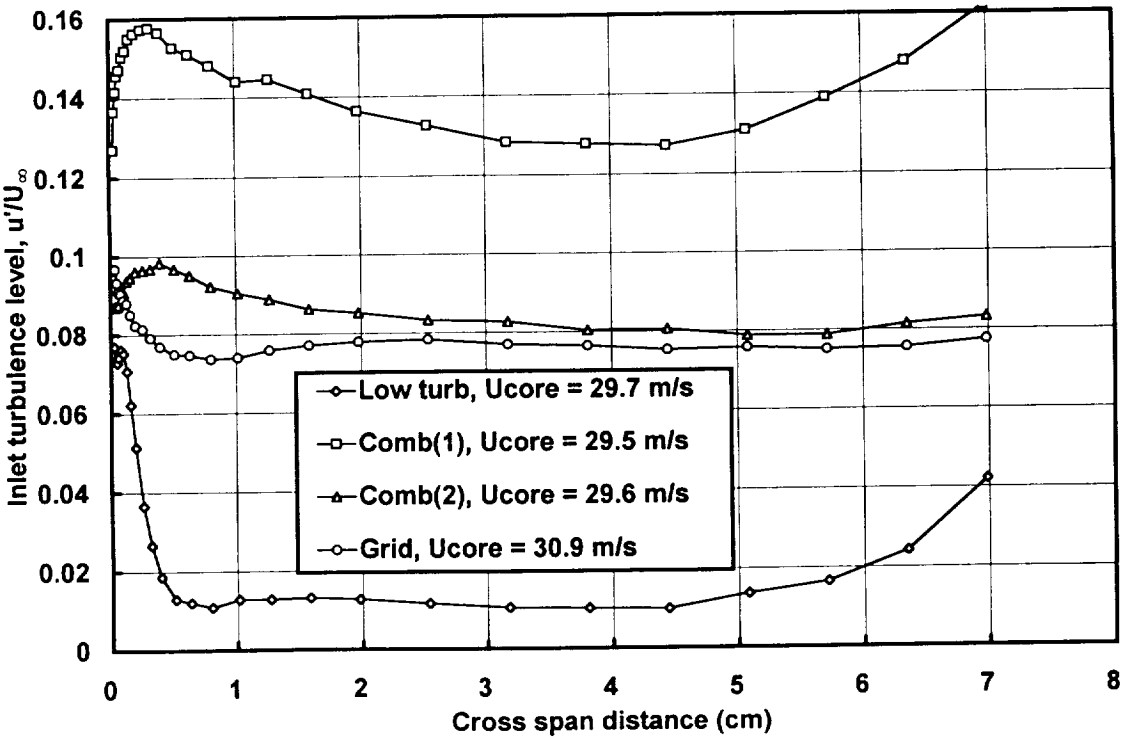

Figure 3.4 Comparison of inlet turbulence level for the four turbulence conditions, U_∞ = 30 m/s

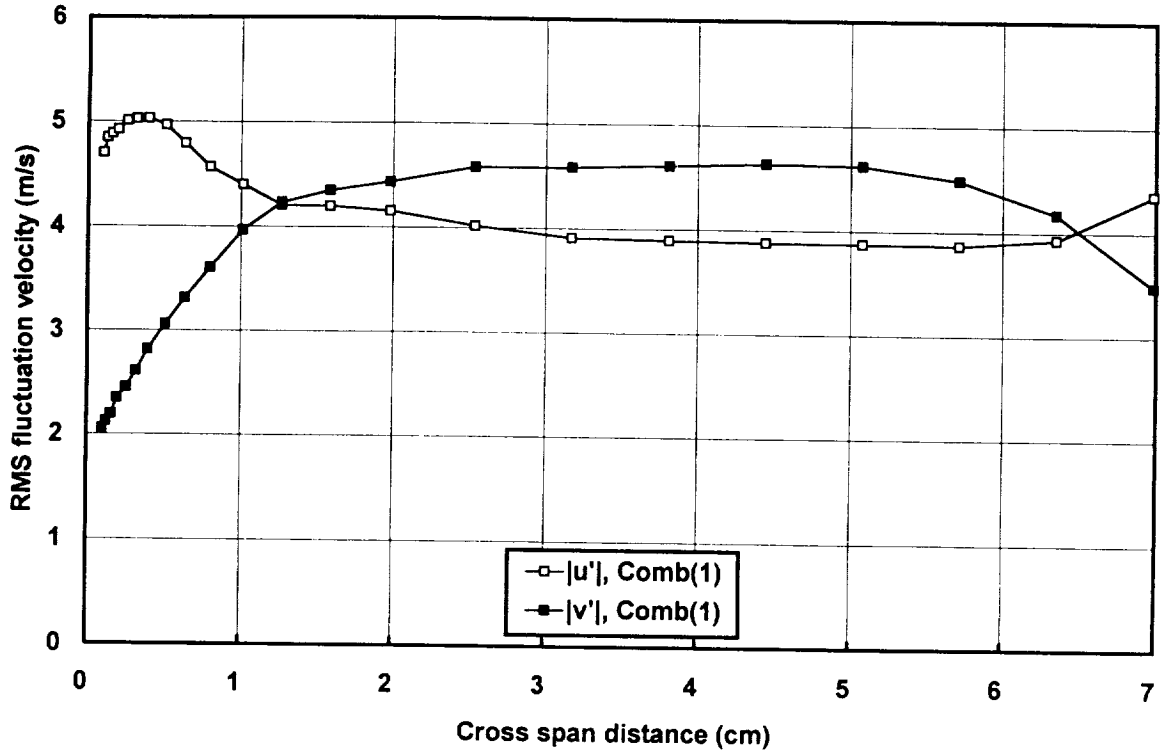

Figure 3.5 Cross span survey of turbulence components, Comb(1), U_∞ = 30 m/s

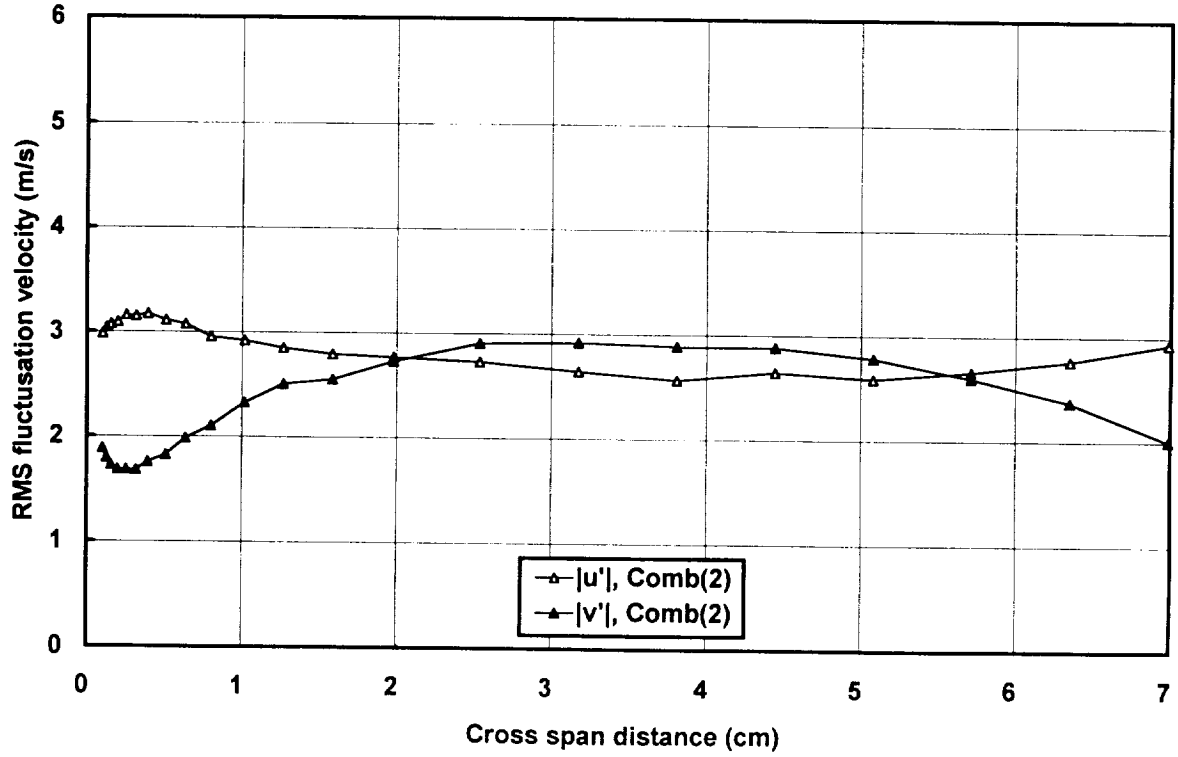

Figure 3.6 Cross span survey of turbulence components, Comb(2), U_∞ = 30 m/s

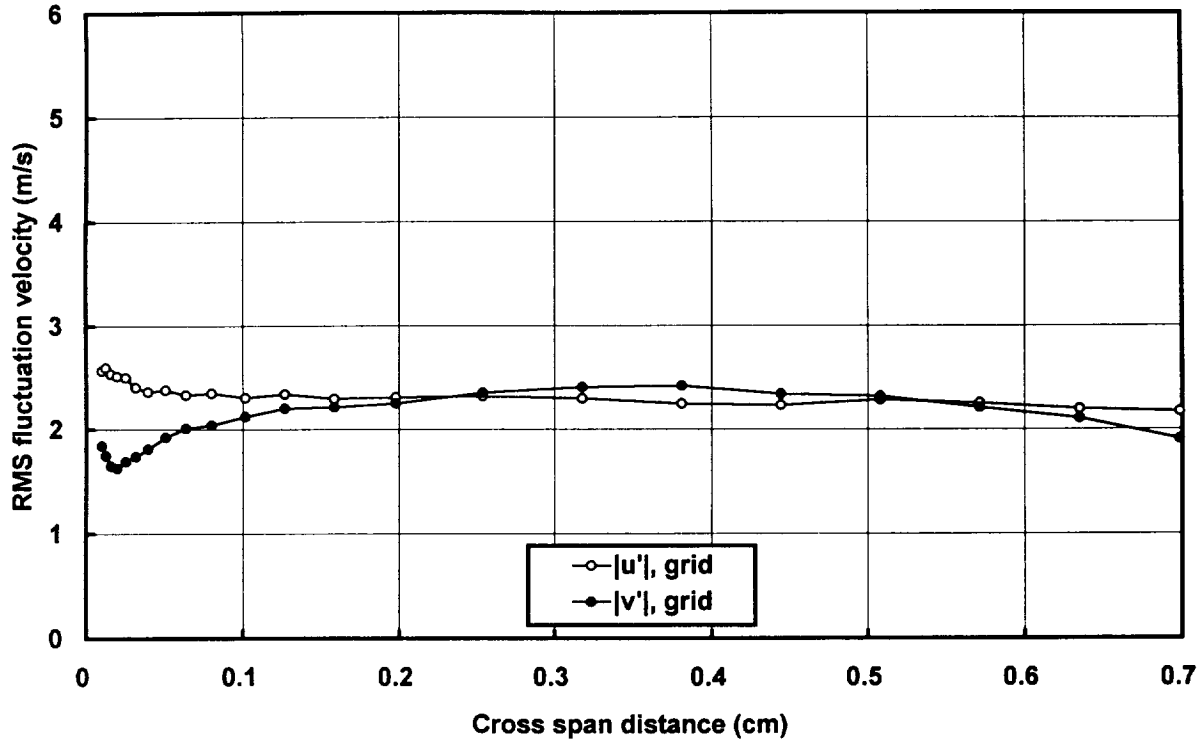

Figure 3.7 Cross span survey of turbulence components, Grid, U_∞ = 30 m/s

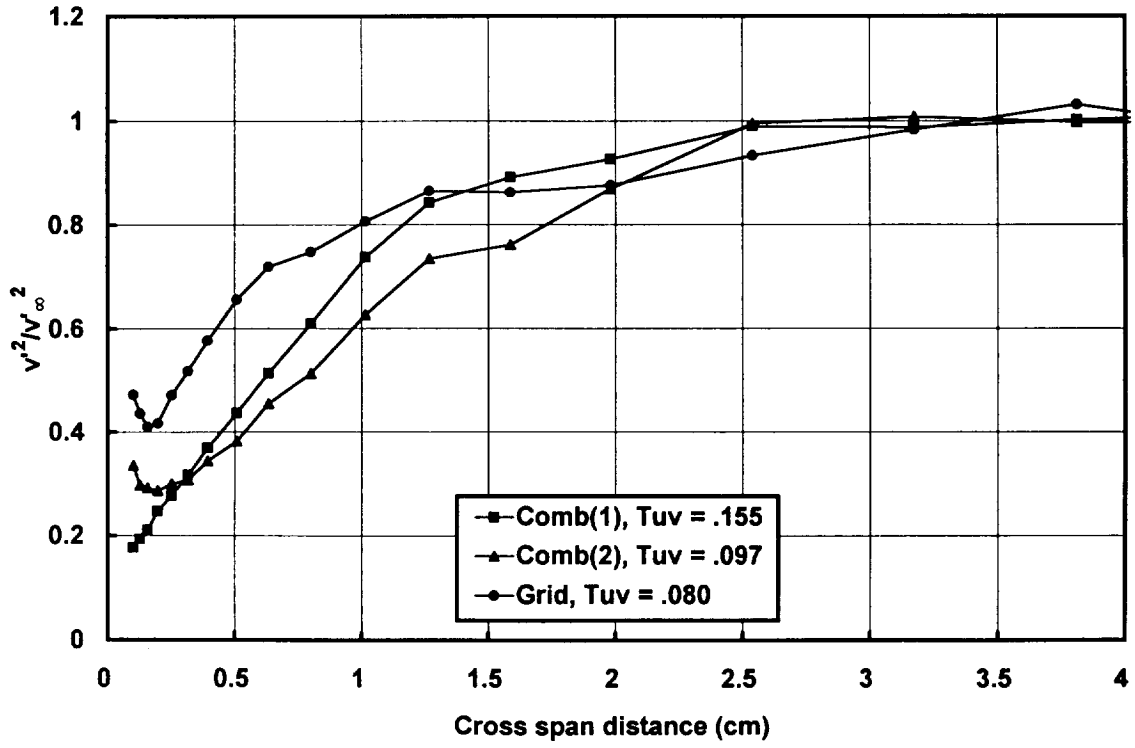

Figure 3.8 Cross span distributions of v'^2/v'^2_∞ showing near wall attenuation, U_∞ = 30 m/s

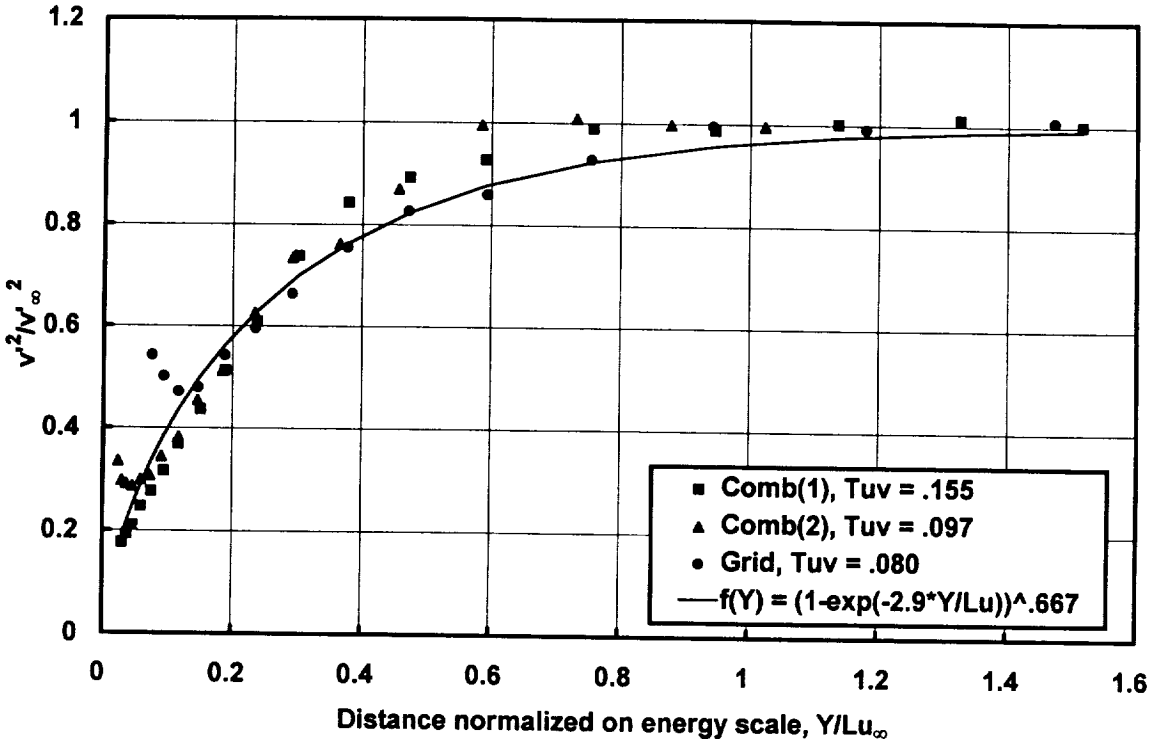

Figure 3.9 Cross span distributions of v'^2/v'^2_∞ versus Y/Lu_∞ showing near wall attenuation, U_∞ = 30 m/s

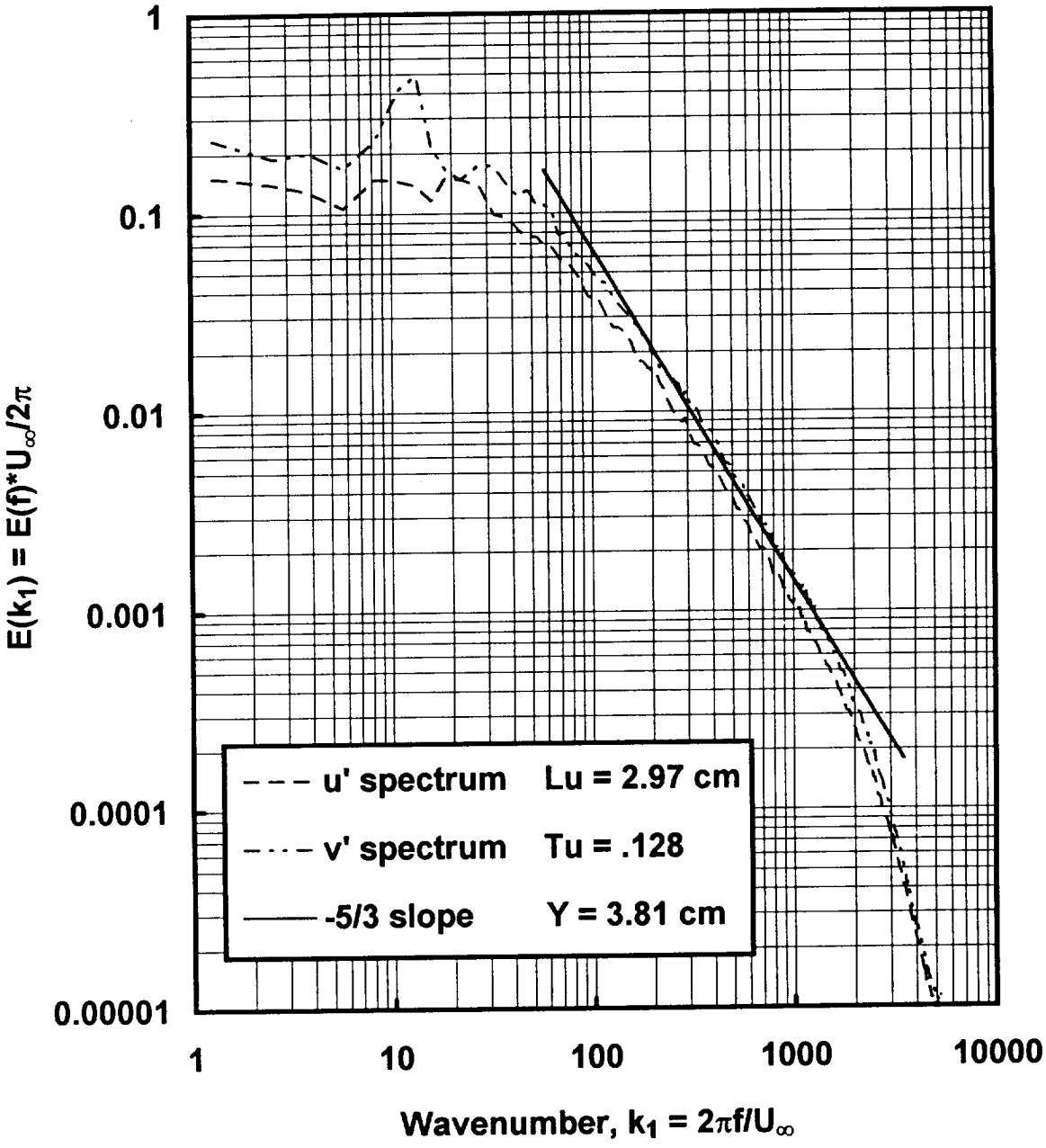

Figure 3.10 One dimensional spectra of u' and v' for Comb(1) showing inertial subrange isotropy, U_∞ = 30 m/s

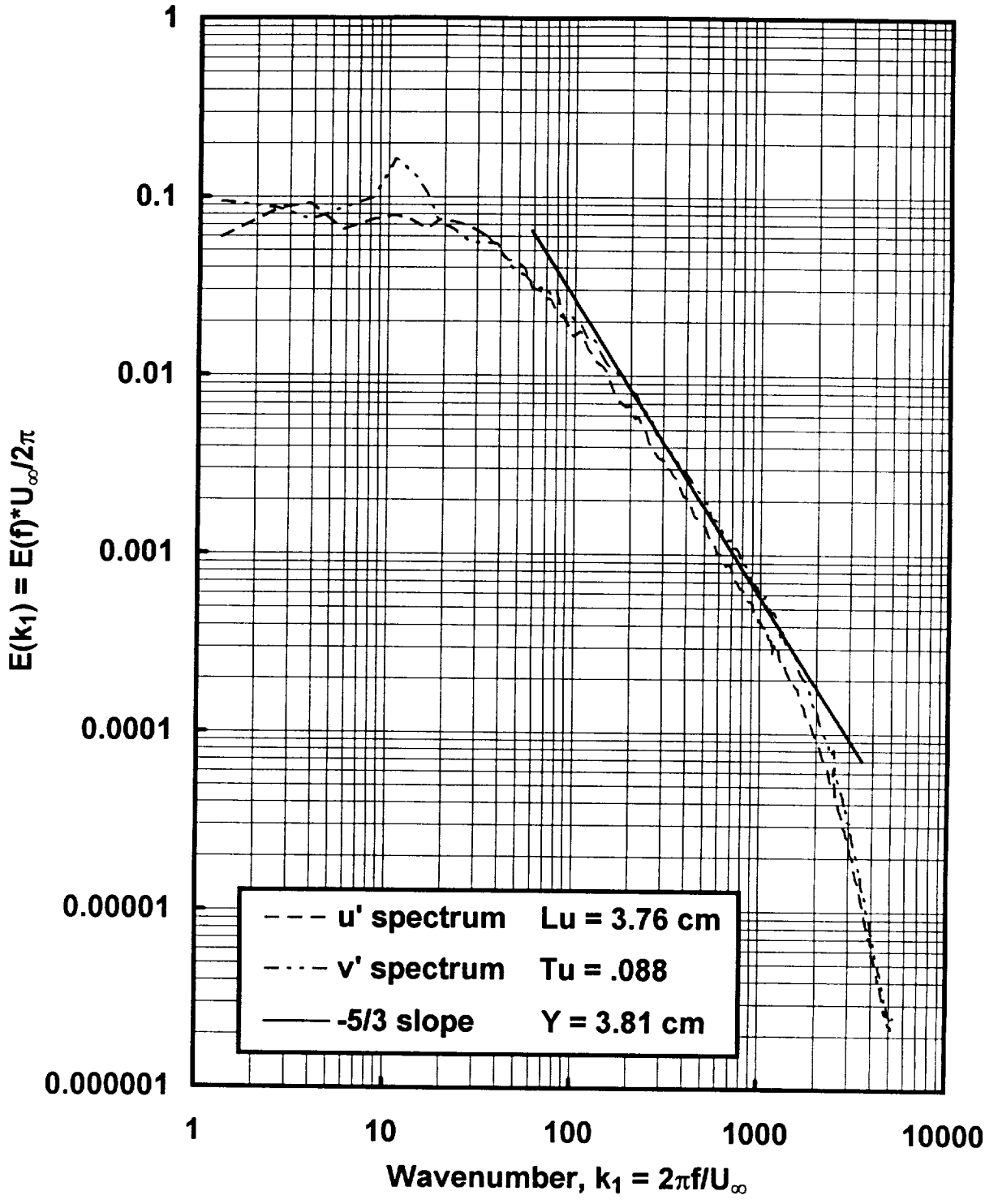

Figure 3.11 One dimensional spectra of u' and v' for Comb(2) showing inertial subrange isotropy, U_∞ = 30 m/s

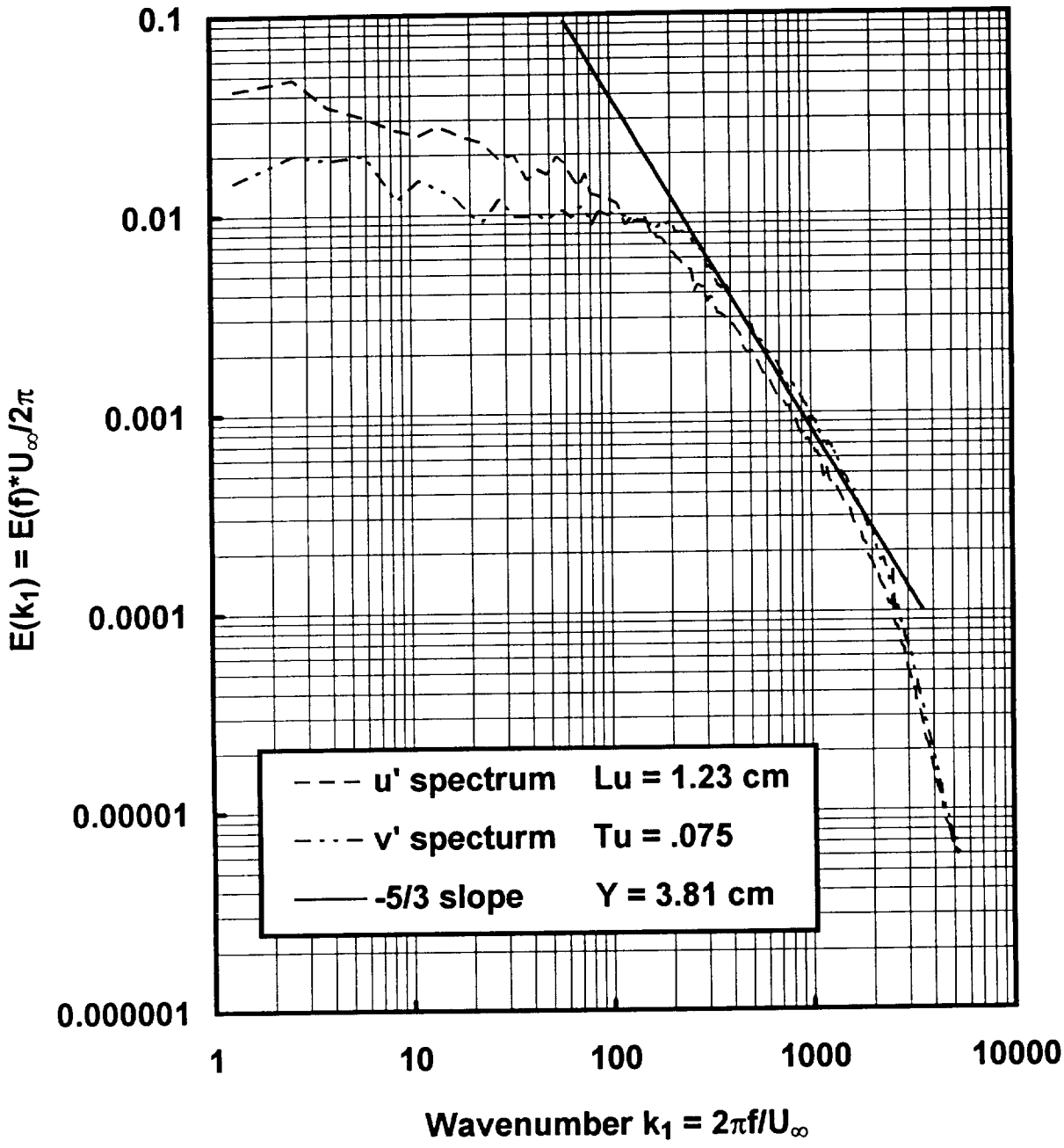

Figure 3.12 One dimensional spectra of u' and v' for grid showing inertial subrange isotropy, U_∞ = 30 m/s

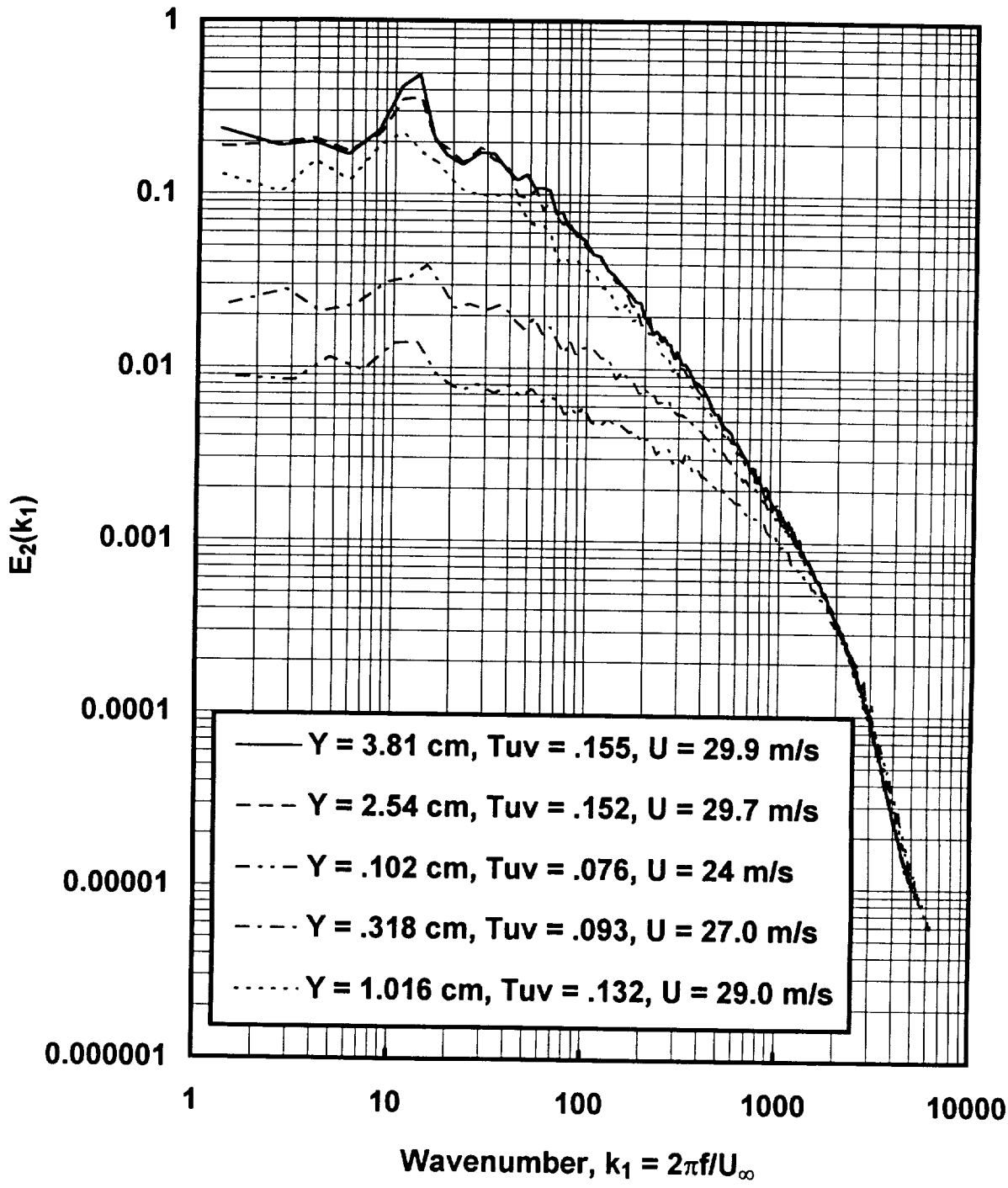

Figure 3.13 Comparison of v' spectra for various Y showing low wavenumber attenuation, Comb(1)

Chapter Four

Heat Transfer Results

This chapter examines the influence of turbulence level and scale on vane heat transfer. Initially, the baseline heat transfer data is reviewed. Next, the results of three turbulence cases are compared in terms of Stanton number for the two different Reynolds numbers. The data are also examined in terms of Stanton number augmentation comparing the three turbulence levels at constant Reynolds number and then comparing the effect of Reynolds number on the three turbulence cases. Finally, the data are compared in terms of the absolute augmentation of the heat transfer coefficient.

Baseline Results

A comparison between the experimentally determined heat transfer coefficient for the low turbulence condition and a heat transfer coefficient determined from a finite difference boundary layer calculation (STAN7) is shown in figure 4.1. The calculation used the measured pressure distribution. This comparison over the pressure surface and the laminar part of the suction surface is excellent. The start up at the stagnation point is a little off due to the difference between the actual velocity and temperature distributions and the ones input into the boundary layer code. On the suction surface, as the boundary layer develops along the adverse pressure gradient, the code calculates boundary layer separation and cannot continue. The calculated point of separation appears to be near the point where the vane has a laminar separation and then transitions. This comparison between the calculated and predicted heat transfer coefficients gives confidence in the experimental method. The difference between the data and the prediction falls within the estimated +/- 5 percent absolute uncertainty in experimental heat transfer data. The relative uncertainty in the experimental data for run to run comparison purposes is estimated to be 2.4 percent.

Stanton Number Results

The heat transfer data for the highest Reynolds number comparing the four turbulence conditions are shown in figure 4.2. The elevated turbulence data show a substantial augmentation over the low turbulence baseline case throughout the region where the boundary layer is laminar. This laminar region includes the stagnation region, all of the pressure surface, and the favorable pressure gradient portion of the suction surface. The main effect of the turbulence on the suction surface is to cause the boundary layer to transition at an earlier location. Based on our low turbulence laminar calculation for the suction surface, the transition is due to a laminar separation for the

low turbulence case. For the three elevated turbulence cases, the transition occurs earlier and the laminar heat transfer prior to that location is also elevated above the low turbulence case. These observations suggest there is no laminar separation occurring for the elevated turbulence cases. A comparison of the Stanton numbers for the turbulent portion of the suction surface shows only a mild increase in Stanton number due to the elevated levels of turbulence. Due to the large turbulence scales of this experiment relative to the thin airfoil boundary layers, the turbulence produces only a small enhancement to the turbulent boundary layer. This observation is consistent with Ames[3] who showed that relatively large scale turbulence has a significantly reduced effect on thin flat plate turbulent boundary layers.

The Stanton number data near the stagnation region of the vane show that the grid turbulence has a slightly higher augmentation than the close combustor [comb(1)] condition and a significantly higher augmentation than the far combustor condition [comb(2)]. Over the pressure surface, the increase in Stanton number due to the grid turbulence is significantly greater than the far combustor condition but lower than the close combustor condition. The legend of figure 4.2 gives values for the inlet turbulence level and scale for the four turbulence conditions showing that the grid has a lower turbulence level and smaller scale than the two combustor turbulence conditions. This result confirms that in addition to turbulence level, the turbulence scale has an important influence on heat transfer.

The heat transfer data for the lowest Reynolds number comparing the four turbulence conditions is shown in figure 4.3. The results are very similar to the results shown in figure 4.2. The main difference between the results is that the lower Reynolds number data has a lower level of augmentation.

The level of augmentation to Stanton number relative to the low turbulence case is shown in figure 4.4. The augmentation to the turbulent boundary layer on the suction surface is relatively small. The Stanton number augmentation on the leading edge, shown at 0.0 cm surface distance, ranges from about 25 percent for the far combustor position to about 36 percent for the grid. For the close combustor condition, the augmentation over the pressure surface exceeds 60 percent for most of the surface. The grid and far combustor conditions also produce a high level of augmentation on the pressure surface but lower than the close combustor condition. Figure 4.5 shows the same comparison for the lower Reynolds number cases.

The ability to predict stagnation region heat transfer is important to the reliability and efficiency of cooled vanes and blades. Ames[3] gives a correlation for stagnation region heat transfer with high free stream turbulence. A good engineering approximation to Ames' correlation is given below.

$$Nu/Re_D^{1/2} = 0.95 + 0.038\ Tu\ Re_D^{5/12}\ (Lu/D)^{-1/3}$$

An estimate for the augmentation in the stagnation region can be made by dividing the correlation through by 0.95.

$$Nu/Nu0 = 1 + 0.04\ Tu\ Re_D^{5/12}\ (Lu/D)^{-1/3}$$

Using the baseline Stanton number, inlet velocity, and vane leading edge diameter, the correlation predicted the stagnation region Stanton number of the vane within 5 percent for the three turbulence conditions and both Reynolds numbers.

Based on the work of Ames[3], for a given geometry and Reynolds number, the increase in heat transfer should scale on the free stream dissipation rate to the one-third power (or equivalently $Tu_\infty * Lu_\infty^{-1/3}$), provided the turbulence Reynolds number is high enough to support a well developed inertial subrange. Figures 3.10 through 3.12 show the turbulence generated for this study pass this criteria. This $Tu_\infty * Lu_\infty^{-1/3}$ scaling idea can be used to compare to the relative level of augmentation observed. The average augmentation for the close combustor condition was 55.6 percent over the entire pressure surface based on the average of the local values of augmentation. The grid condition had an average pressure surface augmentation of 47.8 percent which was 86 percent of the close combustor augmentation compared with an estimate based on $Tu_\infty * Lu_\infty^{-1/3}$ of 88 percent. The far combustor condition had an average pressure surface augmentation of 38.9 percent or 70 percent of the close combustor augmentation compared to an estimate based on $Tu_\infty * Lu_\infty^{-1/3}$ of 64 percent. For the lower Reynolds number, the average pressure surface augmentation for the close combustor was 46.4 percent. The low Reynolds number grid condition had an average pressure surface augmentation of 41.8 percent or 90 percent of the close combustor condition compared to an estimate of 86 percent. The low Reynolds number far combustor condition had an average augmentation of 34.2 percent which was 73 percent of the close combustor average compared to an estimate of 58 percent. The relative augmentation estimated by $Tu_\infty * Lu_\infty^{-1/3}$ generally falls within the uncertainty band of the experiment and supports this scaling argument.

Reynolds number also has an important effect on heat transfer augmentation to a laminar boundary layer. Figure 4.6 shows the augmentation for the close combustor condition at the two Reynolds numbers. This comparison is similar for the other two turbulence conditions. The influence of Reynolds number on the relative augmentation is clear by this presentation. The data for the three elevated turbulence conditions at the two Reynolds numbers allows an opportunity to estimate the Reynolds number dependence of the relative augmentation. For example, the Reynolds dependence of the grid is found to be ln(.478/.418)/ln(790,000/510,000) or .306, for the close combustor the dependence is 0.413, and is 0.294 for the far combustor. This dependence on Reynolds number averages to be 0.34. Based on the analysis of Ames, the stagnation region augmentation should scale on the 5/12 power of Reynolds

number. Similar reasoning for a flat plate laminar boundary layer suggests augmentation ought to depend on the 1/3 power of Reynolds number. These data show a dependence ranging from 0.294 to 0.413 and averaging 0.34 which is closer to the flat plate dependence.

Absolute Heat Transfer Augmentation

The absolute level of augmentation can be determined by subtracting the baseline heat transfer coefficient from the heat transfer coefficient determined for a particular turbulence condition. This absolute value in the increase in the heat transfer coefficient is shown in figure 4.7 for the higher Reynolds number condition. The stagnation region shows the highest absolute increase in the value of heat transfer coefficient except at the point of early transition. The absolute augmentation on the pressure surface is about 25 to 35 percent lower than the peak increase in the stagnation region. The absolute levels of augmentation for the lower Reynolds number tests, shown in figure 4.8, have similar trends to those shown in figure 4.7 but are about 30 percent lower in absolute level.

Conclusions

The present data demonstrate that the length scale, Lu, has a significant effect on stagnation region and pressure surface heat transfer. The average heat transfer from over the pressure surface was found to scale reasonably well on the relative level of dissipation. The stagnation region heat transfer correlated well on the $\{Tu\ Re_D^{5/12}\ (Lu/D)^{-1/3}\}$ parameter of Ames. The dependence of heat transfer augmentation on Reynolds number was estimated to scale on the 1/3 power for the pressure surface. The absolute level of heat transfer coefficient was found to be highest near the stagnation region and declined to about 70 percent of that value over the rest of the pressure surface. The close combustor at a Reynolds number of 800,000 had an average augmentation on the pressure surface of 56 percent.

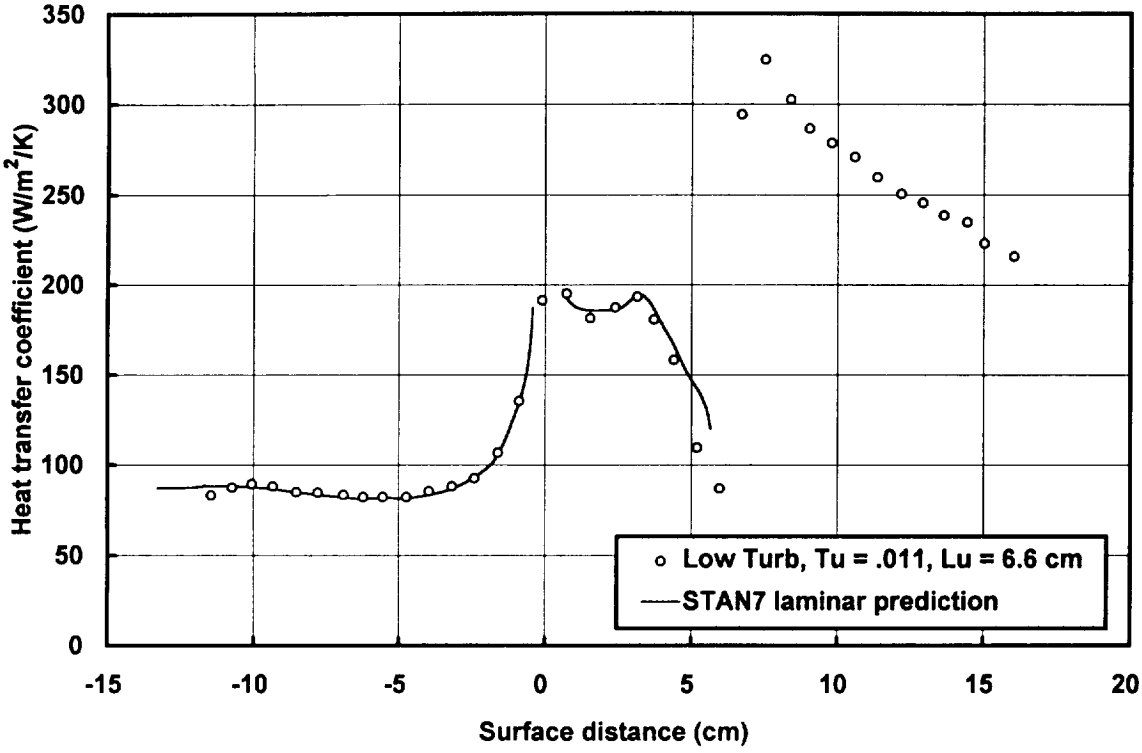

Figure 4.1 Comparison of baseline heat transfer test with STAN7 calculation, Re_{ex} = 780,000, Ma_{ex} = 0.27

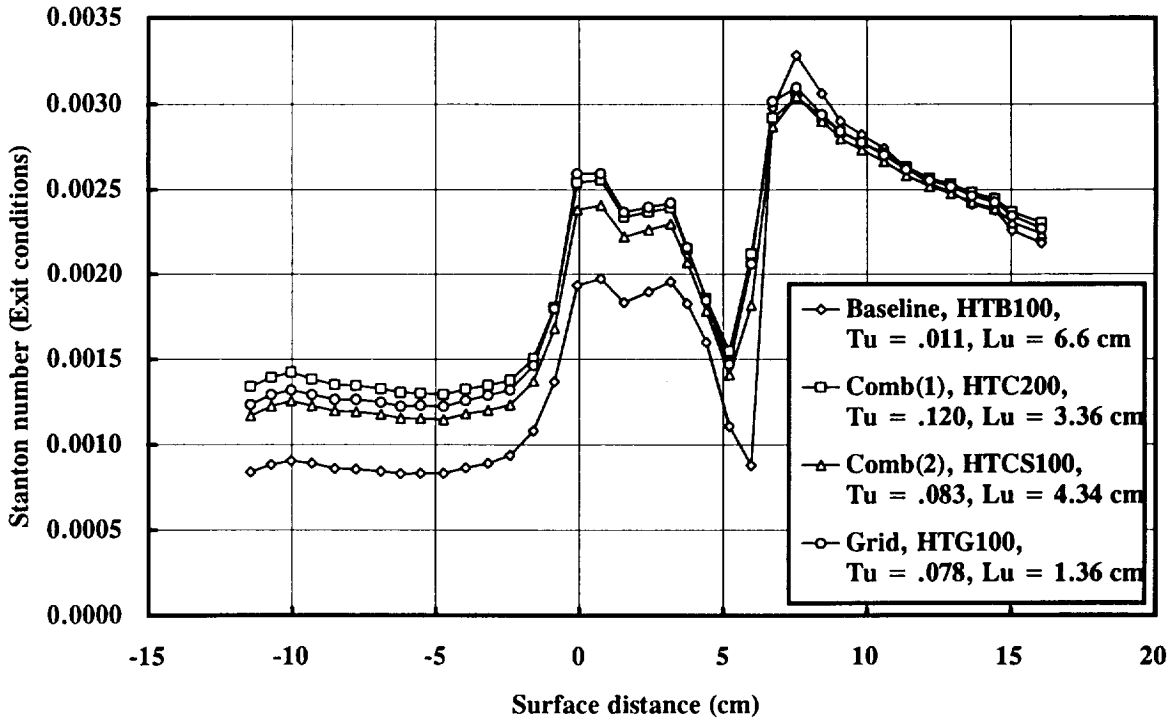

Figure 4.2 Comparison of Stanton number distribution showing effects of turbulence, Re_{ex} = 780,000

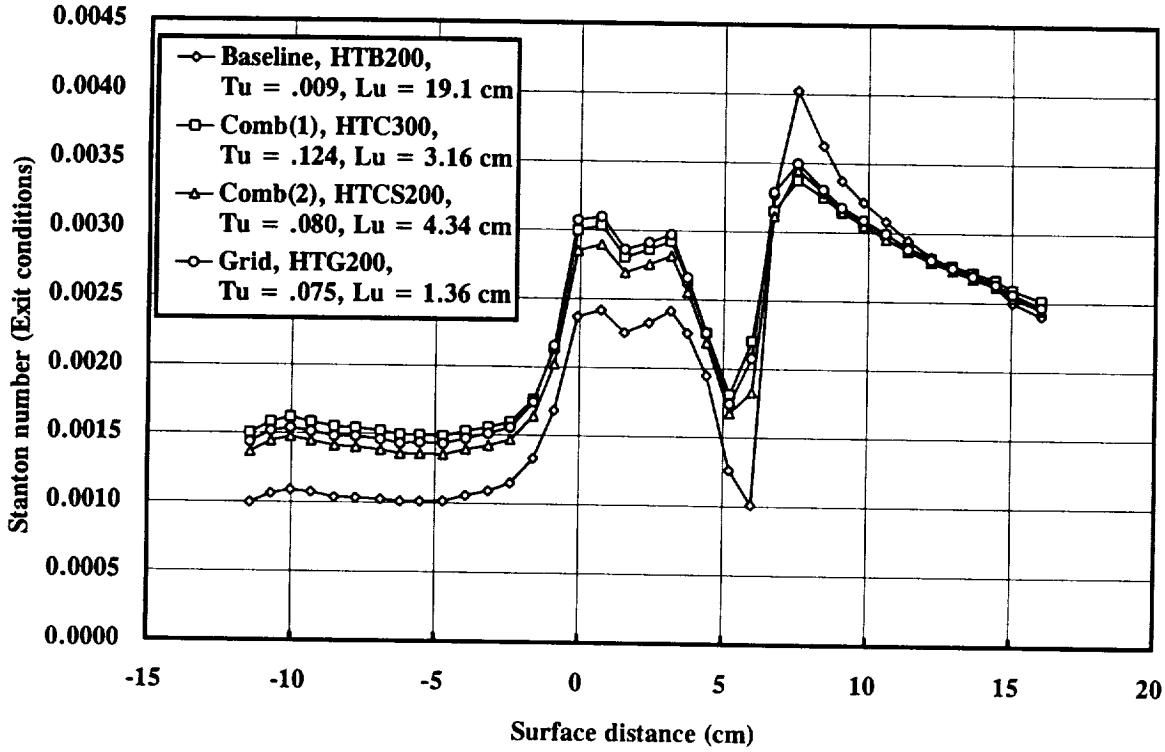

Figure 4.3 Comparison of Stanton number distribution showing effects of turbulence, Re_{ex} = 510,000

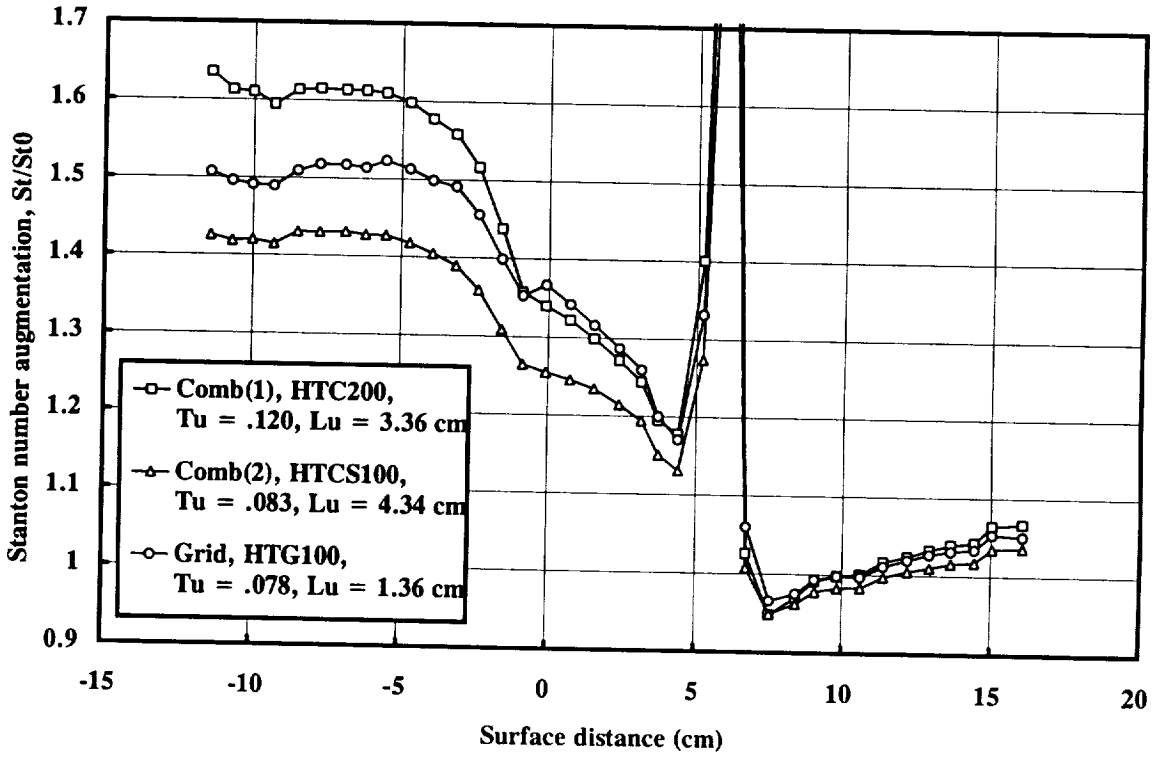

Figure 4.4 Influence of turbulence on heat transfer augmentation, Re_{ex} = 790,000

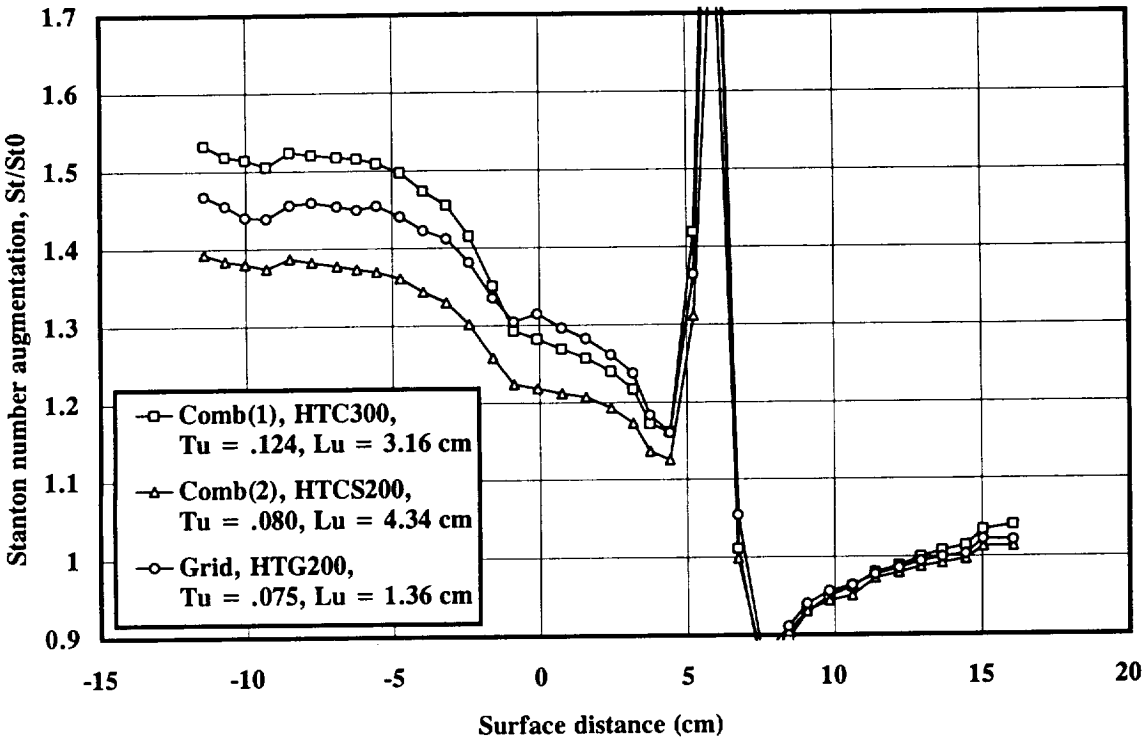

Figure 4.5 Influence of turbulence on heat transfer augmentation, Re_{ex} = 510,000

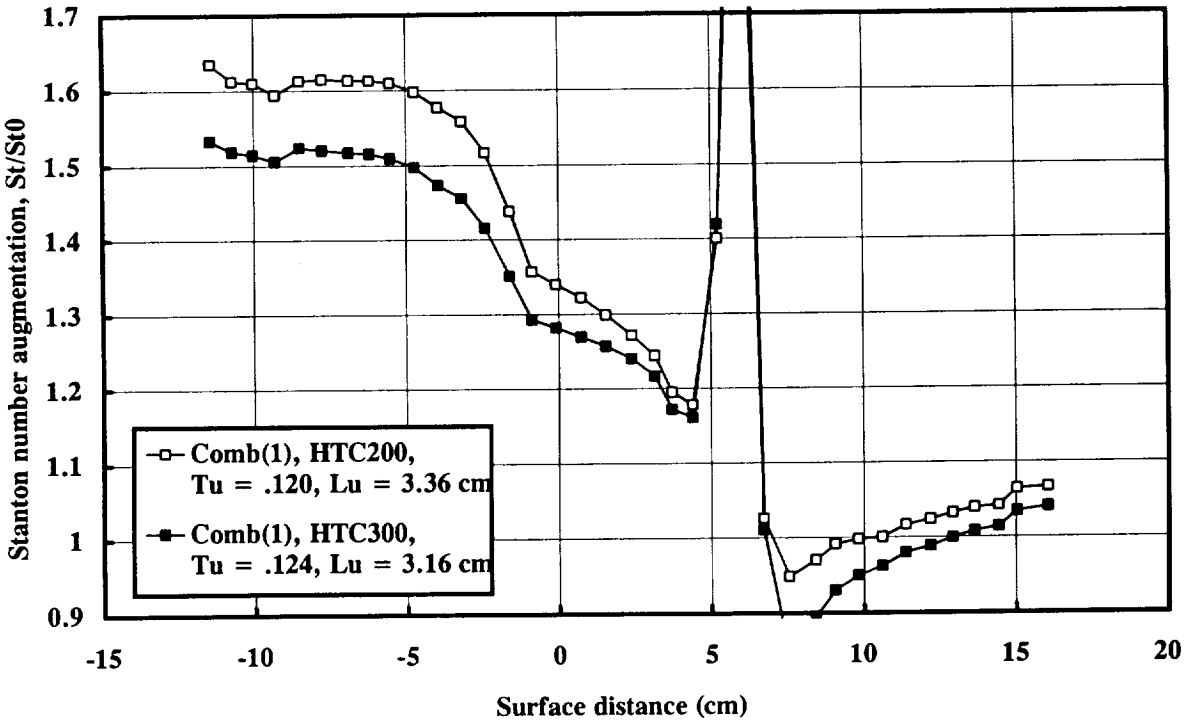

Figure 4.6 Influence of Reynolds number on heat transfer augmentation, Comb(1)

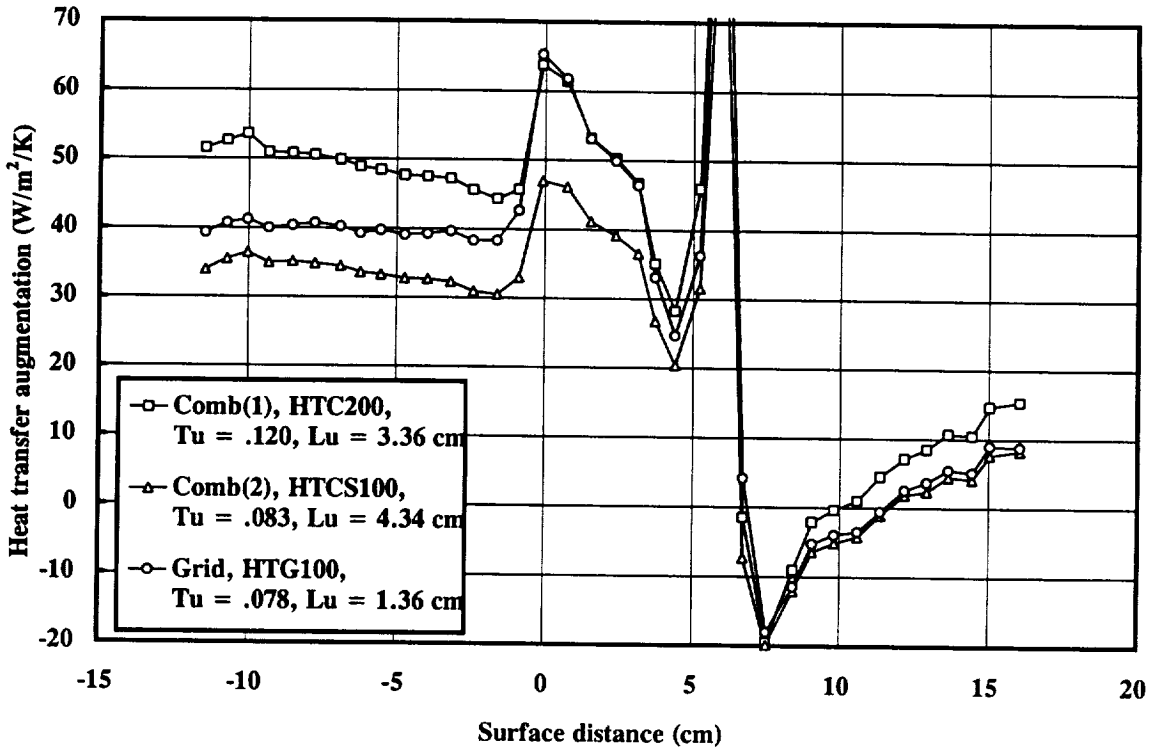

Figure 4.7 Comparison of absolute level of heat transfer augmentation, Re_{ex} = 790,000

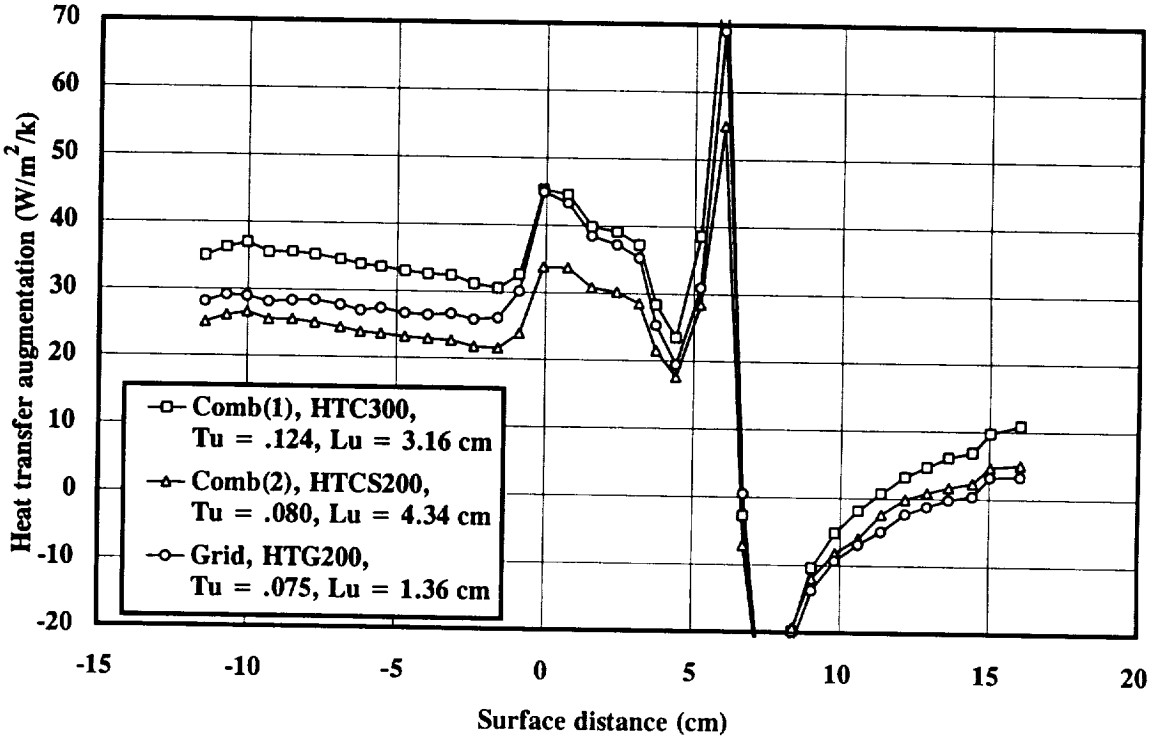

Figure 4.8 Comparison of absolute level of heat transfer augmentation, Re_{ex} = 510,000

Chapter Five

Intrapassage Turbulence

The pressure surface of a turbine airfoil is known to produce levels of heat transfer well above laminar estimates. The stagnation region of an airfoil sees similar levels of heat transfer augmentation. Based on the work of Hunt and Britter, Hunt, and Mumford, the high rates of strain near the stagnation region allow turbulence to penetrate close to the surface. Ames [3] and Van Fossen [13,14] have both found that length scale has a strong influence on stagnation region heat transfer. Ames believes the straining mechanism reported by Hunt and Britter is responsible.

The pressure surface of a vane is similar to a wedge flow, the velocity accelerates along the total length. Straining rates are lower than around a stagnation region but may be high enough to be responsible for intensification of the near wall turbulence and its resulting effect on heat transfer. If this mechanism is present then enhanced dissipation rates relative to inlet levels will be observed as the wall is approached. The objective of the present chapter is to examine the experimental data in order to look for evidence to support or to reject this hypothesis.

Experimental Measurements

The single wire and X-wire data taken across the passage during this investigation were made using a probe that pivoted around a downstream location. The probe access positions and the arcs made by the single wire probe in that position are shown in figure 5.1. The pivots afforded good access to both the intrapassage region of the flow and exit positions. The intrapassage measurements were taken from pivot positions 1 through 4 and all distances are reported as distances normal to the pressure surface. In the intrapassage position, the probe pivot caused some downstream blockage which was not accounted for in these measurements.

The probe length from pivot center was nominally 14.73 cm long. The actual length of the single wire and X-wire probes were 14.32 cm and 14.56 cm respectively. This difference between nominal and actual probe lengths means the single wire and X-wire traverses occurred in slightly different positions.

The intrapassage velocities for the three turbulence conditions taken at the four positions are shown in figure 5.2. The velocity data shows both a strong acceleration along the surface and a slight increase going away from the surface. The effect of the turbulence can be seen by the thickness of the boundary layers. The outer region of the boundary layer is thickened by the eddy diffusivity of the free stream turbulence.

Based on an integral calculation and typical laminar shape factors, a laminar boundary layer would range in thickness from .041 cm to .027 cm at the four points along the pressure surface. Based on the single wire measurements, the boundary layer thicknesses shown in figure 5.2 range from about .16 cm to .1 cm. The profile at the highest velocity is taken from position four. The arc of the single wire probe tip intersects the vane in the trailing edge region of the airfoil so the resulting near surface profile is more of a wake than a boundary layer. The velocity profile taken off the suction surface at the same location shows a relatively thick turbulent boundary layer developing downstream of the adverse pressure gradient. Based on exit measurements, this suction surface profile accounts for a significant portion of the vane exit losses.

Turbulence Measurements

Cross passage RMS streamwise fluctuation velocity profiles taken with a single wire are shown in figures 5.3 through 5.5 for the three elevated turbulence conditions. Figure 5.3 shows a comparison of $|u'|$ at the four pivot locations. The level of u' is strongly attenuated in the streamwise direction. The fact that this is attenuation and not decay is clear from the streamwise distribution of dissipation which remains approximately constant as shown in tables 5.1 through 5.4. Strong streamwise acceleration tends to suppress longitudinal fluctuations. Near the wall, the level of u' increases. This is due to the blocking of v' by the surface which tends to redirect v' fluctuations into the u' and w' components. Also, in the very near wall region, production appears to be occurring. The profiles for the combustor with spool section and for the grid show similar features. However, the streamwise suppression of u' is not as large for the grid turbulence.

One dimensional u' spectra taken at the inlet and at the four intrapassage positions using a single wire probe are shown in figure 5.6. The position of the probe normal to the pressure surface was 0.4 inches for the four intrapassage locations. For the inlet condition and position 1, a 5 micrometer diameter 1.25 mm long platinum coated tungsten wire was used. For positions 2 through 4, a 2.5 micrometer diameter 0.50 mm long platinum coated tungsten wire was used. The high wavenumber spectra of the large wire show evidence of filtering due to averaging the eddies over the length of the wire. In general, the tangent point of the -5/3 slope is close for all 5 profiles indicating that the small scales or higher wavenumber spectra are not measurably affected by the streamwise straining. The large eddies or lower wavenumber spectra are strongly suppressed by the streamwise straining. In fact, the slope of the flat portion of the spectra changes from -5/3 to about -1. This range of slopes is most likely specific to this particular experiment.

Velocity time records were taken with a single wire at 6 locations normal to the pressure surface for each of three turbulence conditions at four different streamwise positions. Results of the analyses of this data are given in tables 5.1 through 5.4. One

parameter of key interest was the dissipation level. If the intensification of turbulence is present along the pressure surface of the vane, we would expect to see an increase in dissipation as the wall was approached. Based on flat plate data where no intensification is expected, the dissipation remains constant in the direction normal to the wall until well within the boundary layer where production begins to become an influence. Based on the present data at position 1, we see an increase in the dissipation level approaching the wall. At position 1, the 99 percent thickness of the boundary layer is about 0.15 cm. Within this region it would be difficult to determine whether the increase in dissipation was due to production within the turbulence enhanced laminar boundary layer or due to straining in the free stream. At position 1, the combustor with the ten inch spool shows an increase in dissipation outside the boundary layer. At position 2, where the boundary layer is about 0.13 cm thick, both the close combustor and the grid show mildly enhanced dissipation levels at the edge of the boundary layer while the combustor with spool shows a very significant amplification at the edge and outside of the boundary layer. At position 3, where the boundary layer is about 0.10 cm thick, only the combustor with spool shows a significantly elevated dissipation level outside of the boundary layer.

Table 5.3 shows another very interesting aspect about the turbulence. For all three turbulence cases, the dissipation just off the suction surface shows a significantly reduced level. The probe is located just on the backside of the vane downstream of a significant region of convex curvature.

Cross passage distributions for the normal component of turbulence at the four streamwise positions are shown for the three turbulence cases in figure 5.7 through 5.9. Figure 5.7 shows how the v' component of turbulence grows in the streamwise direction as the flow accelerates along the passage for the close combustor. The attenuation of v' is confined closer to the wall region than for the inlet turbulence (see figure 3.8). The y/Lu scaling of v'^2 no longer applies in this region. In the near wall region at positions 3 and 4, the near wall upswing in v' indicates that the near wall production of turbulence is occurring. Figures 5.8 and 5.9 show the same general trends for the combustor with spool and the grid turbulence respectively.

The normal distribution of the v' component of turbulence is shown in figure 5.10 comparing the three turbulence cases at position 1. The grid and combustor with spool have nearly identical distributions while the level of v' for the close combustor is significantly greater. Figure 5.11 shows the same comparison at position 4. The data indicates that the turbulence is amplified significantly more for the combustor with spool than for the grid. The difference in time scales [Lu/|u'|] is the likely cause. When the time scale of the turbulence is large in comparison with the rate of strain [1/(dU/dx)] the turbulence does not have time to react to the straining of the flow so the turbulent eddies are deformed along with the flow. This rapid straining can produce significant anisotropies in the turbulence. The turbulence of the combustor

with spool has a lot of large eddies that react slowly and the longitudinal fluctuations are suppressed by the streamwise straining while the lateral fluctuations tend to be intensified.

The development of the v' spectra in the streamwise direction is shown in figure 5.12 for the close combustor. The spectra show a significant increase in the lower wavenumbers but no increase is evident in the higher wavenumbers. The lower wavenumber spectra appear to fill out the inertial subrange [-5/3 slope region].

The isotropy of the turbulence at position 1 is shown in figure 5.13 for the close combustor. The turbulence conforms closely to the isotropy relationship $E_2(k_1) = 4/3*E_1(k_1)$ in the inertial subrange region. Figure 5.14 shows the contrasting relationship for spectra taken at position 4. Here, the turbulence is strongly anisotropic except perhaps for a small region of relatively high wavenumber eddies where the $E_2(k_1) = 4/3*E_1(k_1)$ relationship seems to hold. Notice how the anisotropy of the scales increases with decreasing wavenumber.

In the inlet conditions section figure 3.9 compared v'^2 as a function of y/Lu and found that the distribution away from the wall correlated well. Inside the turbine passage, the normal distribution of v'^2 has a steeper near wall slope outside of the pressure surface as compared to outside of a zero velocity gradient boundary layer. Figure 5.15 shows a comparison of free stream normalized v'^2 distributions for the three turbulence conditions at position 2. The grid with the smallest scale has the sharpest near wall distribution. The close combustor with an inlet scale between the grid and the combustor with spool has the least abrupt near wall distribution and the combustor with spool, having the largest inlet scale is in between. Previously, the combustor with spool condition had shown the largest effect in its near wall dissipation distributions. Evidently, this amplification effect on the large scale turbulence modified the near wall turbulence distributions. Otherwise, we would expect the close combustor to have a steeper profile than the combustor with spool. Figure 5.16 shows the normal distributions of v'^2 as a function of y/Lu and the data clearly show that y/Lu in itself is no longer a valid scaling parameter for the pressure side distribution.

The previous two figures showed how v'^2 was attenuated off the pressure surface at position 2. Figure 5.17 shows v' spectra at different locations off the pressure surface at position 2. A comparison of figure 5.17 with figure 3.13, which shows the same type of distribution at the inlet to the cascade, indicates that the v' attenuation is different at the two locations. Off the pressure surface of the vane, the normal component of turbulence penetrates closer to the pressure surface boundary layer.

Summary and Conclusions

The data presented in this chapter demonstrated how the mean level of u' fluctuations were attenuated through the passage while the mean level of v' fluctuations increased as the flow accelerated. A careful examination of the spectra revealed that most of this change occurred in the larger eddies or the low wavenumber spectra while the highest wavenumber spectra remained unaffected. When the dissipation level of the u' spectra was examined normal to the pressure surface, some intensification was seen outside of the boundary layer. This intensification was most predominate for the combustor with spool which had the largest turbulent time scale.

One of the key elements of Hunt's work was the idea of rapidly distorting a turbulent flow. Basically, a turbulent flow is rapidly distorted when the time scale of straining [1/(dU/dx)] is much much smaller than the time scale of the turbulence [Lu/|u'|]. The vane cascade has a time scale along the pressure surface of about 1.7 milliseconds. The close combustor, the combustor with spool, and the grid have time scales of about 9, 17, and 6 milliseconds respectively. These time scales are on the slow end of being rapid for the turbine passage. The combustor with spool had the largest time scale and the biggest reaction to both the near wall straining and the streamwise straining. The grid turbulence with the smallest time scale shows the least reaction to the streamwise straining and only a modest near wall reaction. The time scale of the turbulence really changes with the wavenumber. In the inertial subrange, for a given dissipation level, the time scale of the turbulence should scale on $k_1^{-2/3}$. This observation suggests that small scale eddies should adjust to straining more quickly than larger eddies and therefore be less affected by it. The streamwise u' spectra clearly show the smaller eddies are less affected which is consistent with a smaller time scale.

The heat transfer data in chapter 4 demonstrated that the combustor with spool had a high augmentation relative to the $Tu*Lu^{-1/3}$ scaling factor at constant Reynolds number. In light of the present data, the near wall straining of the combustor with spool turbulence appears to be responsible for this variation. Based on the values of dissipation determined outside the boundary layer, the amplification of turbulence, while present, does not appear to be the major influence to pressure surface augmentation in the present data. At higher chord Reynolds numbers, this conclusion may no longer be true due to the decreasing relative thickness of the boundary layer. The thinner boundary layer allows a greater degree of straining to occur outside the boundary layer.

In conclusion, the passage and near wall straining of turbulence in the present experiment produced significant anisotropies in the low wavenumber eddies, but the relatively high wavenumbers remained largely unaffected. A near wall increase in the

dissipation rate was found outside the pressure surface boundary layer but it appeared to be insufficient to produce a dramatic effect on heat transfer. The flow field turbulence did cause significant levels of turbulent production within the pressure surface boundary layer. This boundary layer production appears to be the mechanism responsible for the high levels of heat transfer augmentation found on the pressure surface.

Table 5.1 Intrapassage turbulence data for position 1

	File	Tu	Vel (m/s)	Lx (cm)	Lu (cm)	Diss (m^2/s^3)	Y (cm)
Comb(1)	IP1C1	0.1720	22.00	0.897	1.892	4295	0.037
	IP1C2	0.1388	26.41	1.120	2.664	2776	0.099
	IP1C3	0.1147	28.10	1.359	2.299	2199	0.309
	IP1C4	0.1130	28.72	1.514	2.414	2126	0.987
	IP1C5	0.1152	30.38	1.603	3.297	1950	1.975
	IP1C6	0.1152	32.51	1.608	3.747	2104	2.962
Comb(2)	IP1CS1	0.1354	23.47	1.194	2.344	2051	0.037
	IP1CS2	0.1106	26.13	1.511	2.797	1296	0.099
	IP1CS3	0.0844	27.83	1.814	2.593	749	0.309
	IP1CS4	0.0813	28.25	1.877	3.119	582	0.987
	IP1CS5	0.0810	29.92	1.905	4.013	533	1.975
	IP1CS6	0.0812	31.87	2.037	4.562	570	2.962
Grid	IP1G1	0.1320	21.90	0.813	1.692	2140	0.037
	IP1G2	0.0983	25.52	0.998	1.654	1430	0.099
	IP1G3	0.0662	27.51	0.894	0.955	949	0.309
	IP1G4	0.0691	28.25	1.234	1.240	898	0.987
	IP1G5	0.0708	30.54	1.572	1.537	989	1.975
	IP1G6	0.0695	32.14	1.255	1.410	1188	2.962

Table 5.2 Intrapassage turbulence data for position 2

	File	Tu	Vel (m/s)	Lx (cm)	Lu (cm)	Diss (m^2/s^3)	Y (cm)
Comb(1)	IP2C1	0.1017	39.80	0.932	1.074	9254	0.062
	IP2C2	0.0744	42.95	1.115	1.857	2633	0.123
	IP2C3	0.0651	43.96	1.168	1.245	2831	0.309
	IP2C4	0.0604	45.06	1.311	1.270	2385	0.987
	IP2C5	0.0634	47.28	1.651	1.811	2233	1.975
	IP2C6	0.0648	49.86	1.443	2.195	2306	2.962
Comb(2)	IP2CS1	0.0903	40.22	1.021	1.311	5481	0.062
	IP2CS2	0.0557	43.70	1.478	1.758	1230	0.123
	IP2CS3	0.0476	44.49	1.689	1.471	966	0.309
	IP2CS4	0.0429	45.73	1.814	1.778	639	0.987
	IP2CS5	0.0422	48.19	2.027	2.286	551	1.975
	IP2CS6	0.0430	50.74	2.163	2.893	537	2.962
Grid	IP2G1	0.0907	39.70	0.833	1.219	5737	0.062
	IP2G2	0.0444	43.55	1.067	0.922	1172	0.123
	IP2G3	0.0369	44.33	1.036	0.599	1100	0.309
	IP2G4	0.0356	45.19	1.166	0.681	916	0.987
	IP2G5	0.0406	47.15	2.197	0.963	1094	1.975
	IP2G6	0.0403	50.08	1.552	0.978	1259	2.962

Table 5.3 Intrapassage turbulence data for position 3

	File	Tu	Vel (m/s)	Lx (cm)	Lu (cm)	Diss (m^2/s^3)	Y (cm)
Comb(1)	IP3C1	0.0477	68.30	1.072	1.237	4202	0.062
	IP3C2	0.0383	69.60	1.199	1.267	2247	0.123
	IP3C3	0.0342	70.60	1.217	0.942	2249	0.309
	IP3C4	0.0312	72.90	1.275	0.876	2012	0.987
	IP3C5	0.0305	79.35	1.613	0.988	2163	1.975
	IP3C6	0.0257	93.03	1.041	1.750	1447	2.962
Comb(2)	IP3CS1	0.0370	69.09	1.608	1.344	1867	0.062
	IP3CS2	0.0272	70.21	1.684	1.354	769	0.123
	IP3CS3	0.0246	71.24	2.085	1.067	761	0.309
	IP3CS4	0.0210	73.51	3.112	1.207	461	0.987
	IP3CS5	0.0206	80.03	3.373	1.331	502	1.975
	IP3CS6	0.0180	93.56	4.338	2.626	271	2.962
Grid	IP3G1	0.0358	68.70	1.488	0.998	2229	0.062
	IP3G2	0.0246	69.80	1.598	0.846	895	0.123
	IP3G3	0.0209	70.69	1.895	0.513	939	0.309
	IP3G4	0.0199	73.15	2.459	0.513	906	0.987
	IP3G5	0.0197	79.60	2.896	0.599	971	0.975
	IP3G6	0.0189	92.96	2.540	1.168	690	2.962

Table 5.4 Intrapassage turbulence data for position 4

	File	Tu	Vel (m/s)	Lx (cm)	Lu (cm)	Diss (m^2/s^3)	Y (cm)
Comb(1)	IP4C2	0.0332	91.95	1.590	0.792	5370	0.123
	IP4C3	0.0260	91.10	1.372	0.815	2457	0.309
	IP4C4	0.0241	90.30	1.496	0.650	2366	0.987
	IP4C5	0.0244	92.65	1.961	0.777	2235	1.975
	IP4C6	0.0266	95.82	1.712	0.587	4214	2.962
Comb(2)	IP4CS2	0.0257	91.40	2.019	0.632	3064	0.123
	IP4CS3	0.0170	90.92	2.992	0.792	693	0.309
	IP4CS4	0.0170	89.75	2.756	1.242	432	0.987
	IP4CS5	0.0161	91.71	3.807	1.247	387	1.975
	IP4CS6	0.0178	94.82	2.304	0.958	749	2.962
Grid	IP4G2	0.0205	91.59	2.451	0.460	2152	0.123
	IP4G3	0.0160	90.55	2.499	0.536	852	0.309
	IP4G4	0.0155	89.31	2.464	0.462	860	0.987
	IP4G5	0.0165	91.80	3.127	0.511	1012	1.975
	IP4G6	0.0173	95.09	2.283	0.378	1753	2.962

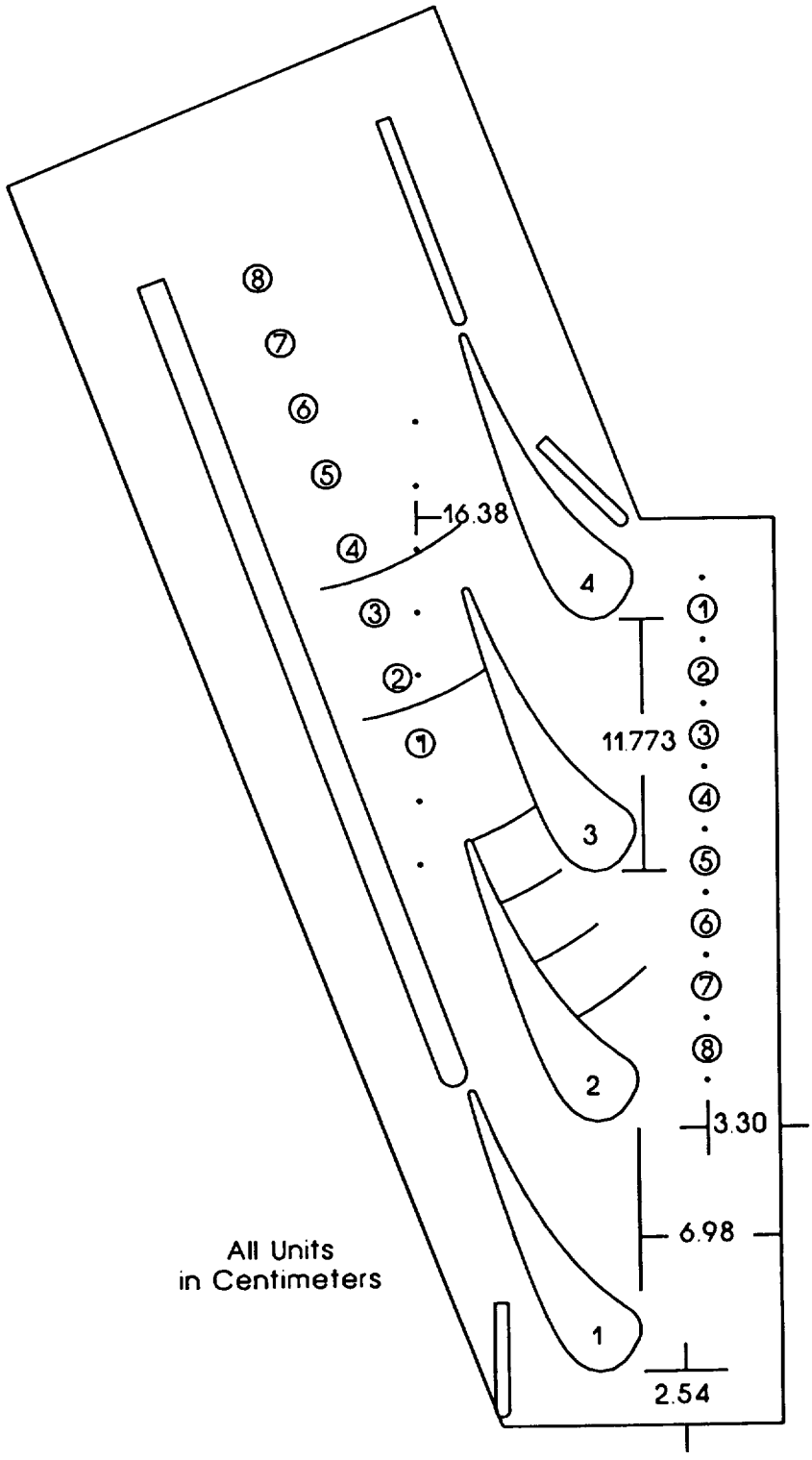

Figure 5.1 Schematic of cascade showing locations of intrapassage and exit measurements

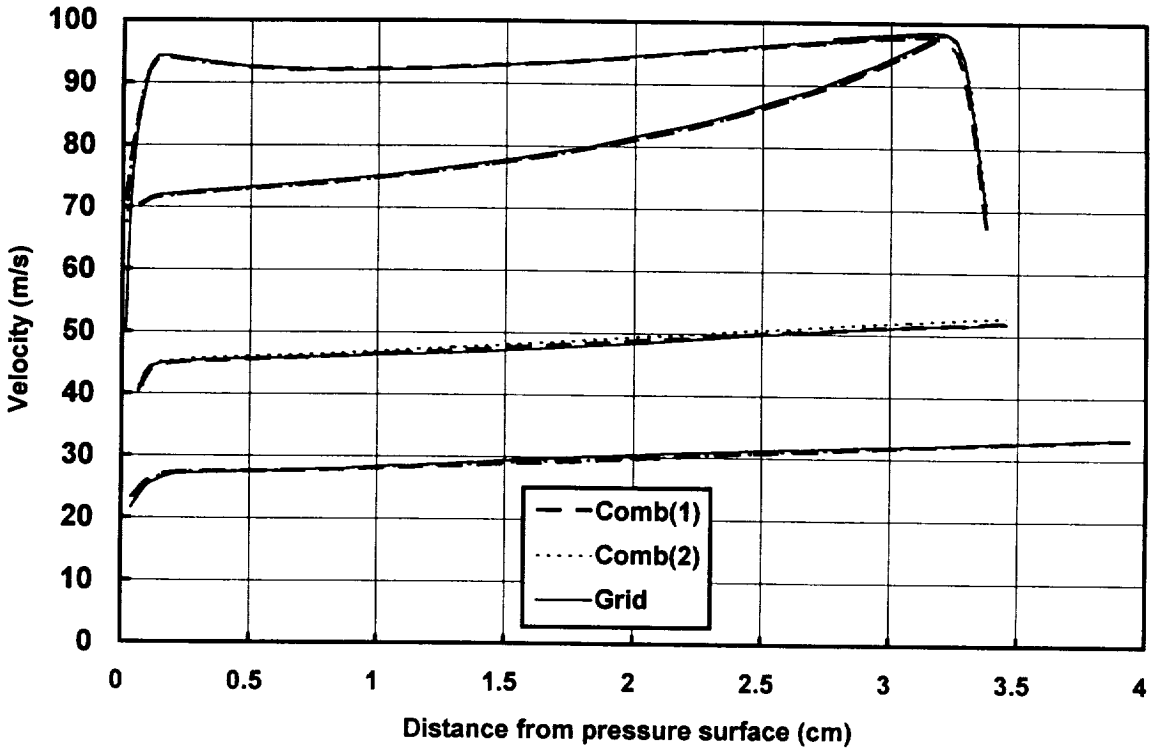

Figure 5.2 Intrapassage single wire velocity measurements at survey locations 1 through 4

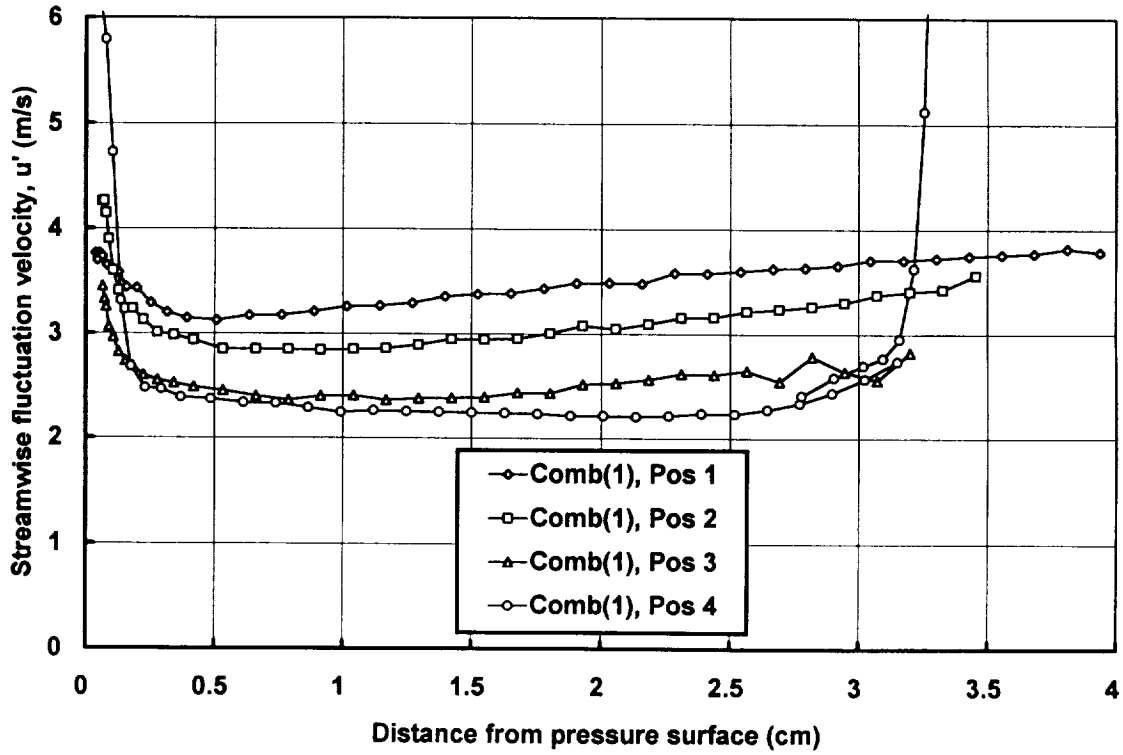

Figure 5.3 Intrapassage distributions of u' at locations 1 through 4, Comb(1)

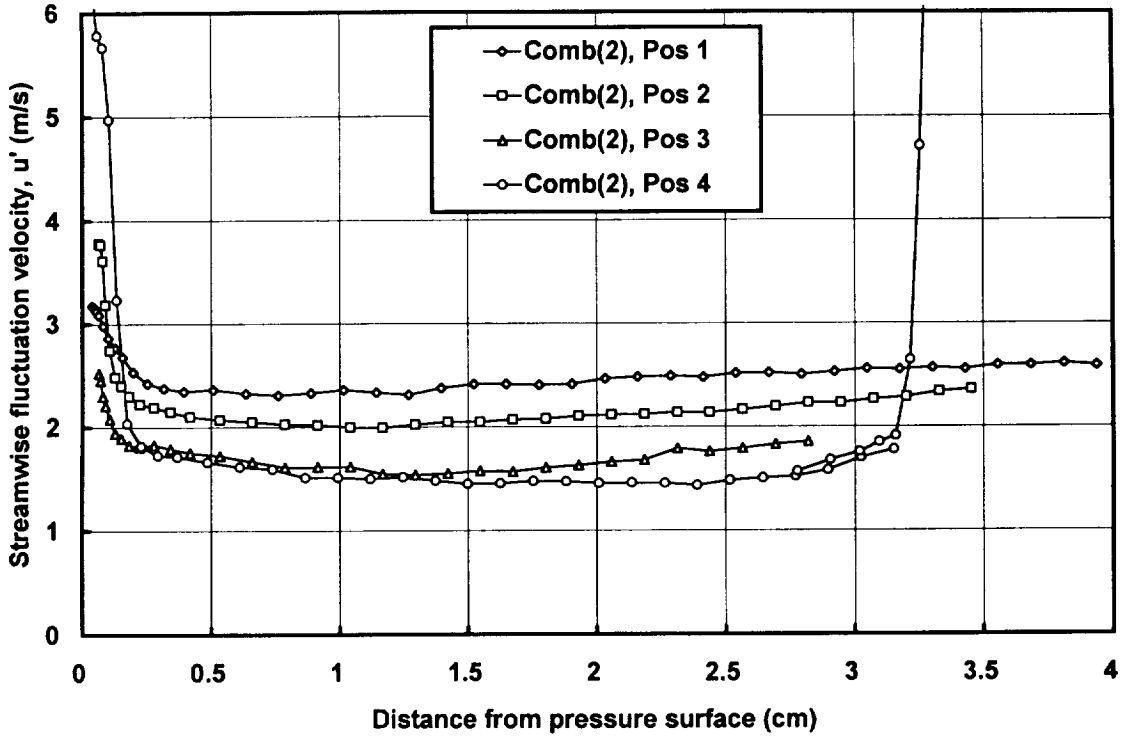

Figure 5.4 Intrapassage distributions of u' at locations 1 through 4, Comb(2)

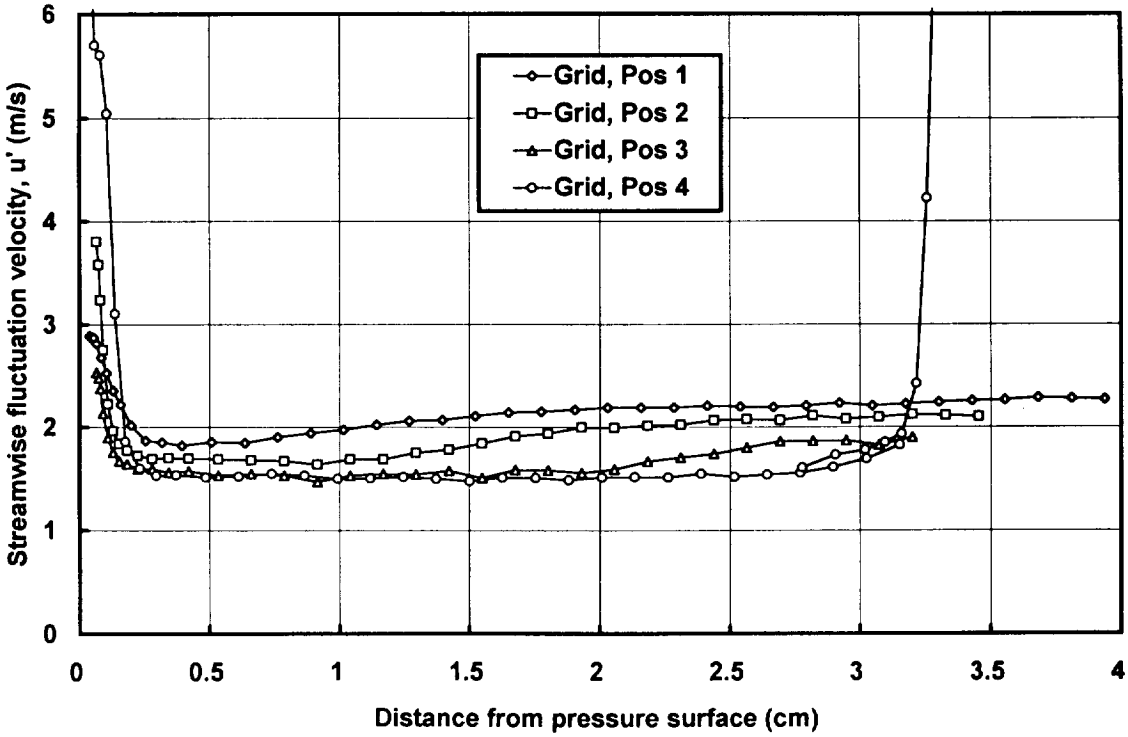

Figure 5.5 Intrapassage distributions of u' at locations 1 through 4, Grid

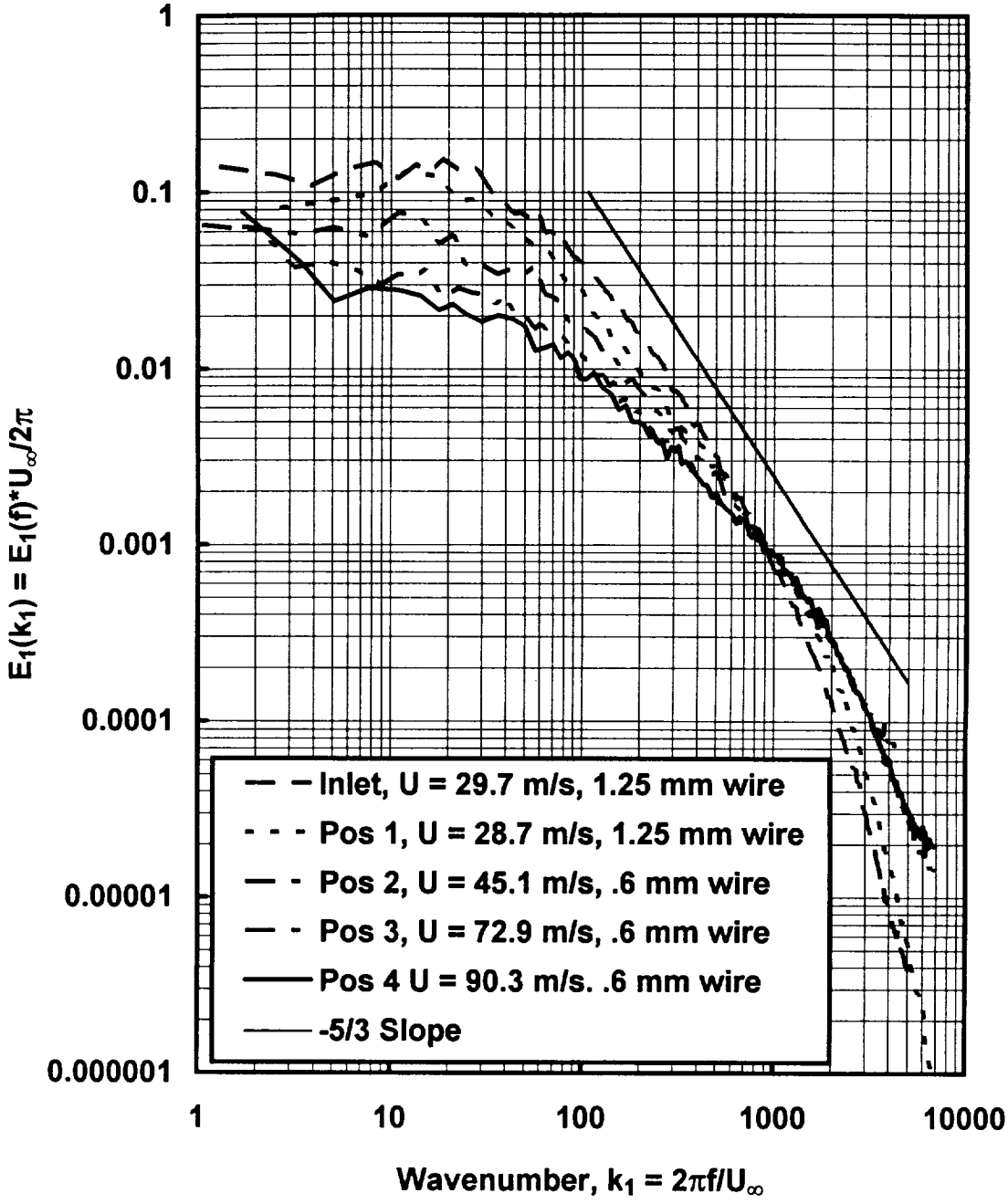

Figure 5.6 Development of u' spectra through turbine passage for Comb(1)

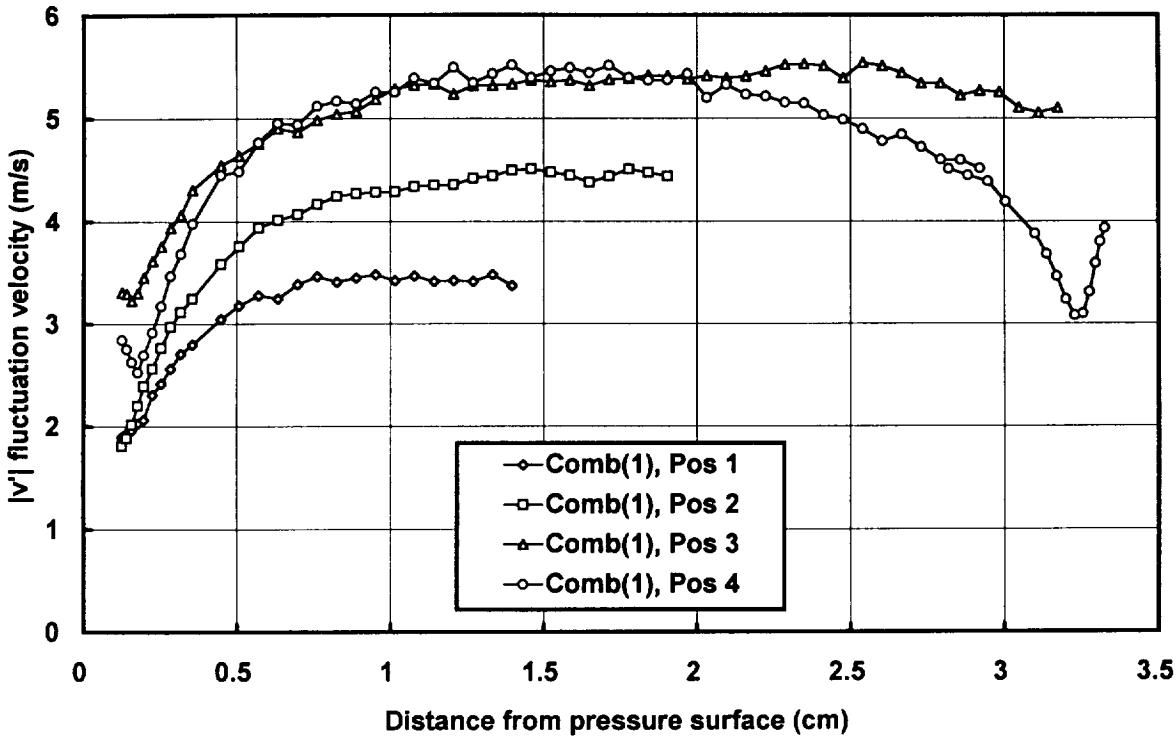

Figure 5.7 Intrapassage distribution of v' at locations 1 through 4 for Comb(1)

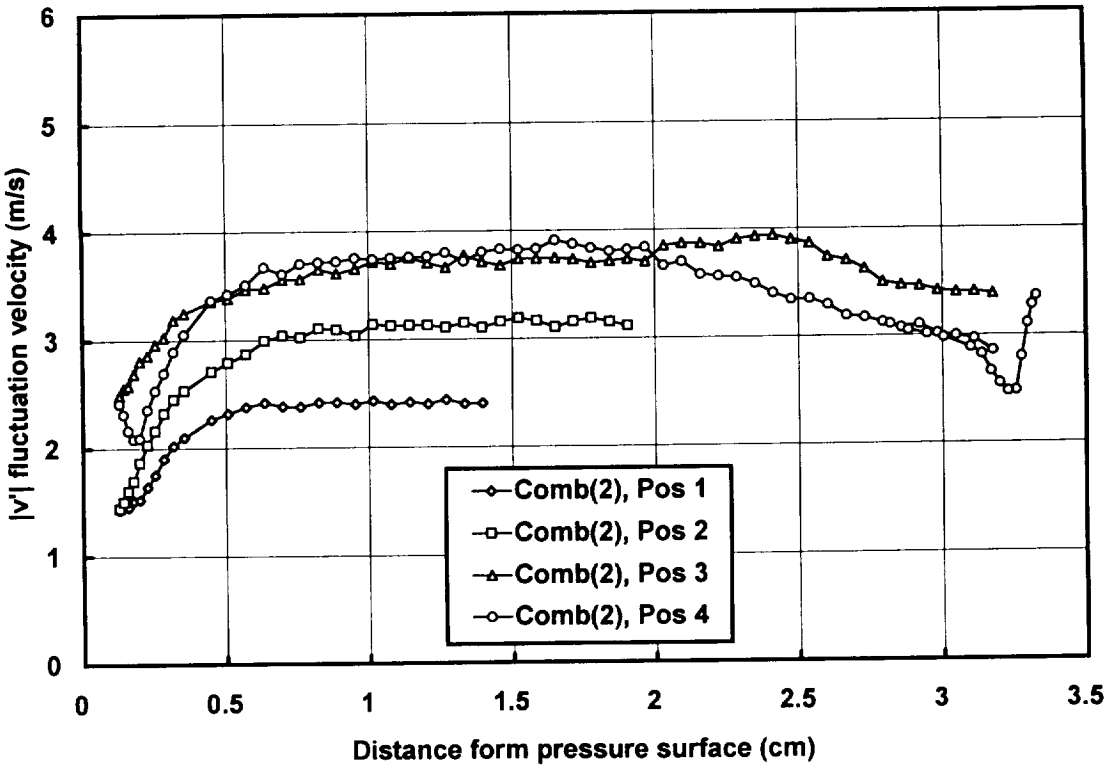

Figure 5.8 Intrapassage distribution of v' at locations 1 through 4 for Comb(2)

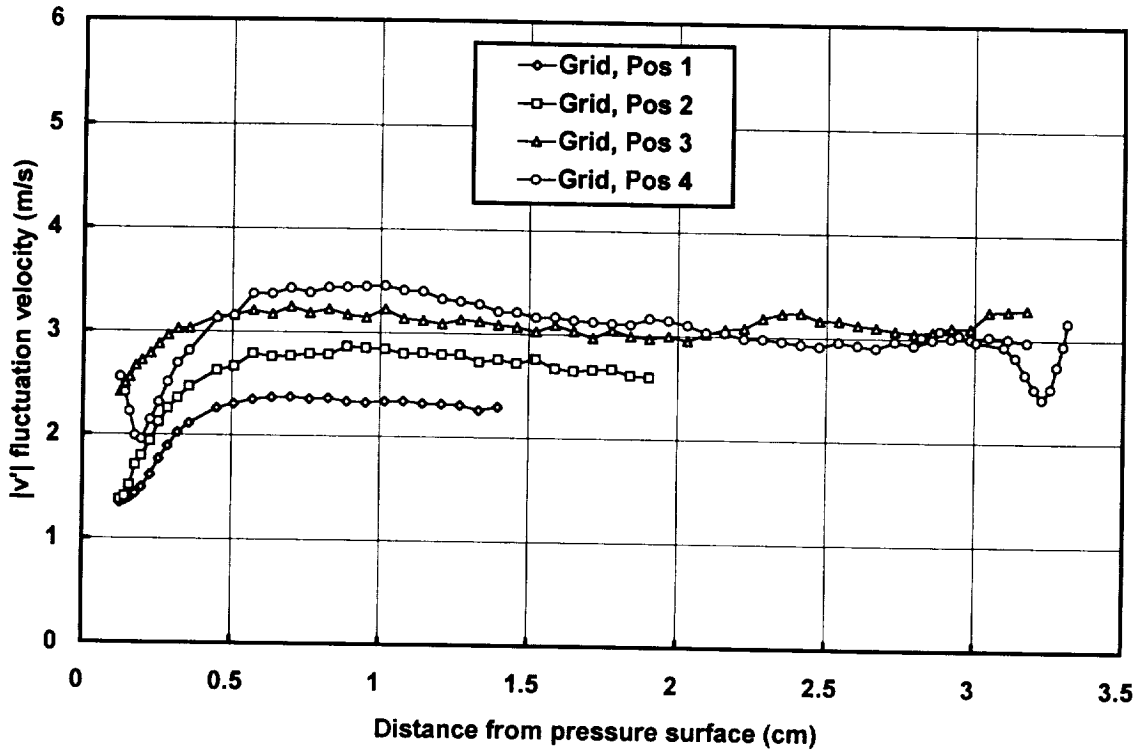

Figure 5.9 Intrapassage distribution of v' at locations 1 through 4 for Grid

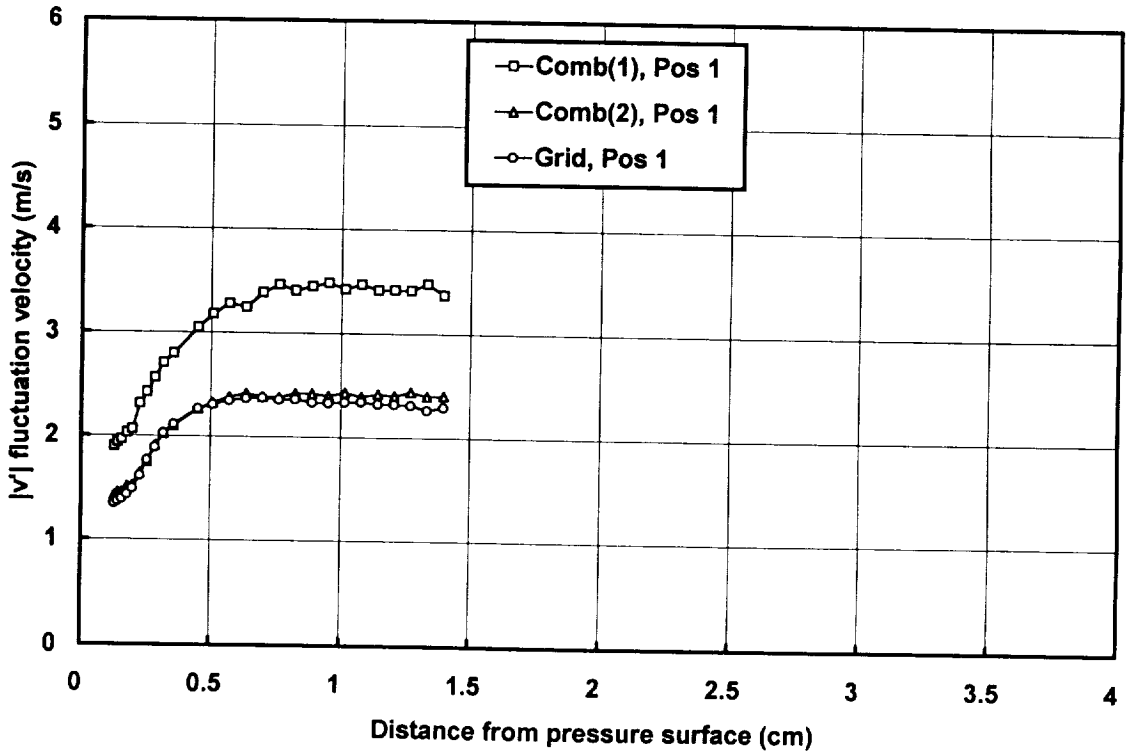

Figure 5.10 Comparison of v' distributions at location 1

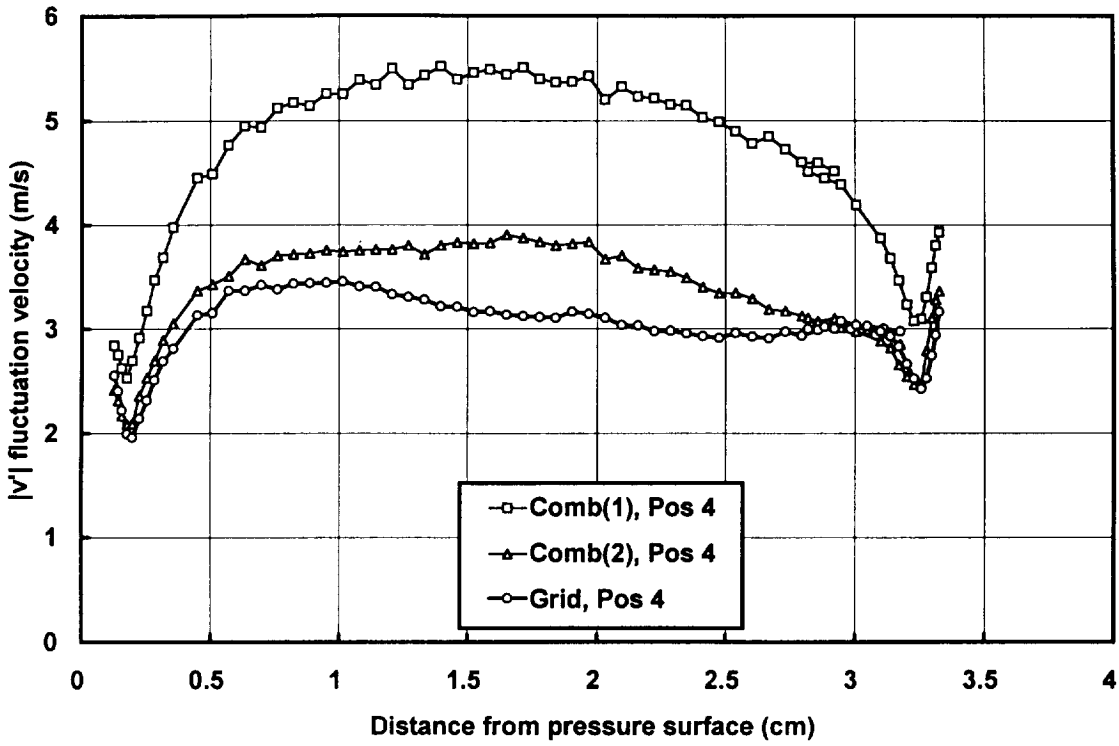

Figure 5.11 Comparison of v' distributions at location 4

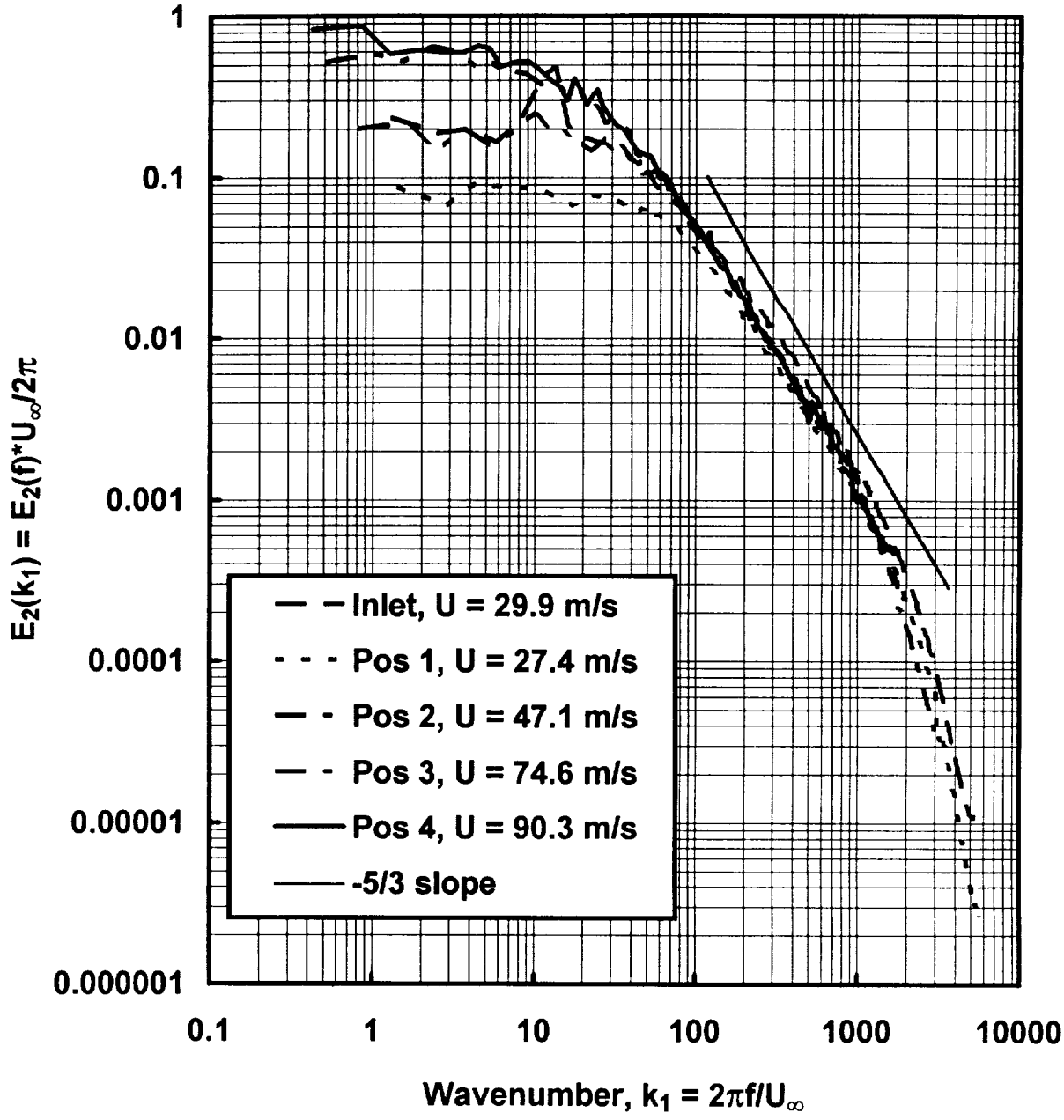

Figure 5.12 Development of v' spectra through turbine passage for Comb(1)

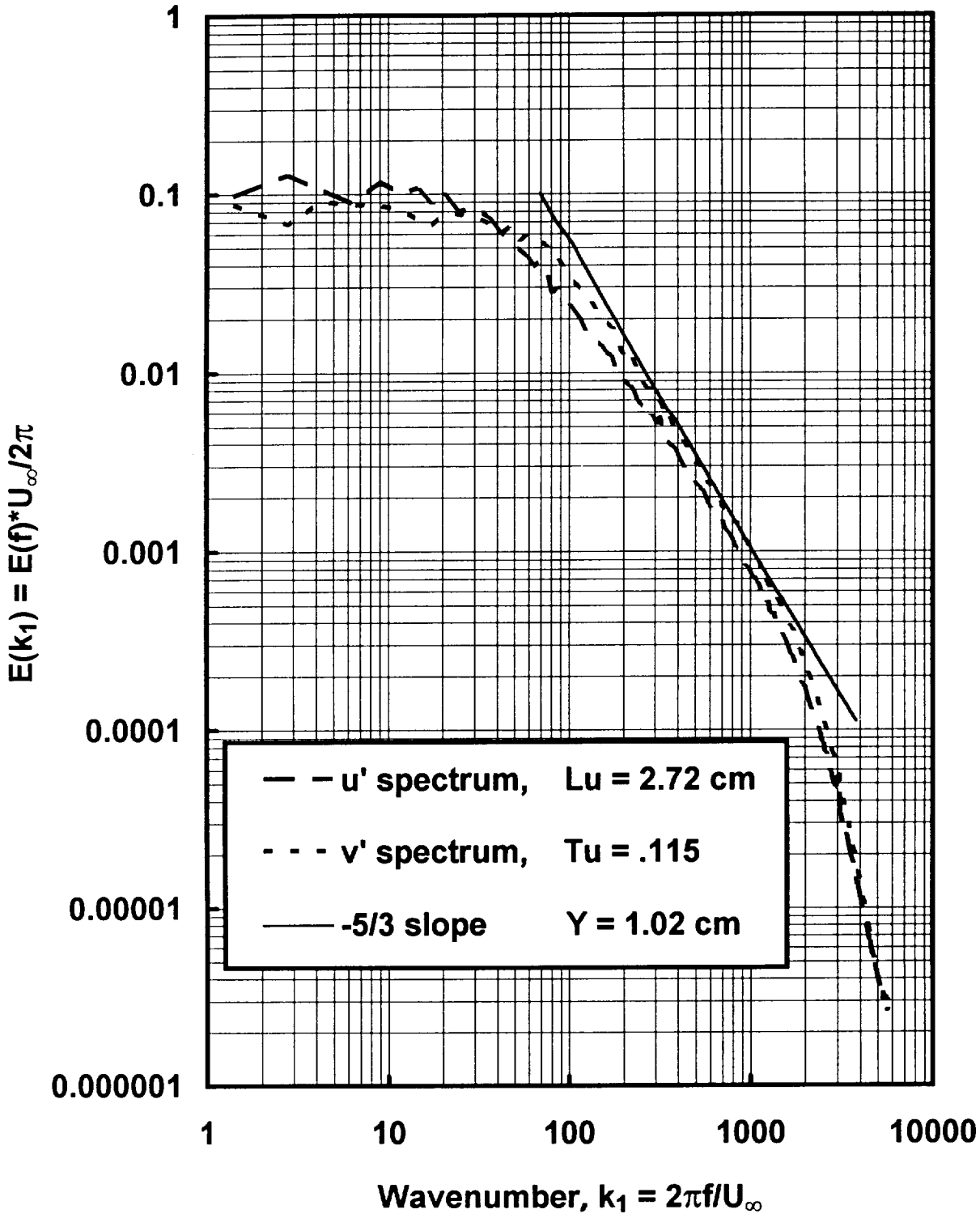

Figure 5.13 One dimensional spectra of u' and v' for Comb(1) at position 1 showing inertial subrange isotropy, U = 27.4 m/s

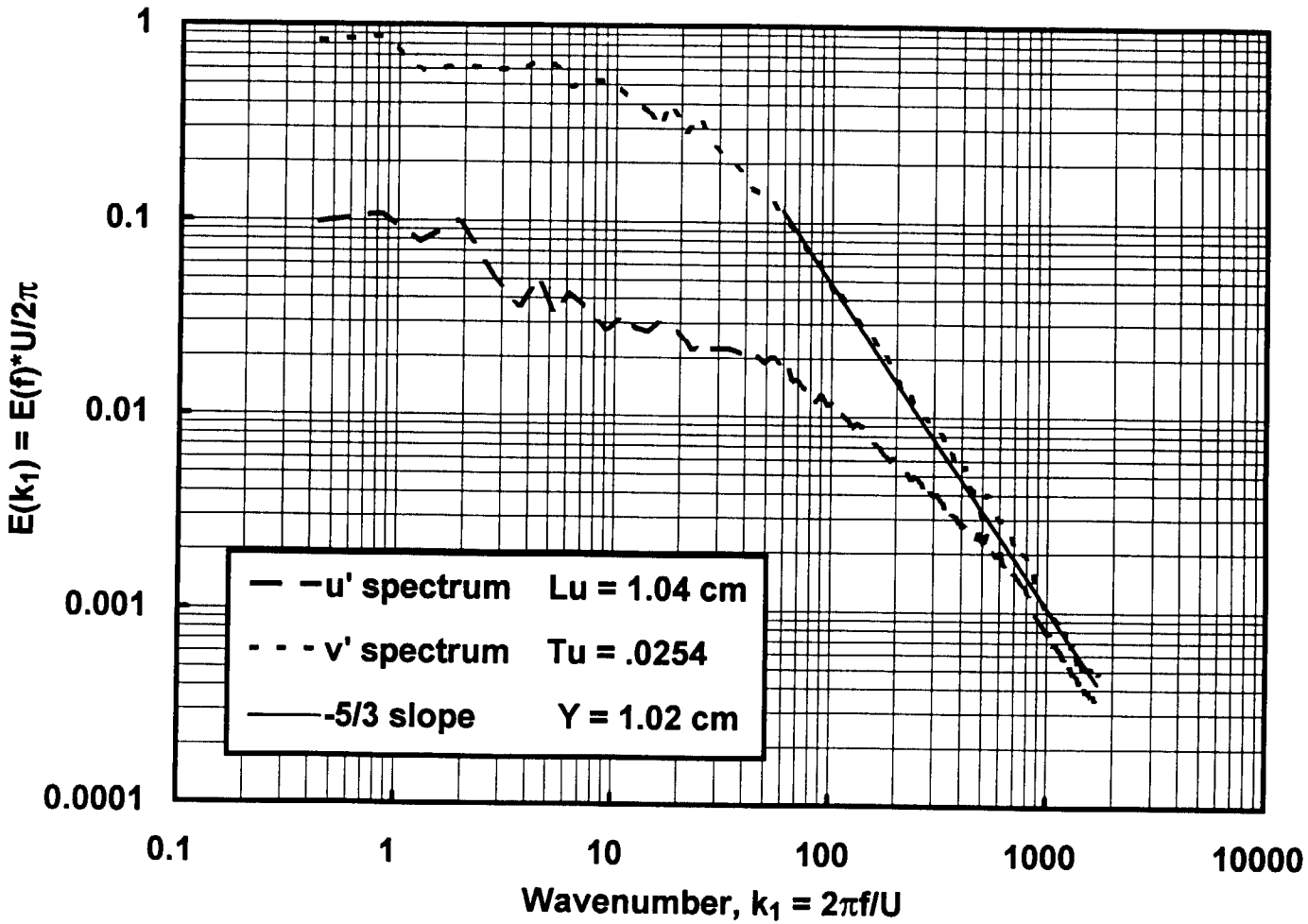

Figure 5.14 One dimensional spectra of u' and v' for Comb(1) at position 4 showing significant anisotropy, U = 90.3 m/s

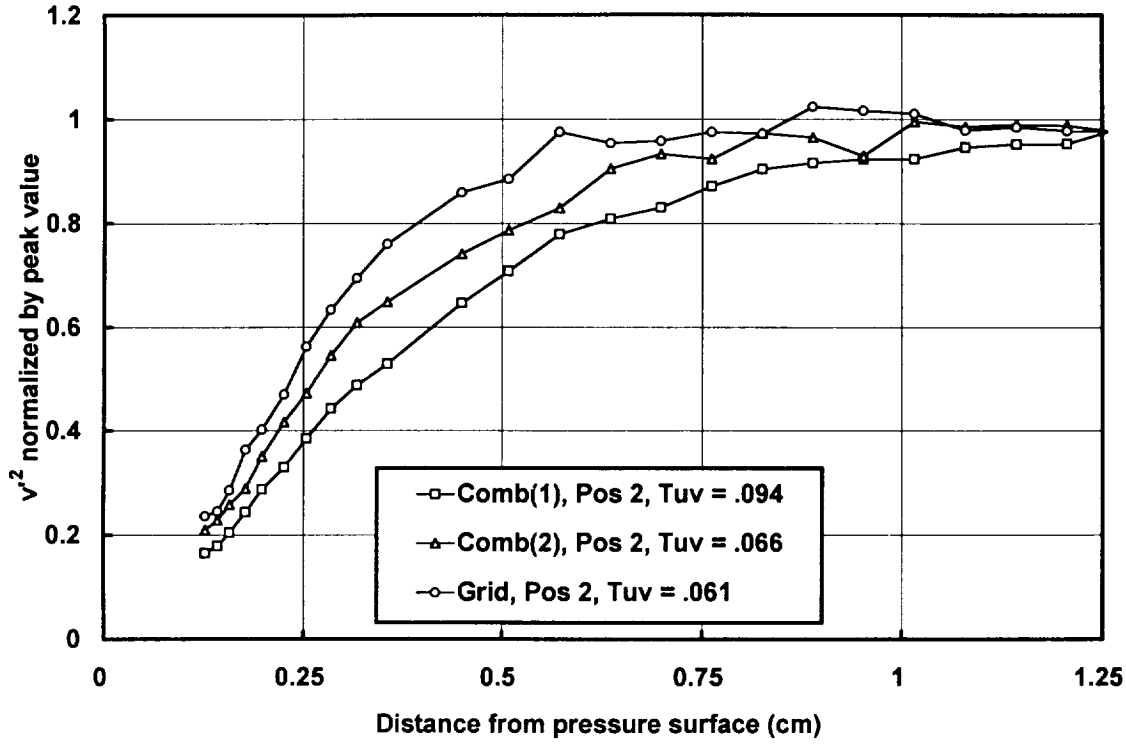

Figure 5.15 Comparison of near wall distributions of v'^2/v'^2_∞ at position 2

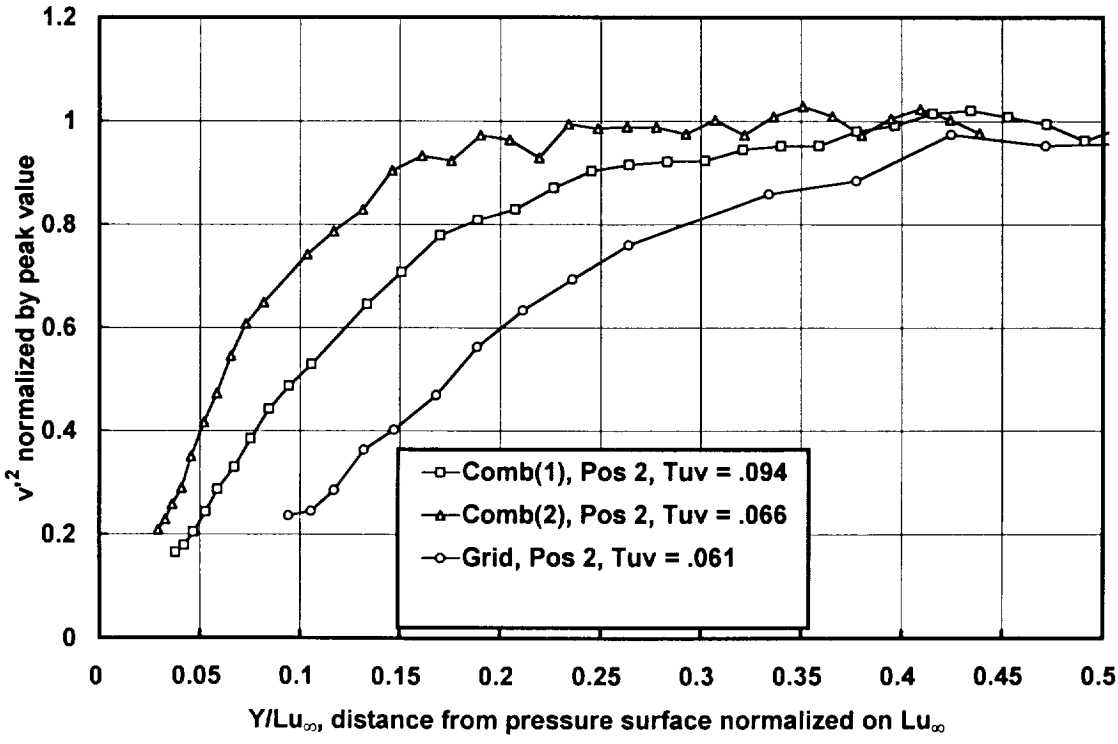

Figure 5.16 Comparison of near wall distributions of v'^2/v'^2_∞ versus Y/Lu_∞ at position 2

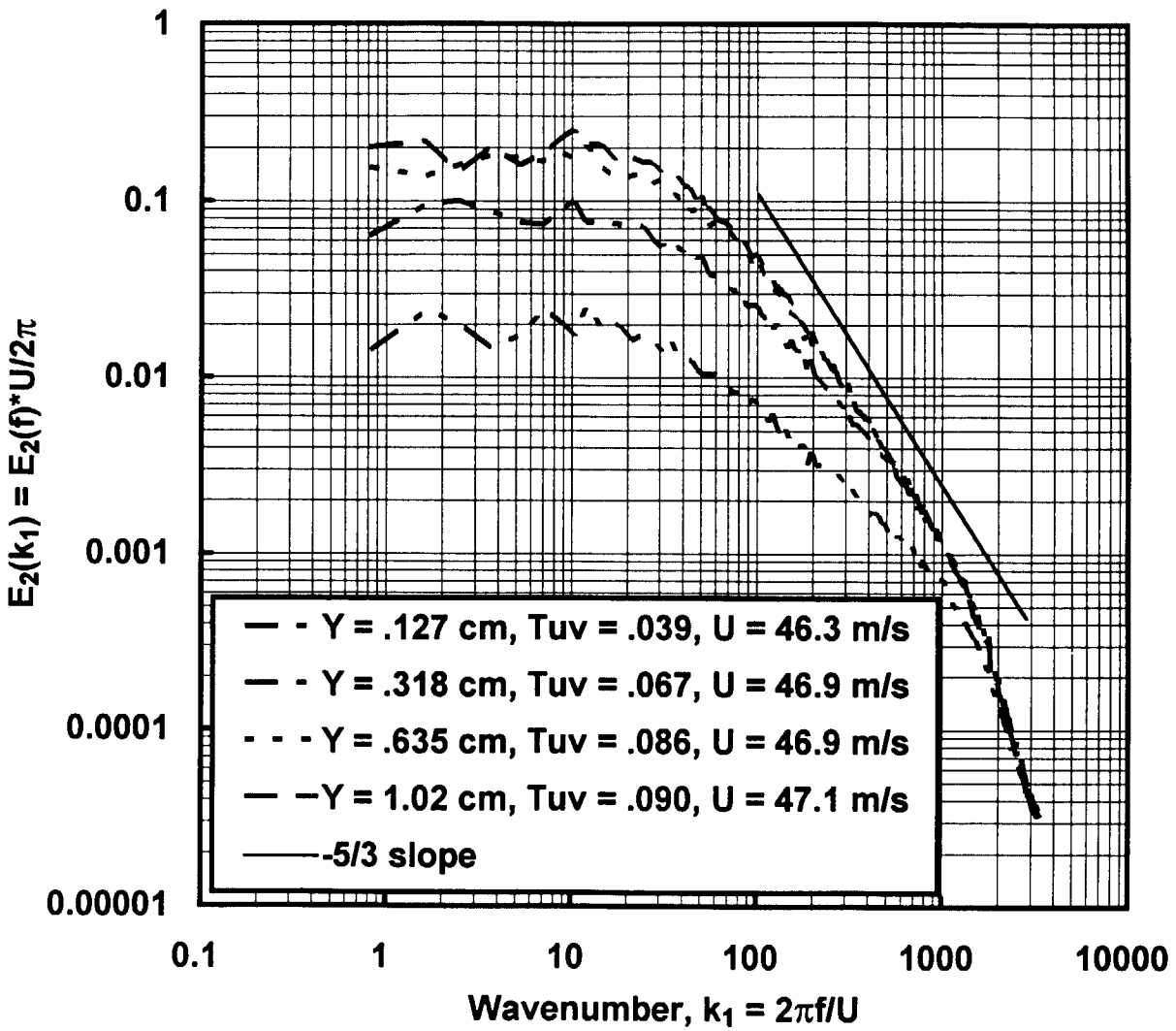

Figure 5.17 One dimensional v' spectra at various Y, position 2, Comb(1)

Chapter 6

Exit Measurements

The exit conditions of the first stage vane not only provide a means to assess vane profile loss but also constitute the inlet boundary conditions for the first stage rotor. Identifying the influence of inlet turbulence on losses and the development of the wake is important for accurately predicting stage aerodynamic performance and assessing the effect of combustor and wake generated turbulence on rotor heat transfer. In this section, the main results of the total pressure, single wire, and X-wire measurements will be presented and evaluated in terms of wake losses, development, and characteristics of interest for predicting heat transfer.

Wake Losses

Exit total pressure surveys were taken at midspan at positions 6 and 8 to determine profile losses for the different turbulence conditions. Figure 6.1 shows the total pressure loss profile from blade 2 taken at position 6 for the four turbulence conditions. The inlet turbulence conditions are listed on the legend of the figures. The survey starts from the suction surface of vane 3 and traverses across the wake of vane 2 (see figure 5.1). The peak total pressure loss is highest for the low turbulence condition and lowest for the close combustor [Comb(1)] condition. The close combustor has the broadest width while the low turbulence condition has the narrowest width. Another feature the profiles show is a loss which occurs in the core of the flow well away from either the edge of the wake or the suction surface boundary layer. This loss is clearly a strong function of the turbulence level and is at least partly due to turbulent mixing across velocity gradients in the core of the flow. This "background" loss is negligible for the low turbulence condition but is very important for the close combustor condition.

The exit total pressure loss profiles taken at position 8 for the lower wake (blade 2) are shown in figure 6.2. The trends of peaks, widths, and background losses discussed for figure 6.1 are similar here but are even more pronounced. The exit total pressure loss for both the upper (blade 3) and lower (blade 2) wakes, taken from position 8, are shown in figure 6.3. The suction surface side of the upper wake gives evidence of the effects of turbulence on the suction surface boundary layer and the resulting effect on the near wake profile. The wake edge profile is much more abrupt for the low turbulence wake as compared to the higher turbulence wakes.

Some of the more important wake parameters for positions 6 and 8, downstream of vane 2, are tabulated in table 6.1a and 6.1b including the mass averaged total

pressure loss, $\bar{\omega}$, and kinetic energy loss, $\bar{e}$, which are close in value due to the low exit Mach number of 0.27. These parameters provide information about the origin of the losses. The midspan or profile losses can be categorized into losses due to the development of boundary layers on the vane, losses due to separation at the trailing edge, and losses due to turbulence mixing outside of the vane boundary layers and wakes. The losses categorized as "background" losses seem high for the elevated turbulence level cases. However, both the level of turbulent kinetic energy and the dissipation rate increase significantly between and cascade inlet plane and the exit measurement stations, indicating that turbulent production in the core of the flow due to lateral and streamwise velocity gradients is extracting kinetic energy from the flow. At least 1/3 and perhaps 1/2 of a percent in losses can be attributed to turbulence production by a simple balance. Denton [24] (1993) indicates that mixing process across velocity gradients in the flow can be a source of losses even when no frictional forces are present. The source of the additional 1/2 to 2/3 of a percent in these "background" losses is not understood. However, this level of total pressure loss between wakes is consistent with experience at Allison Engine Company in their warm cascade facility where data on the C3X vane also shows that secondary losses are predominately confined to a region near the endwalls within 1/4 the span of the vane.

The largest source of loss is the suction surface boundary layer. The loss parameters and boundary layer parameters due to the suction surface boundary layer are listed with the subscript "ss" in the table. These parameters show that suction surface boundary layer developing on vane 3 at position 6 is responsible for 40 to 50 percent of the total wake loss. In addition, when the skin friction coefficient is integrated to the trailing edge of the blade and an estimate for the pressure surface skin friction loss is added, the resulting loss ranges from 50 to 60 percent of the total wake loss. The trailing edge blockage accounts for 30 to 40 percent of the loss and using the analysis from chapter 7 of NASA SP-290 [25] (1973) has a drag coefficient which averages 0.144 and ranges from 0.126 to 0.163. NASA SP-290 sites two references which suggest the drag coefficient for a rounded trailing edge ranges between 0.14 and 0.16. The local wake kinetic energy loss, $\bar{e}_{1,clc}$, can also be determined for the integral parameters as given by equation (7-67) of NASA SP-290. The mixed out loss, $\bar{e}_2$, can be determined from the integral parameters for incompressible flow but does require knowledge of the exit angle. The exit angle, α_2, was taken as the inverse cosine of the cross stream distance, CL, ratioed by the vane spacing, 11.773 cm. The cross stream distance, CL, was determined from the distance between the suction surface of vane 3 and the centerline of the vane 2 wake for position 6. For position 8, CL was taken as the cross stream distance between the peak deficit location of vane 2 and 3's wake. Equation (7.82) of NASA SP-290 was used to determine $\bar{e}_{2,clc}$. The half velocity widths reported in tables 6.1a and 6.1b are uncorrected for shear displacement effects. In a velocity gradient, a total pressure probe tends to read a pressure which is skewed towards the high velocity side since the probe averages the square of the velocity. According to Moffat [26] (1980), the shift of the effective centerline towards the high

velocity side is about 0.15 times the outer diameter. The outer diameter of the pressure probe used was about 0.079 cm so the correction for this case should be about 0.0118 cm. To apply this correction to the loss coefficients, $\bar{e}_{1,clc + prb}$ and $\bar{e}_{2,clc + prb}$, the coefficients were multiplied by one plus two times the ratio of the shear displacement thickness to the half velocity width, W. At both positions 6 and 8, a comparison of the total losses shows that the low turbulence case, the grid condition, and the far combustor case [Comb(2)] are all fairly consistent. The grid and far combustor have a reduced suction surface boundary layer loss but have an increased "background" loss. The close combustor case [Comb(1)] has an elevated loss primarily due to the "background" loss. Finally, to compare the mixed out losses which can clearly be attributed only to the vane boundary layers and the trailing edge loss, the "background" loss was subtracted from the mixed out kinetic energy loss coefficient $\bar{e}_{2,clc + prb - bgd}$. At position 6, a comparison shows the net wake losses are fairly consistent. A noticeable increase in losses occurs between positions 6 and 8. Part of this increase could be due to the divergence that takes place between the two stations. According to Denton (1993), deceleration amplifies velocity gradients and can increase the mixing loss in wakes. Also, some of the increase in loss between the two stations could be due to slight differences in the upstream and downstream setup, the uncertainty in experimentally determining the loss coefficient, and the mixing out of spanwise nonuniformities in the flow. For the close combustor case, at least part of this increase in "background" losses appears to be due to mixing together of the adjacent wakes.

Wake Growth Estimates

Single wire velocity profiles exhibit the same trends as the total pressure profiles. Figure 6.4 shows the mean velocity deficit profiles for the wakes at position 6. Again the low turbulence wake has a deeper velocity deficit and a narrower profile while the high turbulence wakes are shallower and broader. Figure 6.5 shows the velocity defect profiles taken from position 8 for the upper and lower wakes with similar trends to figure 6.4. An analysis of the wake growth is given in table 6.2. This analysis for cylinder wakes from Hinze (1975) is considered valid for 50 or more diameters downstream from a cylinder. While the present data are neither from a cylinder nor outside of 50 trailing edge diameters, the analysis does provide a means to compare the relative growth of the wakes between station 6 and 8 behind vane 2.

Based on the single wire probe length, the wire intersected the wake 6.965 cm and 13.388 cm downstream from the trailing edge of the vane. In the table, the half velocity width of the wake is based on the locations where 1/2 the peak defect velocity occurs on each side of the wake. Also, the ratio of the maximum defect velocity divided by the free stream velocity is given. Based on the analysis of Hinze, the following equation can be used to estimate the origin, a, of the wake.

$$a = W^2/.1817/d - X_1 \qquad (6.1)$$

where d is the trailing edge diameter, (0.34 cm) and X_1 is the downstream distance from the trailing edge to the probe. The key feature of growth is shown by comparing the origin of the wakes between positions 6 and 8. All the wakes with elevated levels of free stream turbulence show a substantial increase in the distance to the origin as compared to the low free stream turbulence wake. This comparison supports the contention that the free stream turbulence enhances spreading of the wakes and therefore the mixing within the wakes.

Turbulence Parameters

The characteristics of the turbulence at the exit of the cascade help describe the wake in terms of pertinent mixing parameters and also document the turbulence boundary condition for the rotor. Figure 6.6 shows the u' distribution taken at position 6. The profiles show turbulence in the suction surface boundary layer through the passage and across the wake. The wakes show the characteristic double peak behavior due to the maximum velocity gradients being located on either side of the peak with their resulting high production rates.

The v' distributions for position 6 are shown in figure 6.7. Near the suction surface of the upper vane, the v' distributions show a near wall increase due to boundary layer production. Outside the boundary layer but near the wall, the attenuation of v' due to the wall is evident in the profile. The energy in the v' component is redirected into the u' and w' components. In the wake off the suction surface of vane 3, evidence of the history of v' attenuation is evident. The v' distributions are also off centerline toward the pressure surface. The pressure side of the wake has a higher initial velocity gradient than the suction surface due its the boundary layer profile and this gradient produces high production rates.

The u' fluctuating velocity distributions taken at position 8 with an X-wire are shown in figure 6.8. These u' distributions agree very well with the single wire u' distributions. Comparison of the level of u' in the region between the two wakes in figure 6.8 with the u' level at position 6 (see figure 6.6) shows that u' is increasing in the streamwise direction. This increase in u' is due to the redistribution of the turbulence components after the straining of the turbulence through the turbine passage produced a significant anisotropy. The turbulence fluctuations themselves redistribute the high levels of energy in the v' and w' components into the u' component after the end of streamwise straining. The u' distributions though the wakes show the characteristic double peak behavior for both upper and lower wakes. The u' level in the wake is skewed toward the suction surface side for the high free stream turbulence cases. This skewed u' distribution is due to turbulence history effects left over from the suction surface boundary layer. The dissipation levels around the suction surface

side peaks are lower than the pressure side peaks but are about the same level for all four cases.

The v' fluctuation distributions for position 8 are shown in figure 6.9. The notable feature is that the level of v' in the core flow is now the same as the level in the lower wake for the close combustor. Also, if we estimate the turbulent kinetic energy, TKE, at position 8 based on half the total of the u' TKE and twice the v' TKE we find that the exit TKE is actually slightly above the inlet TKE.

In addition to u' and v' distributions shown in figures 6.6 through 6.9, table 6.3 provides integral length scale, energy scale, and dissipation information at different locations in both the core flow and the wake. From a standpoint of heat transfer augmentation, the cube root of dissipation seems to be the driving parameter. Evidence for this scaling is given by Ames (1994). Based on scaling laws, u' and v' should decay as $[(X_1+a)/d]^{-1/2}$ while the wake width grows as $[(X_1+a)/d]^{1/2}$. Since dissipation scales on u'^3/Lu, (Note, $Lu \equiv 1.5\ u'^3/\varepsilon$) dissipation should decay as $[(X_1+a)/d]^{-2}$ in the wake. The wake grows as $X_1^{1/2}$, so a larger area across the passage will be affected by this elevated turbulence. The resulting effect to rotor heat transfer ($\varepsilon^{1/3}W$) should scale as $[(X_1+a)/d]^{-1/6}$. Based on the present data, dissipation was found to decay as $X_1^{-3/2}$ and thus, the net affect of the wake turbulence on heat transfer augmentation should not vary significantly in the streamwise direction. Also, the total effect of the close combustor turbulence and wake turbulence together should have more than double the augmenting effect of the wake turbulence for the low free stream turbulence case.

Wake Mixing

Vane wakes provide the hydrodynamic and thermodynamic boundary condition for the downstream rotor. Accurately modeling the mixing in wakes is important to be able to predict their development. This section examines the mixing occurring in the wakes for the four turbulence conditions based on the experimental measurements.

Table 6.2 previously documented the rapid growth of the wakes with elevated levels of free stream turbulence. Enhanced mixing was inferred from this data. Figure 6.10 shows shear stress distributions taken at position 6 across the wake. Generally, the high turbulence cases show deeper and broader shear stress profiles. Similar trends are shown in figure 6.11 for both the upper and lower wakes taken at position 8.

A mean eddy diffusivity can be estimated from the shear stress measurements and the local velocity gradients. Table 6.4 lists estimates for the eddy diffusivity average across the wake in regions of high velocity gradient for the four conditions at the three measurement positions. In addition, a mean local shear stress gradient, a mixing length based on ν_m/v' (l), the half velocity width (W), the mean energy scale

(Lu), and the maximum velocity deficit in the wake are given in the table. The estimates show a substantial increase in eddy diffusivity for the flow with a turbulent core. In addition, the eddy diffusivity grows substantially in the streamwise direction for the turbulent flows. Hinze, based on cylinder analysis, suggests the eddy viscosity in a cylinder wake can be estimated as:

$$\nu_m = 0.0164\ U_\infty\ d \qquad (6.2)$$

Schlichting (1979) on the other hand estimates the value to be:

$$\nu_m = 0.0222\ C_D U_\infty\ d \qquad (6.33)$$

Since C_D for a subcritical cylinder ranges around 1.0, Schlichting's estimate for eddy viscosity is about 35 percent higher than Hinze's. Schlichting also gives the following estimate for eddy viscosity based on the free stream velocity and the half velocity width of the wake:

$$\nu_m = 0.047\ W\ U_{max,defect} \qquad (6.4)$$

This estimate for eddy viscosity is finally applicable to a vane wake. We would expect Hinze's estimate to have a coefficient of about 0.035 rather than 0.047. Based on these two estimates and the values of W and $U_{max,defect}$ given in table 6.4, the mean value of eddy viscosity in the present low turbulence wakes should range from 0.0030 m^2/s to 0.0039 m^2/s. The values in table 6.4 generally agree with this estimate.

For wakes developing in the presence of elevated levels of inlet turbulence, the mixing in the wake can be expected to be affected by the flow field turbulence as the turbulence is entrained into the wake. Excluding the suction surface side, where the turbulence affects the development of the boundary layer, the effect of the free stream turbulence is not immediate. The eddy diffusivity levels grow in the streamwise direction. This delay in the effect of the free stream turbulence is due to the wall blocking effect on v'. This effect limits the v' level close to the developing wake until the larger scale motions have time to mix into the wake region. In comparing the mixing as the wakes develop, the combustor with spool has significantly enhanced mixing over the grid turbulence due to its larger scale. Based on table 6.4, the combustor with spool conditions shows a significant increase in eddy diffusivity over the grid turbulence. This enhanced diffusivity is also reflected by the wake width and peak velocity deficit.

The mixing length, l, defined as ν_m/v' is shown for comparison to the half velocity width and the energy scale in table 6.4 For the low turbulence case, the ratio l/W would be expected to remain constant. Especially in the far field where the characteristics of the wake have reached an equilibrium state. A comparison of l and

W immediately shows that with elevated levels of free stream turbulence, the mixing length in the wake no longer scales on the wake width. This ratio l/W also grows in the downstream direction. This growth demonstrates that as turbulence with the large scale characteristics of the free stream mix into the wake, the mixing is enhanced. Another measure of a mixing length is the energy length scale, Lu. A comparison between l and Lu shows that at position 6 the ratios are consistent. Based the K-epsilon model, the ratio l/Lu should be about 0.135. At position 6 the experimental data is reasonably consistent with this value. For the wake at position 8 behind vane 2, (X_1 = 13.15 cm) l/Lu averages 0.18 and is higher for the higher levels of turbulence.

Accurately predicting the development of wakes in the streamwise direction is dependent on our ability to model the mixing process. The comparison between the mixing length, l, and the wake width, W, indicated that a mixing length model would work adequately for a low turbulence situation but not for the cases with elevated levels of free stream turbulence. The comparison between the mixing length, l, and the energy scale, Lu, shows initially that Lu gives a decent estimate for the mixing length. However, as the larger scale turbulence in the free stream begins to mix into the wake, the dissipation scale begins to underpredict the impact of these large scale motions on the mixing process.

Conclusions

In this paper, the influence of turbulence on wake losses, wake growth, overall turbulence parameters, and on mixing were examined. Losses were broken down into losses which occurred in the free stream and losses which occurred in the wake. About 50 to 60 percent of the losses could be attributed to the vane boundary layers while 30 to 40 percent of the losses could be attributed to separation off the trailing edge of the vane. The elevated levels of free stream turbulence were found to exhibit significant losses in the "core" of the flow or the part of the flow not expected to be influenced by the wake or the suction surface boundary layer. First order estimates of turbulent production in this region indicated turbulent mixing in the core of the flow is responsible for at least 1/3 to 1/2 of these "background" losses. The origin of the remainder of these "background" losses is not understood.

The elevated free stream turbulence was also found to have a significant effect on wake growth. Generally, the wakes with elevated turbulence were found to be broader across and had smaller peak velocity deficits. The wakes with the free stream turbulence spread faster than the low turbulence case based on an estimate of the wake origins.

The overall level of turbulence and dissipation inside the wakes and in the free stream was determined and can be used as the inlet turbulence boundary condition in assessing the expected effects of free stream and wake turbulence on rotor heat transfer

augmentation. Based on the concept that heat transfer augmentation scales on dissipation to the 1/3 power ($\epsilon^{1/3}$), the combined effect of close combustor turbulence with the wake generated turbulence should have more than double the effect of the low turbulence wake alone. Thus, turbulence generated in the combustor can be expected to produce an important influence on rotor heat transfer augmentation.

Eddy diffusivities and mixing lengths were estimated using X-wire measurements of shear stress to quantify how turbulence affected mixing in the wake. The free stream turbulence was found to strongly affect eddy diffusivities. The combustor at both levels of turbulence had a bigger affect than the grid turbulence due to a larger turbulent scale. At the last measuring position, the average eddy diffusivity across the close combustor condition wake was three times the eddy diffusivity of the low turbulence wake.

Table 6.1a Exit Loss Parameters, Position 6, $Ma_{ex} = 0.27$

Condition	Low Turb.	Grid	Comb(2)	Comb(1)
$\overline{\omega}$	.0434	.0456	.0449	.0521
$\overline{e}$	.0428	.0449	.0443	.0513
δ_1 (cm)	.0893	.0883	.0851	.0987
δ_2 (cm)	.0807	.0812	.0785	.0920
δ_3 (cm)	.1538	.1559	.1510	.1777
$\Delta V_{max}/V_{id}$	.1360	.1229	.1197	.1146
W (cm)	.6217	.6714	.6972	.7637
$\overline{\omega}_{max}$	.2569	.2339	.2282	.2191
$\overline{\omega}_{bgd}$	.0002	.0028	.0020	.0100
$\overline{e}_{bgd}$	.0002	.0027	.0020	.0098
$\overline{\omega}_{ss}$	.0222	.0200	.0202	.0217
$\overline{e}_{ss}$	.0220	.0198	.0199	.0214
$\delta_{1,ss}$ (cm)	.0683	.0520	.0525	.0535
$\delta_{2,ss}$ (cm)	.0462	.0373	.0379	.0400
$\delta_{3,ss}$ (cm)	.0796	.0659	.0673	.0722
$Cf/2_{ss}$	.00143	.00175	.00174	.00181
CL (cm)	3.694	3.714	3.688	3.719
Ma_{ex}	.2689	.2698	.2701	.2704
P_t (kPa)	99.4	98.8	97.5	97.5
T_t (K)	292.2	293.1	293.1	293.1
$\overline{e}_{1,clc}$	.0427	.0448	.0441	.0512
$\overline{e}_{2,clc}$	.0443	.0462	.0454	.0523
α_2 (deg)	71.71	71.61	71.44	71.59
$\overline{e}_{1,clc + prb\ dia}$	.0443	.0465	.0457	.0528
$\overline{e}_{2,clc + prb\ dia}$	.0460	.0479	.0470	.0540
$\overline{e}_{2,clc + prb - bgrd}$	.0458	.0452	.0450	.0442

Table 6.1b Exit Loss Parameters, Position 8, Lower Wake, $Ma_{ex} = 0.27$

Condition	Low Turb.	Grid	Comb(2)	Comb(1)
$\overline{\omega}$	.0520	.0535	.0502	.0564
$\overline{e}$	.0511	.0526	.0493	.0555
δ_1 (cm)	.1075	.1086	.1009	.1114
δ_2 (cm)	.0989	.1018	.0951	.1058
δ_3 (cm)	.1899	.1973	.1849	.2065
$\Delta V_{max}/V_{id}$	.1128	.0961	.0874	.0763
W (cm)	.8956	.9554	.9703	.9965
$\overline{\omega}_{max}$	.2170	.1857	.1696	.1564
$\overline{\omega}_{bgd}$	.0031	.0077	.0058	.0151
$\overline{e}_{bgd}$	.0030	.0076	.0057	.0149
CL (cm)	4.564	4.591	4.562	4.576
Ma_{ex}	.2703	.2691	.2706	.2696
P_t (Pa)	98730	98,516	97,494	96092
T_t (K)	296.8	296.6	296.1	298.5
$\overline{e}_{1,clc}$	.0509	.0525	.0493	.0554
$\overline{e}_{2,clc}$	.0523	.0534	.0501	.0559
α_2 (deg)	70.98	70.82	70.90	70.96
$\overline{e}_{1,clc + prb}$	.0523	.0538	.0505	.0567
$\overline{e}_{2,clc + prb}$	.0538	.0548	.0513	.0573
$\overline{e}_{2,clc + all - bgrd}$	.0508	.0472	.0456	.0424

Table 6.2 Wake Growth Analysis for Single Wire Data

Distance from vane trailing edge to probe arc

Position 6	X_1 = 6.965 cm
Position 8	X_1 = 13.388 cm

Position 6 wake

Condition	W (cm)	$U_{max,def}/U_\infty$	Origin (cm)
Low Turb	0.6828	0.1266	0.573
Grid	0.6852	0.1171	0.628
Comb(2)	0.7124	0.1120	1.242
Comb(1)	0.7425	0.1059	1.950

Position 8 wake

Condition	W (cm)	$U_{max,def}/U_\infty$	Origin (cm)
Low Turb	0.9884	0.1116	2.407
Grid	1.0032	0.0959	2.884
Comb(2)	1.0372	0.0883	4.008
Comb(1)	1.1172	0.0736	6.794

Table 6.3a Turbulence Characteristics at Position 6

	File	Tu	Vel (m/s)	Lx (cm)	Lu (cm)	ε (m^2/s^3)	Y (cm)	Pos
Comb(1)	ip6c1	0.1168	76.27	1.890	1.331	79800	0.123	
	ip6c2	0.0720	87.94	2.253	1.928	19800	0.309	
	ip6c3	0.0288	92.06	1.488	0.653	4296	0.987	
	ip6c4	0.0276	91.15	1.384	0.660	3622	1.975	
	ip6c5	0.0281	90.88	1.168	0.650	3842	2.318	-3σ
	ip6c6	0.0413	89.20	1.392	0.693	10854	2.986	-1.52σ
	ip6c7	0.0703	84.59	1.201	0.780	40416	3.354	$-.707\sigma$
	ip6c8	0.0751	80.25	0.980	0.691	47547	3.673	CL
	ip6c9	0.0698	83.66	1.819	1.313	22692	3.992	$+.707\sigma$
	ip6c10	0.0406	87.89	1.704	1.151	5939	4.360	$+1.52\sigma$
	ip6c11	0.0303	88.93	1.237	0.874	3345	5.028	$+3\sigma$
Comb(2)	ip6s1	0.1093	74.58	1.623	0.917	88604	0.123	
	ip6s2	0.0634	87.77	2.230	1.593	16259	0.309	
	ip6s3	0.0181	91.38	2.731	0.772	884	0.987	
	ip6s4	0.0179	90.43	2.179	0.790	800	1.975	
	ip6s5	0.0191	90.11	2.195	0.874	881	2.350	-3σ
	ip6s6	0.0354	88.56	1.191	0.658	7010	3.003	-1.52σ
	ip6s7	0.0671	83.59	1.130	0.709	37257	3.362	$-.707\sigma$
	ip6s8	0.0709	79.35	0.932	0.650	41053	3.673	CL
	ip6s9	0.0651	83.58	1.900	1.247	19415	3.985	$+.707\sigma$
	ip6s10	0.0337	87.41	2.101	1.255	3040	4.344	$+1.52\sigma$
	ip6s11	0.0217	89.10	1.300	0.963	1130	4.996	$+3\sigma$
Grid	ip6g1	0.1052	74.86	1.422	0.823	88827	0.123	
	ip6g2	0.0585	88.59	2.167	1.293	16147	0.309	
	ip6g3	0.0165	91.80	1.872	0.296	1772	0.987	
	ip6g4	0.0173	90.92	2.154	0.384	1508	1.975	
	ip6g5	0.0177	90.86	2.052	0.423	1477	2.410	-3σ
	ip6g6	0.0348	89.02	1.179	0.582	7648	3.033	-1.52σ
	ip6g7	0.0639	84.26	0.777	0.610	38485	3.376	$-.707\sigma$
	ip6g8	0.0679	75.35	0.691	0.572	41129	3.673	CL
	ip6g9	0.0622	83.38	1.207	0.963	21712	3.971	$+.707\sigma$
	ip6g10	0.0312	88.51	1.128	0.813	3888	4.314	$+1.52\sigma$
	ip6g11	0.0162	89.67	2.466	0.404	1148	4.937	$+3\sigma$
Low Turb	ip6l1	0.0261	89.74	1.590	0.630	3099	3.009	-1.52σ
	ip6l2	0.0601	83.85	0.417	0.541	35554	3.354	$-.707\sigma$
	ip6l3	0.0623	79.62	0.335	0.478	36953	3.654	CL
	ip6l4	0.0548	83.54	0.574	0.777	18569	3.954	$+.707\sigma$
	ip6l5	0.0227	89.06	1.483	0.897	1388	4.299	$+1.52\sigma$

Table 6.3b Turbulence Characteristics at Position 8

	File	Tu	Vel (m/s)	Lx (cm)	Lu (cm)	ε (m^2s^3)	Y (cm)	Pos
Comb(1)	ip8c1	0.0984	79.70	0.665	0.424	164088	0.501	$-.707\sigma$
	ip8c2	0.1127	72.77	1.151	0.518	160194	0.706	CL
	ip8c3	0.1073	79.91	2.144	1.732	54680	0.911	$+.707\sigma$
	ip8c4	0.0366	88.76	1.908	1.176	4387	1.575	$+3\sigma$
	ip8c5	0.0314	89.14	1.140	0.813	4060	2.098	
	ip8c6	0.0308	89.27	0.937	0.754	4113	2.528	-3σ
	ip8c7	0.0402	88.28	1.669	0.983	6820	3.550	-1.52σ
	ip8c8	0.0578	84.69	1.775	1.232	14275	4.110	$-.707\sigma$
	ip8c9	0.0589	82.28	1.702	1.110	15380	4.596	CL
	ip8c10	0.0536	85.46	2.306	1.588	9090	5.085	$+.707\sigma$
	ip8c11	0.0370	88.30	1.836	1.285	4063	5.645	$+1.52\sigma$
	ip8c12	0.0343	88.73	1.572	1.295	3264	6.667	$+3\sigma$
Comb(2)	ip8s1	0.0977	75.94	0.500	0.330	185780	0.506	$-.707\sigma$
	ip8s2	0.1069	71.29	1.120	0.424	156889	0.691	CL
	ip8s3	0.1044	78.38	1.737	1.361	60424	0.876	$+.707\sigma$
	ip8s4	0.0233	88.66	1.748	0.792	1661	1.476	$+3\sigma$
	ip8s5	0.0183	88.67	2.223	0.503	1266	2.098	
	ip8s6	0.0215	88.63	2.121	0.795	1298	2.621	-3σ
	ip8s7	0.0314	87.97	2.002	0.798	3970	3.552	-1.52σ
	ip8s8	0.0538	84.11	1.842	1.105	12601	4.063	$-.707\sigma$
	ip8s9	0.0553	80.81	1.400	0.848	15744	4.507	CL
	ip8s10	0.0528	84.24	2.289	1.420	9300	4.939	$+.707\sigma$
	ip8s11	0.0307	87.93	1.636	1.143	2488	5.465	$+1.52\sigma$
	ip8s12	0.0230	88.43	1.562	0.953	1326	6.396	$+3\sigma$
Grid	ip8g1	0.0958	76.34	0.297	0.345	169650	0.521	$-.707\sigma$
	ip8g2	0.1054	72.47	1.115	0.597	112071	0.701	CL
	ip8g3	0.0972	79.56	1.468	1.219	56905	0.880	$+.707\sigma$
	ip8g4	0.0205	88.80	2.240	0.488	1840	1.464	$+3\sigma$
	ip8g5	0.0200	88.99	1.882	0.531	1602	2.098	
	ip8g6	0.0188	88.90	1.923	0.442	1592	2.651	-3σ
	ip8g7	0.0291	88.24	1.735	0.653	3890	3.573	-1.52σ
	ip8g8	0.0499	83.98	1.539	0.907	12160	4.079	$-.707\sigma$
	ip8g9	0.0504	80.44	0.810	0.688	14455	4.519	CL
	ip8g10	0.0467	84.06	1.026	1.049	8656	4.960	$+.707\sigma$
	ip8g11	0.0226	88.16	1.052	0.589	2002	5.466	$+1.52\sigma$
	ip8g12	0.0143	76.42	1.476	0.328	942	6.388	$+3\sigma$
Low Turb	ip8l1	0.0957	75.69	0.135	0.300	190950	0.533	$-.707\sigma$
	ip8l2	0.0924	66.64	0.140	0.249	141051	0.701	CL
	ip8l3	0.0806	75.33	0.201	0.523	63942	0.869	$+.707\sigma$
	ip8l4	0.0197	88.62	1.869	0.475	1690	3.589	-1.52σ
	ip8l5	0.0464	83.33	0.579	0.716	12135	4.080	$-.707\sigma$
	ip8l6	0.0485	79.42	0.579	0.648	13195	4.507	CL
	ip8l7	0.0445	83.59	0.787	0.958	8072	4.932	$+.707\sigma$
	ip8l8	0.0191	88.94	2.365	0.871	850	5.423	$+1.52\sigma$

Table 6.4 Wake Mixing and Turbulence Parameters

Position 6

Condition	|dU/dy| (1/s)	ν_m (m^2/s)	l (cm)	Width (cm)	Lu (cm)	$U_{max,defect}$ (m/s)
Comb(1)	1753	0.00694	0.124	0.7382	0.851	10.56
Comb(2)	1930	0.00556	0.104	0.7012	0.790	11.24
Grid	1981	0.00475	0.094	0.7006	0.635	11.52
Low Turb	2278	0.00410	0.079	0.6664	0.566	12.40

Position 8

Condition	|dU/dy| (1/s)	ν_m (m^2/s)	l (cm)	Width (cm)	Lu (cm)	$U_{max,defect}$ (m/s)
Comb(1)	758	0.01060	0.257	1.0471	1.262	6.84
Comb(2)	978	0.00701	0.185	0.9866	1.074	8.23
Grid	1019	0.00572	0.162	0.9599	0.851	8.49
Low Turb	1189	0.00344	0.109	0.9387	0.747	10.68

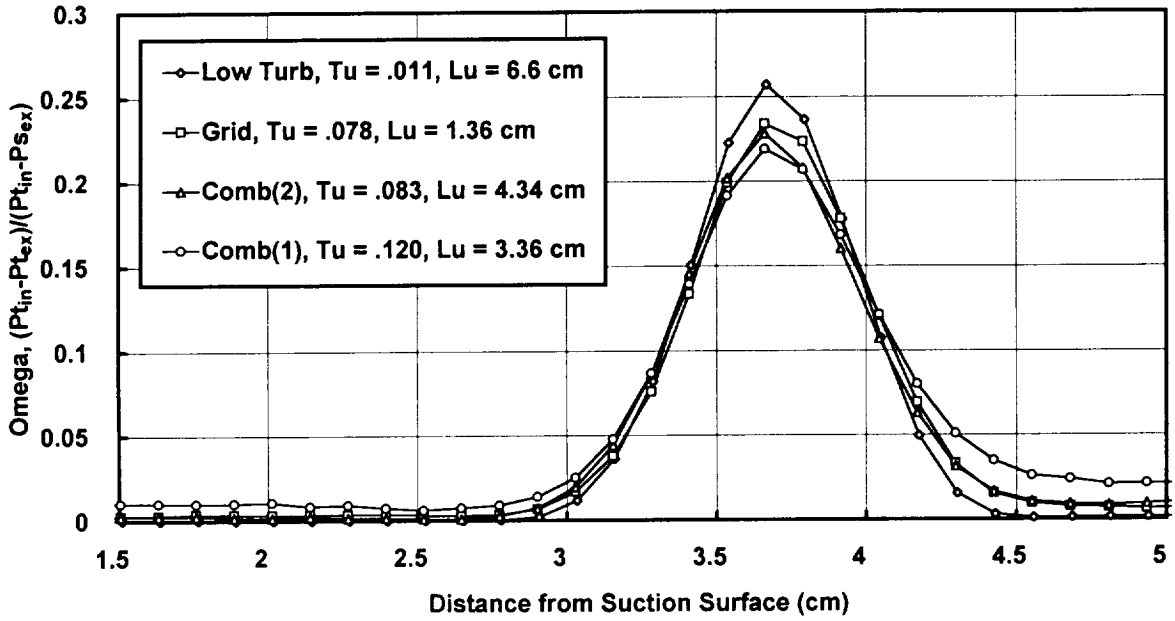

Figure 6.1 Comparison of exit total pressure loss surveys, position 6, $Ma_{ex} = 0.27$

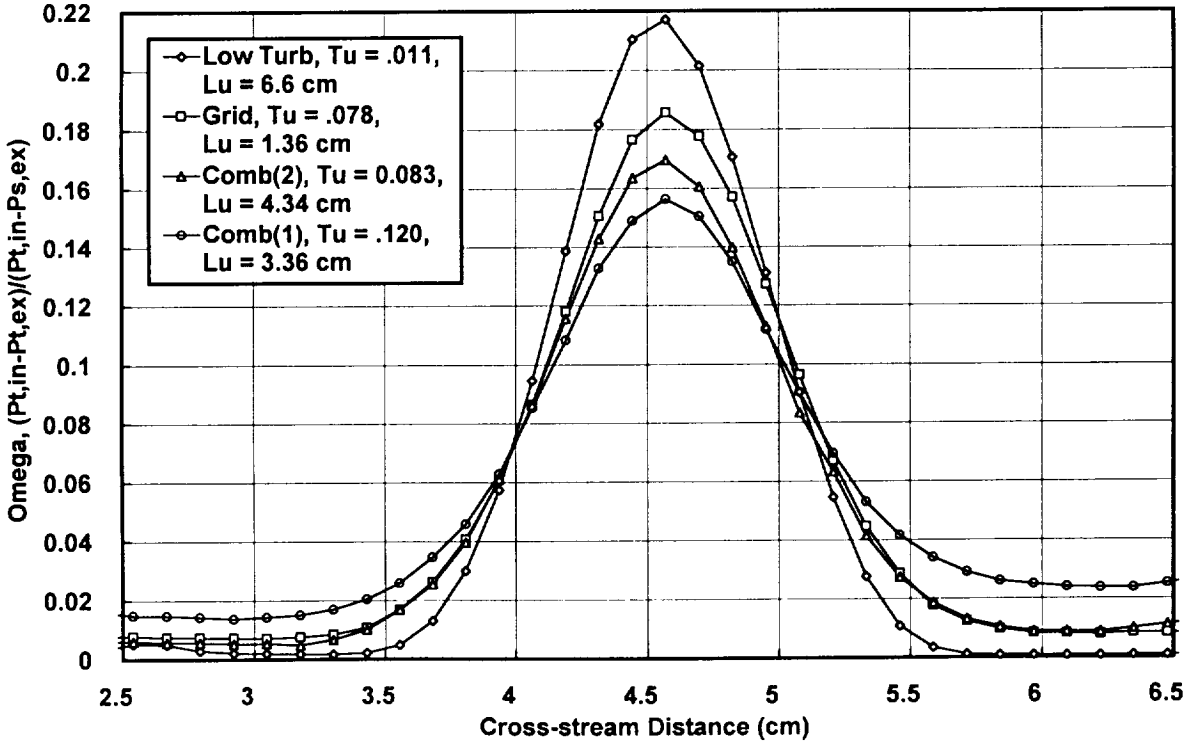

Figure 6.2 Comparison of exit total pressure loss surveys, position 8, lower wake, $Ma_{ex} = 0.27$

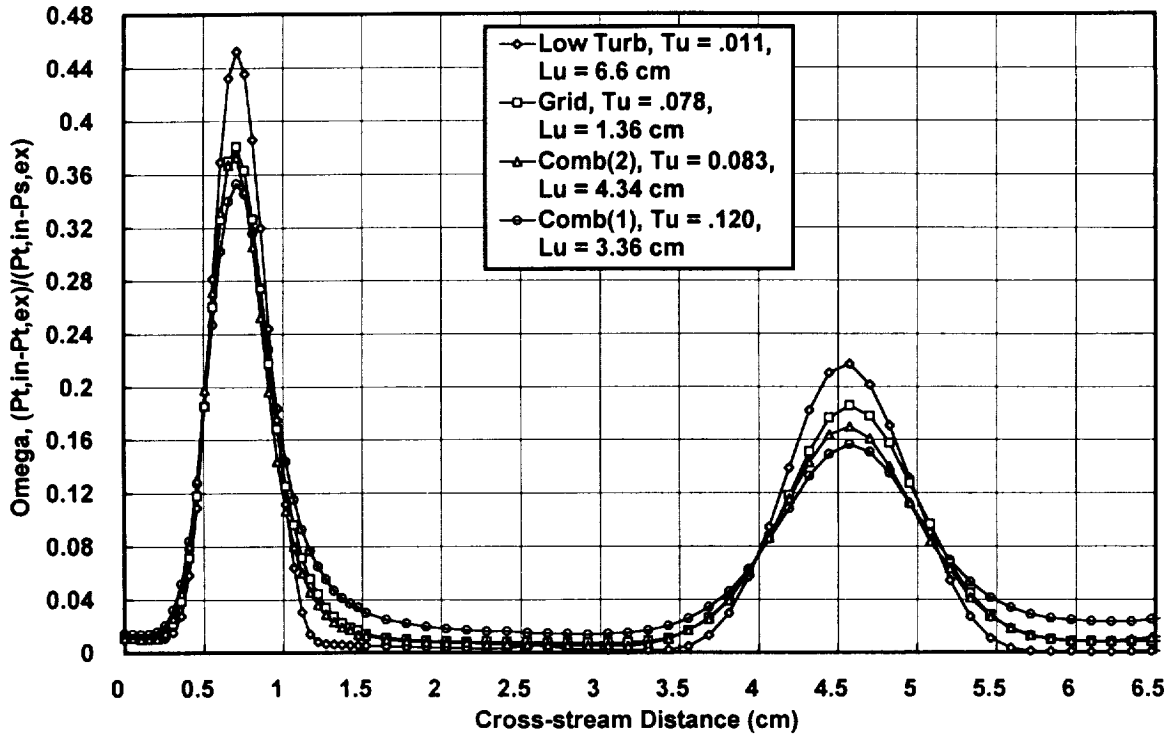

Figure 6.3 Comparison of exit total pressure loss surveys, position 8, upper and lower wakes, $Ma_{ex} = 0.27$

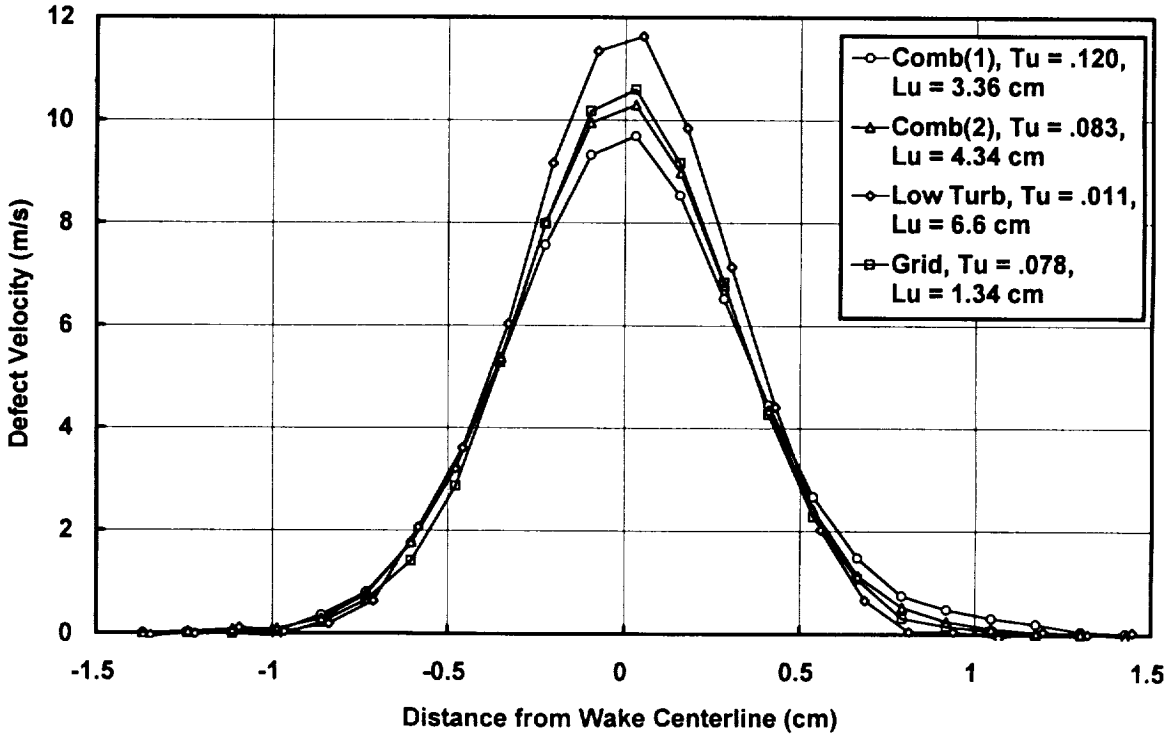

Figure 6.4 Comparison of single wire wake profiles, position 6, $Ma_{ex} = 0.27$

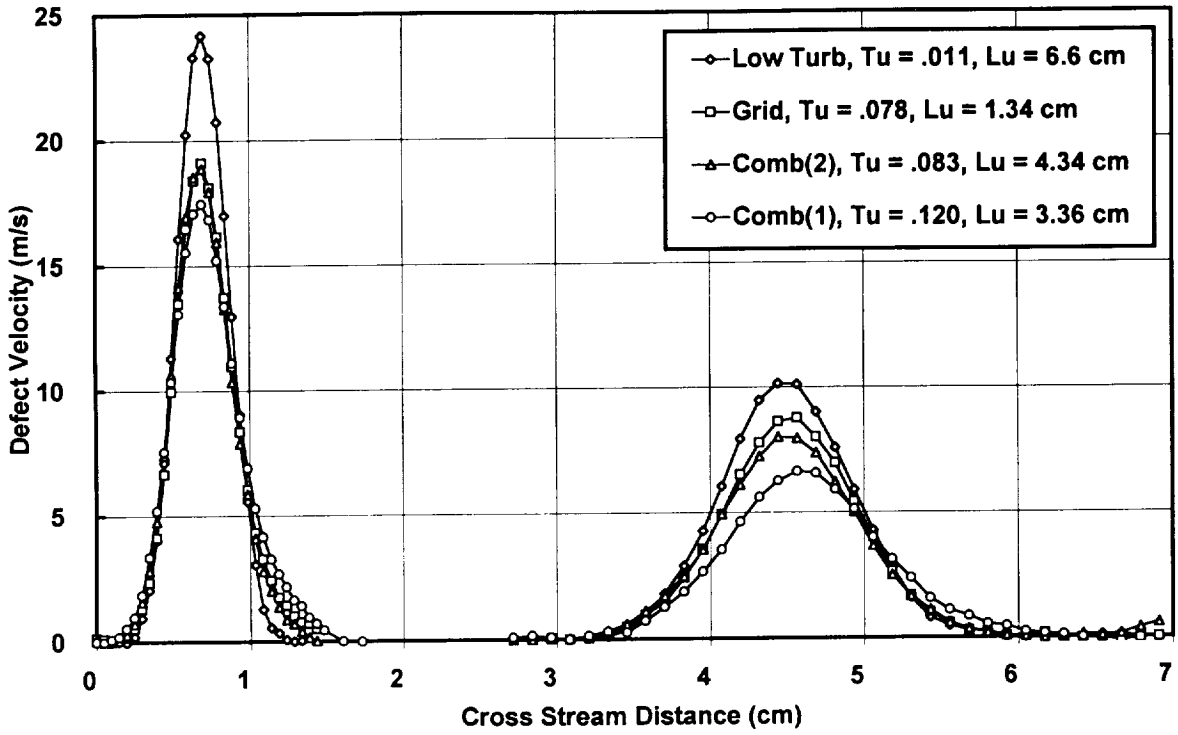

Figure 6.5 Comparison of single wire wake profiles, position 8, $Ma_{ex} = 0.27$

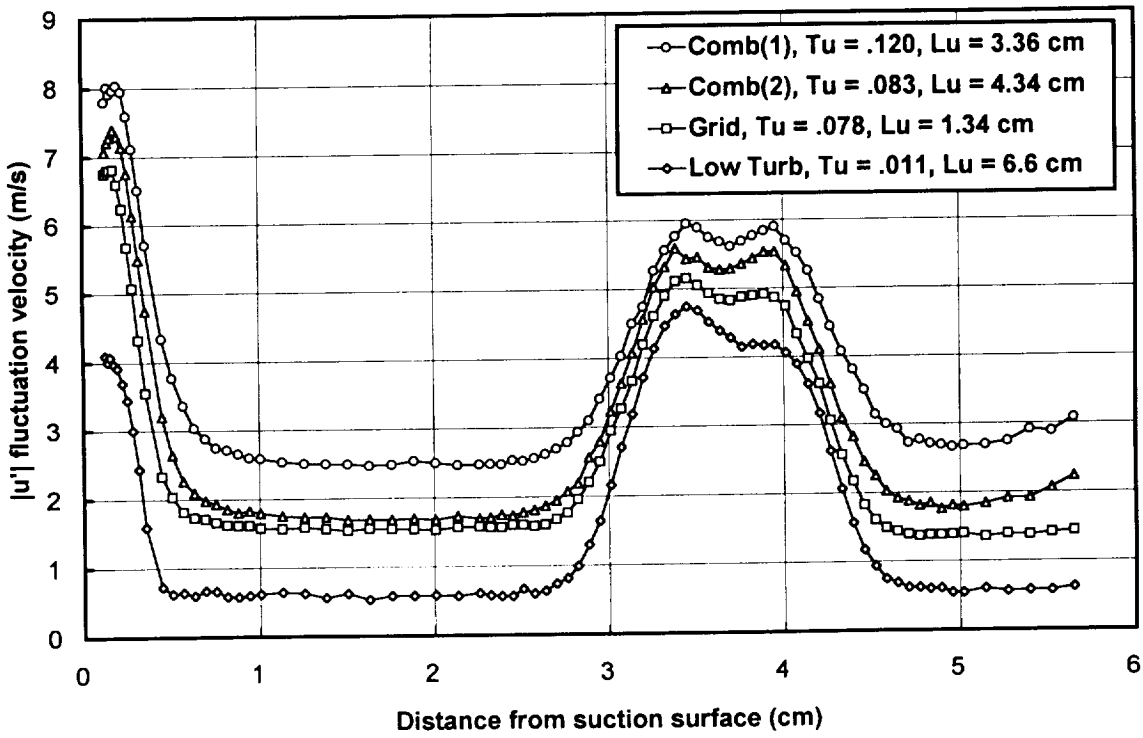

Figure 6.6 Comparison of X wire |u'| distributions, position 6, $Ma_{ex} = 0.27$

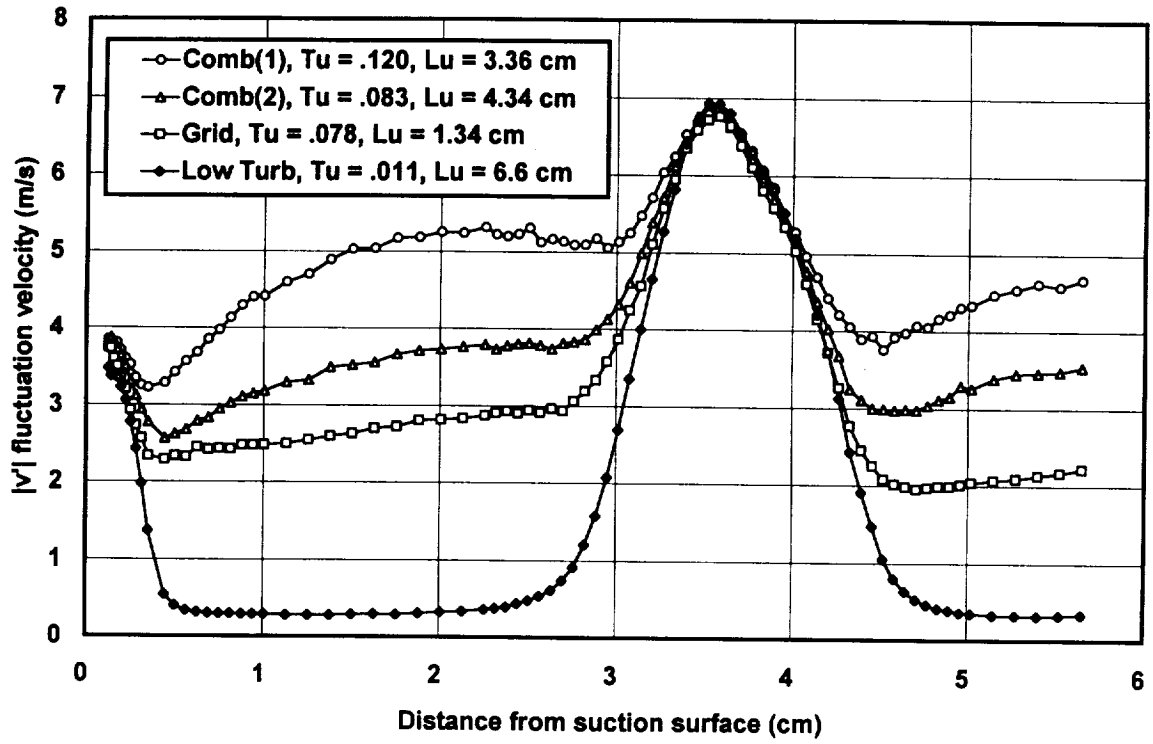

Figure 6.7 Comparison of v' distributions, position 6, $Ma_{ex} = 0.27$

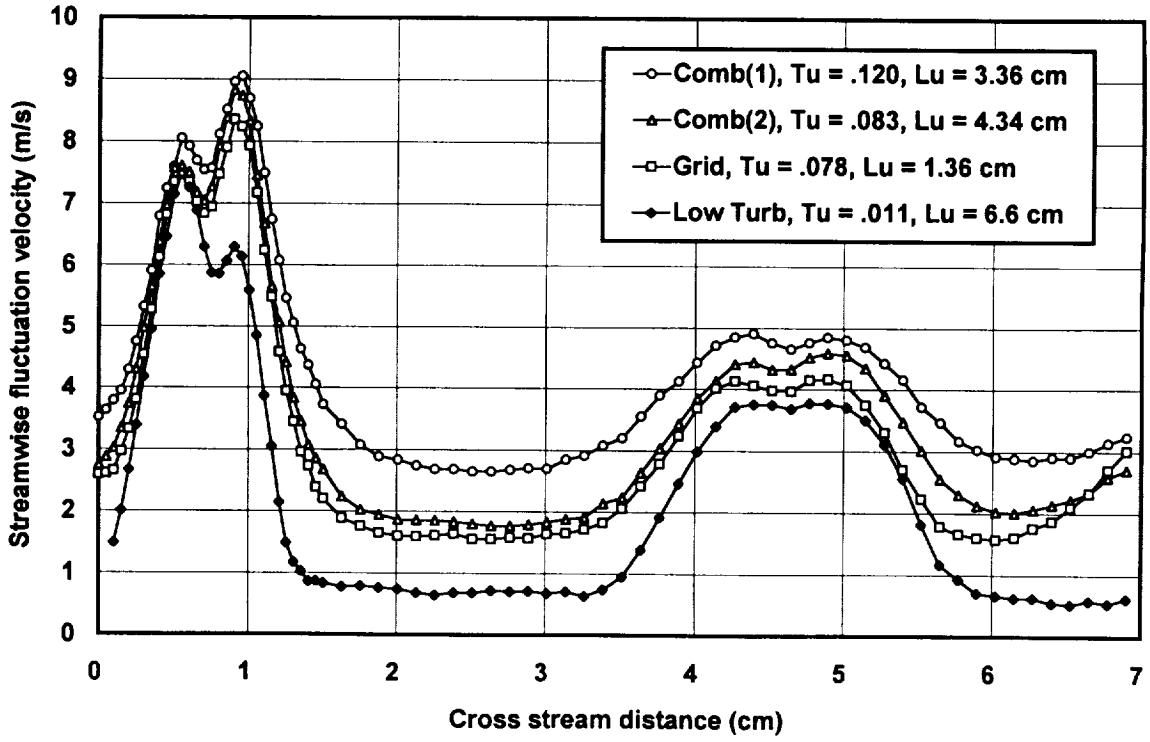

Figure 6.8 Comparison of X-wire |u'| distributions, position 8, $Ma_{ex} = 0.27$

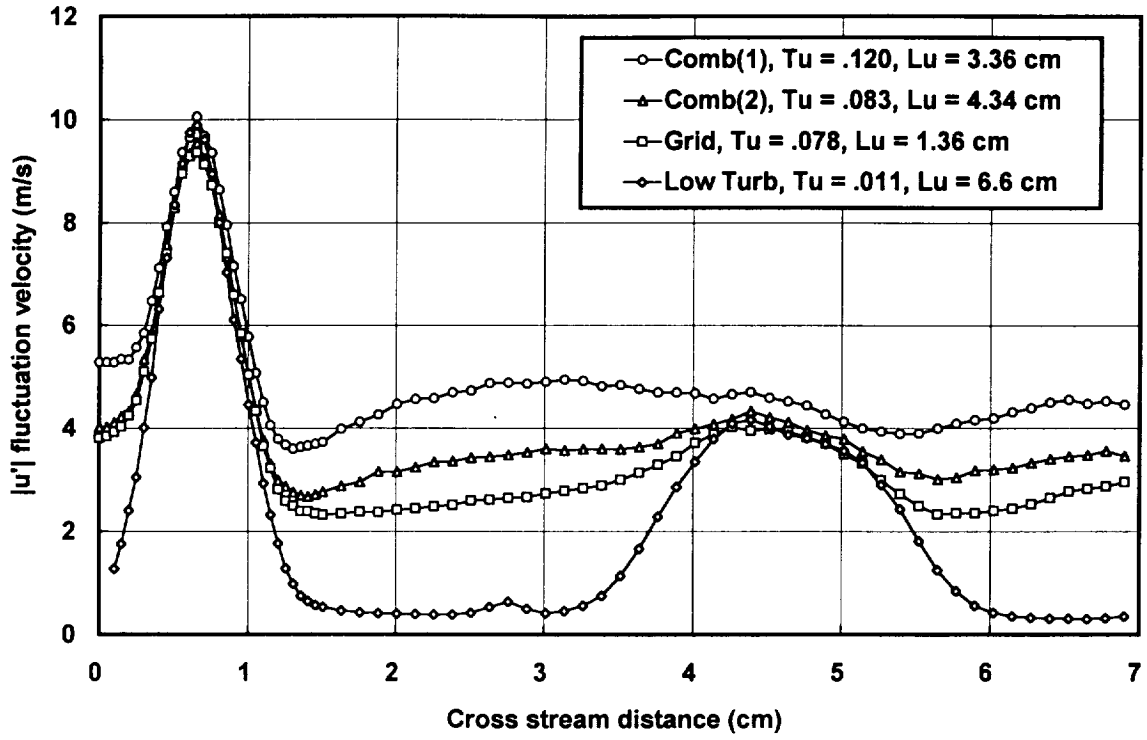

Figure 6.9 Comparison of v' distributions, position 8, $Ma_{ex} = 0.27$

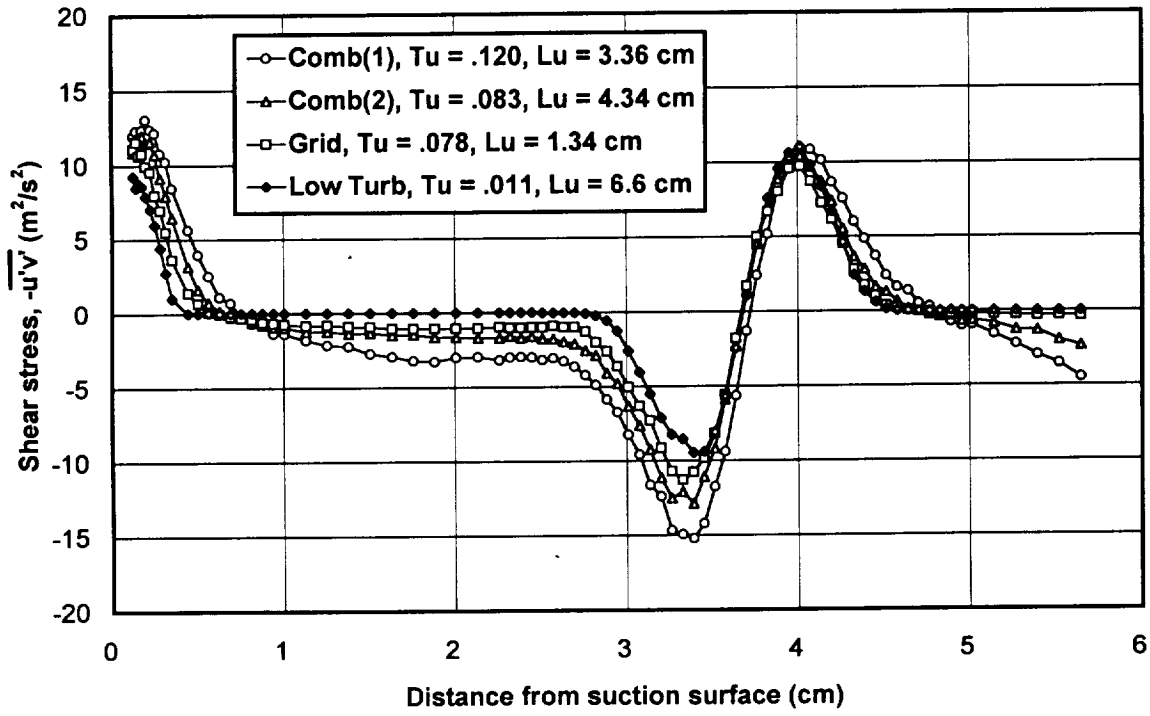

Figure 6.10 Comparison of exit shear stress distributions, position 6, $Ma_{ex} = 0.27$

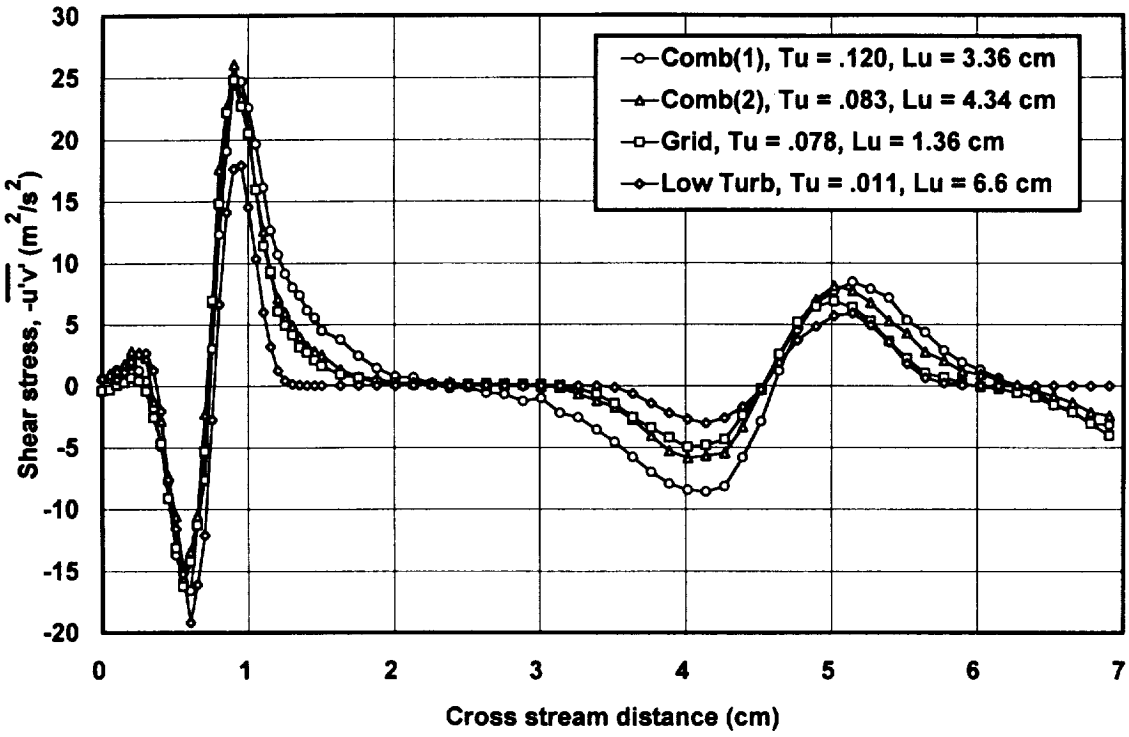

Figure 6.11 Comparison of exit shear stress measurements, position 8, $Ma_{ex} = 0.27$

Chapter 7

Summary and Conclusions

Turbulence occurs at high levels at the exit of a combustor and is known to strongly affect vane stagnation and pressure surface heat transfer. High rates of strain near the stagnation region of cylinders have been found to intensify small scale eddies which penetrate into the boundary layer and enhance heat transfer. Reasonably high rates of strain also occur along the pressure surface of an airfoil. One of the main objectives of this study was to determine to what extent this effect was responsible for high rates of heat transfer occurring on the pressure surface of a vane. In order to examine this intensification effect, the near wall and intrapassage turbulence was studied in detail. In addition to intrapassage turbulence measurements, the vane exit turbulence characteristics were documented to provide boundary conditions for the first stage rotor. Measurements of the wake losses, characteristics, and growth were taken to understand and quantify the influence of flow field turbulence on losses and the rotor turbulence boundary condition. In this section, a summary and the main conclusions of this study are given.

Inlet Turbulence Characteristics

Four turbulence conditions were developed for this study. The conditions included a low turbulence case for comparison purposes, a grid generated turbulence case, and two levels of combustor simulator turbulence. The two levels of combustor turbulence were generated by placing a mock combustor close to the inlet of the cascade for the first case and then spacing the mock combustor 25.4 cm upstream using a rectangular spool section for the second. At the vane inlet plane, the close combustor inlet turbulence was determined to be 12 percent with a 3.36 cm energy scale. The combustor with spool produced a level of 8.3 percent at the vane inlet with an energy scale of 4.34 cm. The inlet plane turbulence level for the grid turbulence was 7.8 percent with a 1.36 cm energy scale. The low turbulence case had an inlet turbulence level of about 1 percent and an energy scale of about 7 cm. Inlet turbulence characteristics are detailed in Appendix A.1.

Heat Transfer

The present data demonstrate that the length scale, Lu, has a significant effect on stagnation region and pressure surface heat transfer. The average heat transfer over the pressure surface was found to scale reasonably well on the relative level of dissipation. The stagnation region heat transfer correlated well on the parameter $\{Tu*Re_D^{5/12} (Lu/D)^{-1/3}\}$ of Ames. The dependence of augmentation on Reynolds

number was estimated to scale on the 1/3 power. The absolute level of augmentation to the heat transfer coefficient was found to be highest near the stagnation region and declined to about 70 percent of that value over the rest of the pressure surface. The close combustor turbulence, at a Reynolds number of 800,000, produced an average augmentation to heat transfer on the pressure surface of 56 percent.

Intrapassage Turbulence

The intrapassage data demonstrated how the mean level of u' fluctuations were attenuated through the passage while the mean level of v' fluctuations increased as the flow accelerated. A careful examination of the spectra revealed that most of this change occurred in the larger eddies or the low wavenumber spectra, while the highest wavenumber spectra remained largely unaffected. When the distribution of the dissipation level of the u' spectra was examined normal to the pressure surface, some intensification was seen outside of the boundary layer. This intensification was most predominate for the combustor with spool which had the largest turbulent time scale ($\tau = 1.5|u'|^2/\varepsilon$.

A comparison of the heat transfer data indicated that the combustor with spool had a slightly higher augmentation relative to the level inferred by the $Tu*Lu^{-1/3}$ scaling factor when compared at constant Reynolds number. In light of the present data, the near wall increase in dissipation found with the combustor with spool turbulence appears to be responsible for this variation. Based on the values of dissipation determined outside the boundary layer, the amplification of turbulence, while present, does not appear to be the major influence to pressure surface heat transfer augmentation in the present data. Since the straining rates outside the pressure boundary layer are much lower than the rates around the stagnation region, these conclusions are not applicable to the stagnation problem. However, the intrapassage turbulence measurements did show a significant level of turbulence production occurring within the boundary layer which was dependent on the external turbulence level and scale. The turbulence produced within the pressure surface boundary layer, due to the influence of the flow field turbulence, is most likely responsible for the enhanced mixing and therefore the high level of heat transfer augmentation.

Wake Characteristics and Development

The effect of turbulence on wake losses, wake growth, overall turbulence parameters, and on mixing were examined. Losses were broken down into losses which occurred in the free stream and losses which occurred in the wake. The elevated levels of free stream turbulence were found to correlate with significant losses in the free stream. About 1/3 to 1/2 of these background losses could be attributed to production of turbulence in the region of the flow outside the boundary layers and wake due to turbulent mixing. When these "background losses" were subtracted, the wake

losses between the turbulence cases were found to be fairly consistent. Also, about 50 to 60 percent of the losses were found to originate in the suction and pressure surface boundary layers.

The elevated free stream turbulence was also found to have a significant effect on wake growth. Generally, the wakes with elevated turbulence were found to be broader across and had smaller peak velocity deficits. The wakes with the free stream turbulence spread faster than the low turbulence case based on an estimate of the wake origins.

The overall level of turbulence and dissipation inside the wakes and in the free stream was determined and can be used to assess the expected effects of free stream and wake turbulence on rotor heat transfer augmentation. Based on the estimate that heat transfer augmentation scales on dissipation to the 1/3 power ($\varepsilon^{1/3}$), the effect of combustor turbulence combined with the wake turbulence should still have more than double the effect of the low turbulence wake alone.

Eddy diffusivities and mixing lengths were estimated using X-wire measurements of shear stress to quantify how turbulence affected mixing in the wake. The free stream turbulence was found to strongly affect eddy diffusivities. The combustor at both levels of turbulence had a bigger effect than the grid due to the larger scale. At the last measuring position, the average eddy diffusivity in the core of the close combustor wake was three times the eddy diffusivity of the low turbulence wake.

References

1. Arts, T., Lambert de Rouvroit, M., and Rutherford, A. W., 1990, "Aero-thermal Investigation of a Highly Loaded Transonic Linear Turbine Guide Vane Cascade," Technical Note 174, von Karman Institute for Fluid Dynamics, Belgium.

2. Bicen, A.F., and Jones, W.P., 1986, "Velocity characterisitics of isothermal and combusting flows in a model combustor," Combust. Sci. and Technology, Vol. 49, p. 1.

3. Ames, F.E., and Moffat, R.J., 1990, "Heat Transfer with High Intensity, Large Scale Turbulence: The Flat Plate Turbulent Boundary Layer and the Cylindrical Stagnation Point., Report No. HMT-43, Thermosciences Division of Mechanical Engineering, Stanford University.

4. Maciejewski, P.K., and Moffat, R.J., 1992, "Heat Transfer with Very High Free-Stream Turbulence: Part I -- Experimental Data and Part II -- Analysis of Results," ASME Journal of Heat Transfer Vol. 114, p. 827.

5. Hunt, J.C.R., and Graham, J.M.R., 1978, "Free-Stream Turbulence Near Plane Boundaries," J. Fluid Mech, Vol. 84, p. 209.

6. Thomas, N.H., and Hancock, P.E., 1977, "Grid Turbulence Near A Moving Wall," J. Fluid Mech., Vol. 82, Part 3, p. 481.

7. Blair, M.F., 1983, "Influence of Free-Stream Turbulence on the Zero-Pressure Gradient Fully Turbulent Boundary Layer," Part I -- Experimental Data and Part II -- Analysis of Results," J. Heat Transfer, Vol. 105, p. 33.

8. Blair, M.F., 1981, "Velocity and Temperature Profile Data for Zero Pressure Gradient Fully Turbulent Boundary Layer," UTRC Report R80-914388-12.

9. Hancock, P.E., and Bradshaw, P. 1983, "The Effect of Free-Stream Turbulence on Turbulent Boundary Layer Flow and Heat Transfer," J. Fluids Engr., Vol. 105, p. 284.

10. Kestin, J., and Wood, R.T., 1971, "The Influence of Turbulence on Mass Transfer from Cylinders," J. Heat Transfer, p. 321.

11. Lowery, G.W., and Vachon, R.I., 1975, "The Effect of Turbulence on Heat Transfer for Heated Cylinders," Int. J. Heat Mass Transfer, Vol. 18, p. 1229.

12. Smith, M.C., and Kuethe, A.M., 1966, "Effects of Turbulence on Laminar Skin Friction and Heat Transfer," Physics of Fluids, Vol. 9, No. 12, p. 2337.

13. Van Fossen, G.J., and Simoneau, R.J., 1994, "Stagnation Region Heat Transfer: The Influence of Turbulence Parameters, Reynolds Number, and Body Shape," AIAA/ASME Thermophysics and Heat Transfer Conference, Colorado Springs, Colorado, June 20-23, 1994.

14. Van Fossen, G.J., and Ching, C.Y., 1994, "Measurements of the Influence of Integral Length Scale on Stagnation Region Heat Transfer," Fifth Int. Sym. on Transport Phenomena and Dynamics of Rotating Machinery (ISROMAC-5), Kaanapali, Maui, Hawaii, Paper No. TP-16.

15. Hunt, J.C.R., 1973, "A Theory of Turbulent Flow Round Two-Dimensional Bluff Bodies," J. Fluid Mech, Vol. 61, Part 4, p. 625.

16. Britter, R.E., Hunt, J.C.R., and Mumford, J.C., 1979, "The Distortion of Turbulence by a Circular Cylinder, " J. Fluid Mech., Vol. 92.

17. Zimmerman, D.R., 1990, "Three-Dimensional Laser Anemometer Measurements in a Linear Turbine Vane Cascade," Forum on Turbulent Flows -- 1990, ASME FED Vol. 94, p. 143.

18. Nealy, D.A., Mihelc, M.S., Hylton, L.D., and Gladden, H.J., 1983, "Measurements of Heat Transfer Distribution Over the Surfaces of Highly Loaded Turbine Nozzle Guide Vanes," ASME paper No. 83-GT-53.

19. Kays, W.M., 1987, "STAN7, a finite difference boundary layer code."

20. Frota, M.F., 1982, "Analysis of the Uncertainties in Velocity Measurements and Technique for Turbulence Measurements in Complex Heated Flows with Multiple Hot-Wires," Ph.D. Dissertation, Dept. Mech. Engr., Stanford University.

21. Kline, S.J., and McClintock, F.A., Jan., 1953, "Describing Uncertainties in Single Sample Experiments," Mech. Engr., p. 3.

22. Wubben, F.J.W., 1991, "Single and Cross Hot Wire Anemometry in Incompressible Flow," Report LR-663, Faculty of Aerospace Engineering, Delft University of Technology

23. Hinze, J., 1975, Turbulence, 2nd Ed., McGraw-Hill, New York.

24. Denton, J.D., 1993, "Loss Mechanisms in Turbomachines," ASME Paper No. 93-GT-435, Presented at the International Gas Turbine and Aeroengine Congress and Exposition, Cincinnati, Ohio, May, 1993.

25. Glassman, A.J., editor, 1973, Turbine Design and Application, NASA SP-290, National Aeronautics and Space Administration, 1973.

26. Moffat, R.J., 1980, "Experimental Methods in the Thermosciences," Dept. Mech. Engr., Stanford, University.

Appendix A.1 Inlet Turbulence Characteristics

	File	Tu	Vel (m/s)	Lx (cm)	Lu (cm)	Diss (m^2/s^3)	Y (cm)	Pos
Comb(1)	IR8CB1	0.1259	29.69	1.509	3.086	2542	3.810	6
	IR8CB2	0.1323	29.50	1.826	3.457	2580	2.540	6
	IR8CB3	0.1269	29.26	1.643	3.205	2396	5.080	6
	IR8CB4	0.1972	22.66	2.261	5.022	2661	0.127	6
	IR8CB5	0.1840	25.92	2.807	6.777	2414	0.318	6
	IR8CB6	0.1468	28.71	2.840	5.118	2197	1.016	6
	IR8CB7	0.1247	29.70	1.433	3.119	2439	3.810	2
	IR8CB8	0.1327	29.34	2.004	3.698	2390	2.540	2
	IR8CB9	0.1314	29.46	1.798	3.602	2415	5.080	2
	IR5CB1	0.1310	19.69	1.560	3.137	821	3.810	2
	IR5CB2	0.1360	19.37	1.567	3.193	858	3.810	6
Comb(2)	IC8CB1	0.0834	29.21	1.687	3.523	616	3.810	6
	IC8CB2	0.0852	29.27	2.101	3.825	608	2.540	6
	IC8CB3	0.0836	29.30	1.816	3.625	608	5.080	6
	IC8CB4	0.1262	23.81	2.319	2.497	1629	0.127	6
	IC8CB5	0.1052	26.42	3.254	5.324	605	0.318	6
	IC8CB6	0.0924	28.56	3.142	6.345	434	1.016	6
	IC8CB7	0.0886	29.30	2.283	4.961	528	3.810	2
	IC8CB8	0.0912	29.27	2.756	5.484	526	2.540	2
	IC8CB9	0.0839	29.37	1.956	4.605	487	5.080	2
	IC5CB1	0.0868	19.23	2.136	4.717	148	3.810	2
	IC5CB2	0.0798	19.31	2.019	3.978	138	3.810	6
Grid	IR8G21	0.0760	30.93	1.196	1.349	1434	3.810	2
	IR8G22	0.0770	31.10	1.201	1.359	1528	2.540	2
	IR8G23	0.0780	29.83	1.153	1.364	1363	5.080	2
	IR8G24	0.0770	30.13	1.059	1.265	1495	3.810	6
	IR8G25	0.0790	30.93	1.237	1.407	1576	5.080	6
	IR8G26	0.0780	30.12	1.041	1.400	1498	2.540	6
	IR8G27	0.1070	25.58	1.651	1.770	1732	0.127	6
	IR8G28	0.0890	28.13	1.768	2.111	1110	0.318	6
	IR8G29	0.0790	29.55	1.588	1.539	1254	1.016	6
	IR5G21	0.0718	19.83	1.245	1.110	390	3.810	2
	IR5G22	0.0777	18.99	0.958	1.095	440	3.810	6
Low Turb	IR8C21	0.0090	29.87	6.708	15.662	0.177	3.810	6
	IR8C22	0.0065	29.71	6.510	5.695	0.192	2.540	6
	IR8C23	0.0136	29.13	3.629	11.844	0.782	5.080	6
	IR8C24	0.0095	29.78	5.316	5.712	0.589	3.810	2
	IR8C25	0.0117	29.78	4.445	9.528	0.668	2.540	2
	IR8C26	0.0145	29.22	4.054	5.695	2.019	5.080	2
	IR5C21	0.0088	19.23	8.336	16.561	0.045	3.810	6
	IR5C22	0.0096	19.44	8.654	21.717	0.045	3.810	2

Appendix A.2 Vane Pressure Distributions

The eight pages following this page contain pressure distributions for the four turbulence cases taken at the two Reynolds number conditions. The surface distance given in the tables can be correlated to the data in chapters 2 and 4 by subtracting 133.35 mm from the surface distance.

File:	CVANE03			
Ptot	93648	Pa		
Ttot	27.12	C	Ts,ex	295.94 K
Main	0.0829		Re,ex	772291
Maex	0.2704		Tu,in	0.011
Ps,ex	89010	Pa	Lu,in	66.0 mm
Ps,in	93199	Pa	U0,in	29.58 m/s

#	Surface (mm)	Ps/Pt
1	0.00	0.95019
2	7.62	0.95513
3	15.24	0.96022
4	22.86	0.96478
5	30.48	0.97035
6	38.10	0.97572
7	45.72	0.98067
8	53.34	0.98498
9	60.96	0.98844
10	68.58	0.99112
11	76.20	0.99290
12	83.82	0.99456
13	91.44	0.99572
14	99.06	0.99667
15	106.68	0.99735
16	114.30	0.99795
17	121.92	0.99846
18	129.54	0.99928
19	137.16	0.99926
20	144.78	0.99311
21	152.40	0.98043
22	160.02	0.95981
23	167.64	0.92313
24	175.26	0.91330
25	182.88	0.91739
26	190.50	0.92253
27	198.12	0.93515
28	205.74	0.93956
29	213.36	0.94207
30	220.98	0.94314
31	228.60	0.94511
32	236.22	0.94608
33	243.84	0.94728
34	251.46	0.94736
35	259.08	0.94744
36	266.70	0.94773
37	274.32	0.94761
38	281.94	0.94757
39	289.56	0.94756
40	297.18	0.94749
41	304.80	0.94761
42	312.42	0.94748
43	320.04	0.95019

File:	CVANE51				
Ptot	95651	Pa			
Ttot	24.89	C	Ts,ex	296.33	K
Main	0.0537		Re,ex	509698	
Maex	0.1697		Tu,in	0.009	
Ps,ex	93747	Pa	Lu,in	191.4	mm
Ps,in	95458	Pa	U0,in	19.34	m/s

#	Surface (mm)	Ps/Pt
1	0.00	0.97949
2	7.62	0.98158
3	15.24	0.98360
4	22.86	0.98556
5	30.48	0.98776
6	38.10	0.98990
7	45.72	0.99187
8	53.34	0.99355
9	60.96	0.99505
10	68.58	0.99615
11	76.20	0.99698
12	83.82	0.99769
13	91.44	0.99819
14	99.06	0.99858
15	106.68	0.99888
16	114.30	0.99916
17	121.92	0.99937
18	129.54	0.99976
19	137.16	0.99967
20	144.78	0.99689
21	152.40	0.99151
22	160.02	0.98297
23	167.64	0.96822
24	175.26	0.96530
25	182.88	0.96621
26	190.50	0.96863
27	198.12	0.97287
28	205.74	0.97563
29	213.36	0.97650
30	220.98	0.97687
31	228.60	0.97764
32	236.22	0.97802
33	243.84	0.97831
34	251.46	0.97844
35	259.08	0.97854
36	266.70	0.97870
37	274.32	0.97865
38	281.94	0.97868
39	289.56	0.97868
40	297.18	0.97866
41	304.80	0.97870
42	312.42	0.97875
43	320.04	0.97949

File:	CBVANE04			
Ptot	94804	Pa		
Ttot	26.31	C	Ts,ex	295.23 K
Main	0.0824		Re,ex	777688
Maex	0.2679		Tu,in	0.120
Ps,ex	90192	Pa	Lu,in	33.6 mm
Ps,in	94355	Pa	U0,in	29.49 m/s

#	Surface (mm)	Ps/Pt
1	0.00	0.95029
2	7.62	0.95605
3	15.24	0.96098
4	22.86	0.96578
5	30.48	0.97146
6	38.10	0.97670
7	45.72	0.98159
8	53.34	0.98570
9	60.96	0.98891
10	68.58	0.99147
11	76.20	0.99320
12	83.82	0.99491
13	91.44	0.99597
14	99.06	0.99694
15	106.68	0.99758
16	114.30	0.99809
17	121.92	0.99849
18	129.54	0.99929
19	137.16	0.99942
20	144.78	0.99390
21	152.40	0.98192
22	160.02	0.96159
23	167.64	0.92595
24	175.26	0.91684
25	182.88	0.91766
26	190.50	0.92765
27	198.12	0.93593
28	205.74	0.94100
29	213.36	0.94379
30	220.98	0.94493
31	228.60	0.94685
32	236.22	0.94777
33	243.84	0.94856
34	251.46	0.94906
35	259.08	0.94925
36	266.70	0.94966
37	274.32	0.94941
38	281.94	0.94936
39	289.56	0.94945
40	297.18	0.94946
41	304.80	0.94956
42	312.42	0.94932
43	320.04	0.95029

File:	CBVANE52				
Ptot	96425	Pa			
Ttot	26.02	C	Ts,ex	297.45	K
Main	0.0541		Re,ex	511930	
Maex	0.1699		Tu,in	0.124	
Ps,ex	94501	Pa	Lu,in	31.6	mm
Ps,in	96228	Pa	U0,in	19.53	m/s

#	Surface (mm)	Ps/Pt
1	0.00	0.97957
2	7.62	0.98189
3	15.24	0.98384
4	22.86	0.98579
5	30.48	0.98801
6	38.10	0.99013
7	45.72	0.99203
8	53.34	0.99374
9	60.96	0.99510
10	68.58	0.99616
11	76.20	0.99693
12	83.82	0.99755
13	91.44	0.99802
14	99.06	0.99833
15	106.68	0.99861
16	114.30	0.99886
17	121.92	0.99904
18	129.54	0.99933
19	137.16	0.99944
20	144.78	0.99703
21	152.40	0.99205
22	160.02	0.98358
23	167.64	0.96913
24	175.26	0.96520
25	182.88	0.96582
26	190.50	0.96962
27	198.12	0.97343
28	205.74	0.97536
29	213.36	0.97642
30	220.98	0.97700
31	228.60	0.97776
32	236.22	0.97815
33	243.84	0.97849
34	251.46	0.97862
35	259.08	0.97871
36	266.70	0.97888
37	274.32	0.97884
38	281.94	0.97887
39	289.56	0.97889
40	297.18	0.97889
41	304.80	0.97888
42	312.42	0.97892
43	320.04	0.97957

File:	CBSVN01				
Ptot	94115	Pa			
Ttot	27.44	C	Ts,ex	296.36	K
Main	0.0809		Re,ex	765934	
Maex	0.2670		Tu,in	0.083	
Ps,ex	89566	Pa	Lu,in	43.4	mm
Ps,in	93685	Pa	U0,in	29.29	m/s

#	Surface (mm)	Ps/Pt
1	0.00	0.94999
2	7.62	0.95477
3	15.24	0.95972
4	22.86	0.96510
5	30.48	0.97050
6	38.10	0.97584
7	45.72	0.98071
8	53.34	0.98502
9	60.96	0.98841
10	68.58	0.99088
11	76.20	0.99268
12	83.82	0.99440
13	91.44	0.99525
14	99.06	0.99576
15	106.68	0.99650
16	114.30	0.99702
17	121.92	0.99753
18	129.54	0.99832
19	137.16	0.99828
20	144.78	0.99294
21	152.40	0.98031
22	160.02	0.96047
23	167.64	0.92551
24	175.26	0.91535
25	182.88	0.91611
26	190.50	0.92597
27	198.12	0.93571
28	205.74	0.93972
29	213.36	0.94232
30	220.98	0.94334
31	228.60	0.94530
32	236.22	0.94602
33	243.84	0.94742
34	251.46	0.94805
35	259.08	0.94828
36	266.70	0.94857
37	274.32	0.94835
38	281.94	0.94849
39	289.56	0.94860
40	297.18	0.94851
41	304.80	0.94838
42	312.42	0.94827
43	320.04	0.94999

File:	CBSVN51				
Ptot	95405	Pa			
Ttot	29.53	C	Ts,ex	300.95	K
Main	0.0543		Re,ex	498041	
Maex	0.1695		Tu,in	0.080	
Ps,ex	93510	Pa	Lu,in	43.4	mm
Ps,in	95209	Pa	U0,in	19.27	m/s

#	Surface (mm)	Ps/Pt
1	0.00	0.98027
2	7.62	0.98243
3	15.24	0.98455
4	22.86	0.98643
5	30.48	0.98833
6	38.10	0.99010
7	45.72	0.99210
8	53.34	0.99378
9	60.96	0.99513
10	68.58	0.99610
11	76.20	0.99678
12	83.82	0.99736
13	91.44	0.99859
14	99.06	0.99898
15	106.68	0.99923
16	114.30	0.99944
17	121.92	0.99968
18	129.54	0.99994
19	137.16	1.00003
20	144.78	0.99757
21	152.40	0.99250
22	160.02	0.98421
23	167.64	0.96952
24	175.26	0.96507
25	182.88	0.96588
26	190.50	0.96908
27	198.12	0.97343
28	205.74	0.97543
29	213.36	0.97664
30	220.98	0.97713
31	228.60	0.97790
32	236.22	0.97832
33	243.84	0.97864
34	251.46	0.97875
35	259.08	0.97892
36	266.70	0.97899
37	274.32	0.97900
38	281.94	0.97896
39	289.56	0.97900
40	297.18	0.97909
41	304.80	0.97907
42	312.42	0.97906
43	320.04	0.98027

File:	GVANE21				
Ptot	95143	Pa			
Ttot	27.84	C	Ts,ex	296.67	K
Main	0.0847		Re,ex	781171	
Maex	0.2700		Tu,in	0.078	
Ps,ex	90443	Pa	Lu,in	13.6	mm
Ps,in	94667	Pa	U0,in	30.51	m/s

#	Surface (mm)	Ps/Pt
1	0.00	0.95000
2	7.62	0.95531
3	15.24	0.96020
4	22.86	0.96497
5	30.48	0.97045
6	38.10	0.97577
7	45.72	0.98062
8	53.34	0.98480
9	60.96	0.98817
10	68.58	0.99075
11	76.20	0.99254
12	83.82	0.99412
13	91.44	0.99523
14	99.06	0.99616
15	106.68	0.99679
16	114.30	0.99741
17	121.92	0.99790
18	129.54	0.99871
19	137.16	0.99899
20	144.78	0.99290
21	152.40	0.98048
22	160.02	0.95982
23	167.64	0.92341
24	175.26	0.91372
25	182.88	0.91520
26	190.50	0.92534
27	198.12	0.93489
28	205.74	0.93970
29	213.36	0.94240
30	220.98	0.94351
31	228.60	0.94554
32	236.22	0.94627
33	243.84	0.94711
34	251.46	0.94766
35	259.08	0.94791
36	266.70	0.94822
37	274.32	0.94812
38	281.94	0.94806
39	289.56	0.94822
40	297.18	0.94810
41	304.80	0.94813
42	312.42	0.94811
43	320.04	0.95000

File:	GVANE51				
Ptot	96602	Pa			
Ttot	26.70	C	Ts,ex	298.13	K
Main	0.0549		Re,ex	511398	
Maex	0.1699		Tu,in	0.075	
Ps,ex	94675	Pa	Lu,in	11.0	mm
Ps,in	96399	Pa	U0,in	19.41	m/s

#	Surface (mm)	Ps/Pt
1	0.00	0.97979
2	7.62	0.98178
3	15.24	0.98383
4	22.86	0.98573
5	30.48	0.98792
6	38.10	0.99005
7	45.72	0.99202
8	53.34	0.99375
9	60.96	0.99511
10	68.58	0.99615
11	76.20	0.99686
12	83.82	0.99753
13	91.44	0.99800
14	99.06	0.99837
15	106.68	0.99864
16	114.30	0.99889
17	121.92	0.99907
18	129.54	0.99942
19	137.16	0.99952
20	144.78	0.99698
21	152.40	0.99176
22	160.02	0.98314
23	167.64	0.96843
24	175.26	0.96509
25	182.88	0.96587
26	190.50	0.96906
27	198.12	0.97349
28	205.74	0.97537
29	213.36	0.97640
30	220.98	0.97695
31	228.60	0.97767
32	236.22	0.97814
33	243.84	0.97848
34	251.46	0.97859
35	259.08	0.97871
36	266.70	0.97879
37	274.32	0.97883
38	281.94	0.97885
39	289.56	0.97887
40	297.18	0.97885
41	304.80	0.97889
42	312.42	0.97898
43	320.04	0.97979

Appendix A.3 Heat Transfer Distributions

The eleven pages following this page contain heat transfer distributions for the four turbulence cases taken at the two Reynolds number conditions. The surface distance given in the tables can be correlated to the data in chapters 2 and 4 by subtracting 133.34 mm from the surface distance. Also, the data from points 1 and 39 do not correlate well with the rest of the data. These points lie very close to the beginning of heating. This discrepancy could be due to a number of reasons. Based on the consistency of the remaining points these points are associated with significant errors and should not be used for analysis.

File:	HTB100				
Ptot	95745	Pa	Ts,ex	296.40	K
Ttot	27.44	C	Re,ex	776143	
Main	0.0807		q"	1406.2	W/m2
Maex	0.2659		Tu,in	0.011	
Ps,ex	91152	Pa	Lu,in	66.0	mm
Ps,in	95310	Pa	U0,in	29.58	m/s

#	Surface (mm)	Tsurf (C)	Taw (C)	h (W/m2-C)	St
1	10.96	39.76	26.96	71.53	0.000724
2	18.87	40.78	27.02	83.05	0.000840
3	26.07	40.83	27.07	87.35	0.000884
4	32.97	40.81	27.12	89.39	0.000905
5	40.15	41.25	27.19	87.96	0.000890
6	48.16	41.76	27.27	84.85	0.000859
7	55.63	42.01	27.31	84.52	0.000855
8	64.28	42.34	27.35	83.38	0.000844
9	71.09	42.61	27.31	82.02	0.000830
10	77.95	42.74	27.35	82.08	0.000831
11	86.01	42.87	27.38	82.10	0.000831
12	93.79	42.48	27.38	85.40	0.000864
13	101.60	42.20	27.42	88.02	0.000891
14	109.27	41.60	27.45	92.56	0.000937
15	117.37	40.02	27.48	106.80	0.001081
16	124.58	37.71	27.51	135.34	0.001370
17	132.43	34.95	27.50	191.36	0.001936
18	140.67	34.75	27.45	195.02	0.001974
19	148.74	35.11	27.35	181.24	0.001834
20	157.27	34.66	27.13	187.41	0.001897
21	164.86	34.20	26.82	193.41	0.001957
22	170.62	34.40	26.47	180.57	0.001827
23	177.31	35.34	26.43	158.22	0.001601
24	185.42	38.74	26.45	109.47	0.001108
25	193.00	40.80	26.34	86.77	0.000878
26	200.41	31.42	26.23	294.32	0.002978
27	208.60	31.21	26.57	324.56	0.003284
28	217.46	31.65	26.71	302.48	0.003061
29	223.89	31.99	26.77	286.58	0.002900
30	231.42	32.23	26.84	278.74	0.002821
31	239.23	32.50	26.88	270.95	0.002742
32	246.95	32.91	27.01	259.64	0.002627
33	255.10	33.15	27.04	250.35	0.002533
34	262.48	33.33	27.05	245.59	0.002485
35	269.70	33.55	27.05	238.41	0.002413
36	277.68	33.68	27.05	234.86	0.002377
37	283.57	34.06	27.06	223.10	0.002258
38	293.75	34.27	27.01	215.81	0.002184
39	300.97	33.51	27.02	264.00	0.002672

File:	HTB200				
Ptot	96754	Pa	Ts,ex	299.25	K
Ttot	27.81	K	Re,ex	508238	
Ma,in	0.0525		q"	1405.4	W/m2
Ma,ex	0.1693		Tu,in	0.009	
Ps,in	96567	Pa	Lu,in	191.4	mm
Ps,ex	94837	Pa	U0,in	19.34	m/s

#	Surface (mm)	T surf (C)	T aw (C)	h (W/m2-C)	St
1	10.96	43.37	27.60	51.70	0.000793
2	18.87	44.66	27.61	64.99	0.000997
3	26.07	44.68	27.63	69.24	0.001062
4	32.97	44.62	27.65	70.88	0.001088
5	40.15	45.08	27.68	69.95	0.001073
6	48.16	45.60	27.73	67.61	0.001037
7	55.63	45.85	27.76	67.45	0.001035
8	64.28	46.19	27.78	66.74	0.001024
9	71.09	46.49	27.75	65.73	0.001009
10	77.95	46.61	27.77	65.87	0.001011
11	86.01	46.71	27.78	66.05	0.001014
12	93.79	46.24	27.80	68.96	0.001058
13	101.60	45.87	27.82	71.18	0.001092
14	109.27	45.11	27.83	74.98	0.001151
15	117.37	43.19	27.85	86.76	0.001331
16	124.58	40.42	27.85	109.67	0.001683
17	132.43	37.11	27.82	154.27	0.002367
18	140.67	36.88	27.78	157.44	0.002416
19	148.74	37.34	27.74	146.95	0.002255
20	157.27	36.98	27.65	151.68	0.002328
21	164.86	36.66	27.53	157.36	0.002415
22	170.62	37.18	27.40	147.10	0.002257
23	177.31	38.46	27.40	126.95	0.001948
24	185.42	43.38	27.40	82.20	0.001261
25	193.00	45.78	27.49	65.75	0.001009
26	200.41	34.33	27.12	212.55	0.003262
27	208.60	33.13	27.29	262.25	0.004024
28	217.46	33.78	27.40	236.28	0.003626
29	223.89	34.29	27.45	219.86	0.003374
30	231.42	34.70	27.49	209.74	0.003219
31	239.23	35.15	27.52	200.98	0.003084
32	246.95	35.64	27.60	191.85	0.002944
33	255.10	35.99	27.63	184.29	0.002828
34	262.48	36.28	27.62	179.45	0.002754
35	269.70	36.57	27.63	174.66	0.002680
36	277.68	36.82	27.61	170.33	0.002614
37	283.57	37.28	27.62	162.80	0.002498
38	293.75	37.62	27.59	156.55	0.002402
39	300.97	36.75	27.62	192.73	0.002958

File:	HTB300				
Ptot	97116	Pa	Ts,ex	296.31	K
Ttot	27.51	C	Re,ex	802227	
Ma,in	0.0819		q"	1781.0	W/m2
Ma,ex	0.2709		Tu,in	0.011	
Ps,in	96661	Pa	Lu,in	66.0	mm
Ps,ex	92286	Pa	U0,in	29.58	m/s

#	Surface (mm)	T surf (C)	T aw (C)	h (W/M2-C)	St
1	10.96	42.70	27.00	74.75	0.000733
2	18.87	44.31	27.05	83.67	0.000820
3	26.07	44.36	27.11	88.22	0.000865
4	32.97	44.32	27.15	90.32	0.000885
5	40.15	44.92	27.22	88.53	0.000868
6	48.16	45.52	27.29	85.47	0.000838
7	55.63	45.83	27.33	85.06	0.000834
8	64.28	46.24	27.35	83.93	0.000823
9	71.09	46.62	27.35	82.52	0.000809
10	77.95	46.80	27.39	82.45	0.000808
11	86.01	46.95	27.41	82.48	0.000809
12	93.79	46.48	27.40	85.72	0.000840
13	101.60	46.13	27.43	88.20	0.000865
14	109.27	45.37	27.45	92.59	0.000908
15	117.37	43.36	27.49	106.91	0.001048
16	124.58	40.42	27.53	135.69	0.001330
17	132.43	36.91	27.56	193.47	0.001897
18	140.67	36.65	27.50	197.16	0.001933
19	148.74	37.11	27.40	183.53	0.001799
20	157.27	36.59	27.18	190.06	0.001863
21	164.86	36.08	26.87	196.21	0.001923
22	170.62	36.37	26.50	183.50	0.001799
23	177.31	37.54	26.44	160.97	0.001578
24	185.42	41.62	26.48	112.79	0.001106
25	193.00	44.58	26.38	87.26	0.000855
26	200.41	33.01	26.38	290.27	0.002845
27	208.60	32.51	26.68	326.92	0.003205
28	217.46	32.96	26.81	307.48	0.003014
29	223.89	33.34	26.86	291.79	0.002860
30	231.42	33.62	26.92	283.55	0.002780
31	239.23	33.92	26.94	276.34	0.002709
32	246.95	34.38	27.05	264.13	0.002589
33	255.10	34.65	27.07	255.61	0.002506
34	262.48	34.90	27.09	250.14	0.002452
35	269.70	35.15	27.09	243.69	0.002389
36	277.68	35.32	27.08	239.34	0.002346
37	283.57	35.79	27.08	227.15	0.002227
38	293.75	36.04	27.03	220.33	0.002160
39	300.97	35.04	27.02	269.96	0.002646

File:	HTB400		
Ptot	97958 Pa	Ts,ex	299.23 K
Ttot	27.81 C	Re,ex	515943
Ma,in	0.0529	q"	1451.0 W/m2
Ma,ex	0.1697	Tu,in	0.009
Ps,in	97766 Pa	Lu,in	191.4 mm
Ps,ex	96007 Pa	U0,in	19.34 m/s

#	Surface (mm)	T surf (C)	T aw (C)	h (W/m2-C)	St
1	10.96	43.62	27.62	53.06	0.000802
2	18.87	45.22	27.64	64.73	0.000979
3	26.07	45.25	27.66	69.02	0.001043
4	32.97	45.19	27.68	70.72	0.001069
5	40.15	45.72	27.71	69.56	0.001052
6	48.16	46.24	27.75	67.24	0.001017
7	55.63	46.52	27.78	67.04	0.001014
8	64.28	46.87	27.79	66.34	0.001003
9	71.09	47.21	27.77	65.29	0.000987
10	77.95	47.34	27.80	65.42	0.000989
11	86.01	47.45	27.82	65.67	0.000993
12	93.79	46.98	27.84	68.46	0.001035
13	101.60	46.60	27.86	70.72	0.001069
14	109.27	45.81	27.86	74.47	0.001126
15	117.37	43.79	27.87	86.23	0.001304
16	124.58	40.89	27.88	109.34	0.001653
17	132.43	37.43	27.86	154.62	0.002338
18	140.67	37.18	27.83	158.05	0.002390
19	148.74	37.65	27.78	147.59	0.002231
20	157.27	37.25	27.69	152.79	0.002310
21	164.86	36.91	27.58	158.80	0.002401
22	170.62	37.42	27.43	148.67	0.002248
23	177.31	38.71	27.43	128.69	0.001946
24	185.42	43.56	27.45	84.51	0.001278
25	193.00	46.40	27.48	65.63	0.000992
26	200.41	34.84	27.21	206.16	0.003117
27	208.60	33.34	27.38	265.13	0.004009
28	217.46	33.96	27.47	240.17	0.003631
29	223.89	34.46	27.51	223.66	0.003382
30	231.42	34.84	27.54	213.91	0.003234
31	239.23	35.28	27.56	205.54	0.003108
32	246.95	35.79	27.62	195.15	0.002951
33	255.10	36.12	27.65	188.34	0.002848
34	262.48	36.43	27.64	182.95	0.002766
35	269.70	36.73	27.65	178.09	0.002693
36	277.68	36.98	27.63	173.57	0.002624
37	283.57	37.44	27.63	165.78	0.002506
38	293.75	37.78	27.60	159.78	0.002416
39	300.97	36.86	27.60	196.17	0.002966

File:	HTB500				
Ptot	96872	Pa	Ts,ex	298.84	K
Ttot	27.42	C	Re,ex	512026	
Ma,in	0.0526		q"	559.2	W/m2
Ma,ex	0.1702		Tu,in	0.009	
Ps,in	96685	Pa	Lu,in	191.4	mm
Ps,ex	94934	Pa	U0,in	19.34	m/s

#	Surface (mm)	T surf (C)	T aw (C)	h (W/m2-C)	St
1	10.96	33.59	27.20	49.91	0.000761
2	18.87	34.09	27.21	63.89	0.000974
3	26.07	34.11	27.24	68.03	0.001037
4	32.97	34.11	27.26	69.58	0.001061
5	40.15	34.31	27.29	68.70	0.001047
6	48.16	34.55	27.34	66.39	0.001012
7	55.63	34.68	27.37	66.10	0.001008
8	64.28	34.84	27.39	65.19	0.000994
9	71.09	34.94	27.36	64.37	0.000981
10	77.95	35.00	27.38	64.51	0.000983
11	86.01	35.07	27.39	64.42	0.000982
12	93.79	34.90	27.41	67.07	0.001023
13	101.60	34.77	27.43	69.25	0.001056
14	109.27	34.47	27.43	72.95	0.001112
15	117.37	33.69	27.46	84.66	0.001291
16	124.58	32.56	27.46	107.25	0.001635
17	132.43	31.19	27.43	151.37	0.002308
18	140.67	31.09	27.39	153.58	0.002341
19	148.74	31.25	27.35	143.54	0.002188
20	157.27	31.03	27.26	149.52	0.002280
21	164.86	30.84	27.14	154.37	0.002353
22	170.62	30.96	27.01	144.93	0.002210
23	177.31	31.46	27.00	125.81	0.001918
24	185.42	33.43	27.01	81.60	0.001244
25	193.00	34.51	27.10	64.28	0.000980
26	200.41	29.64	26.73	211.84	0.003230
27	208.60	29.30	26.90	255.20	0.003891
28	217.46	29.61	27.00	231.37	0.003527
29	223.89	29.84	27.06	216.42	0.003299
30	231.42	30.01	27.10	207.53	0.003164
31	239.23	30.19	27.12	200.57	0.003058
32	246.95	30.45	27.21	190.45	0.002904
33	255.10	30.60	27.23	182.60	0.002784
34	262.48	30.71	27.23	178.40	0.002720
35	269.70	30.82	27.24	174.02	0.002653
36	277.68	30.91	27.22	169.81	0.002589
37	283.57	31.09	27.23	162.68	0.002480
38	293.75	31.21	27.20	156.64	0.002388
39	300.97	30.86	27.23	193.80	0.002955

File:	HTC200				
Ptot	95373	Pa	Ts,ex	293.69	K
Ttot	24.84	C	Re,ex	794625	
Ma,in	0.0805		q"	2268.9	W/m2
Ma,ex	0.27052		Tu,in	0.120	
Ps,in	94942	Pa	Lu,in	33.6	mm
Ps,ex	90644	Pa	U0,in	29.49	m/s

#	Surface (mm)	T surf (C)	T aw (C)	h (W/m2-C)	St
1	10.96	38.16	24.44	126.63	0.001262
2	18.87	39.56	24.46	134.60	0.001341
3	26.07	39.55	24.51	140.00	0.001395
4	32.97	39.45	24.58	143.02	0.001425
5	40.15	40.03	24.64	138.90	0.001384
6	48.16	40.38	24.71	135.68	0.001352
7	55.63	40.56	24.76	135.11	0.001347
8	64.28	40.86	24.80	133.28	0.001328
9	71.09	41.17	24.81	130.92	0.001305
10	77.95	41.29	24.84	130.53	0.001301
11	86.01	41.45	24.87	129.78	0.001293
12	93.79	41.18	24.88	132.91	0.001325
13	101.60	40.96	24.89	135.29	0.001348
14	109.27	40.63	24.91	138.19	0.001377
15	117.37	39.42	24.92	151.20	0.001507
16	124.58	37.26	24.94	181.10	0.001805
17	132.43	33.94	24.96	255.09	0.002542
18	140.67	33.85	24.92	256.43	0.002556
19	148.74	34.47	24.80	234.47	0.002337
20	157.27	34.10	24.57	237.74	0.002369
21	164.86	33.75	24.22	240.12	0.002393
22	170.62	34.42	23.85	215.71	0.002150
23	177.31	35.79	23.79	186.52	0.001859
24	185.42	38.06	23.85	155.45	0.001549
25	193.00	34.63	24.04	212.85	0.002121
26	200.41	32.13	24.16	292.88	0.002919
27	208.60	31.89	24.24	305.06	0.003040
28	217.46	32.24	24.29	293.45	0.002925
29	223.89	32.51	24.30	284.53	0.002836
30	231.42	32.72	24.31	278.42	0.002775
31	239.23	33.00	24.32	271.99	0.002711
32	246.95	33.35	24.40	264.18	0.002633
33	255.10	33.57	24.40	257.50	0.002566
34	262.48	33.75	24.41	254.10	0.002532
35	269.70	33.95	24.40	249.13	0.002483
36	277.68	34.10	24.41	245.36	0.002445
37	283.57	34.41	24.40	237.79	0.002370
38	293.75	34.61	24.35	231.19	0.002304
39	300.97	33.25	24.38	292.93	0.002919

File:	HTC300				
Ptot	97382	Pa	Ts,in	296.20	K
Ttot	24.78	C	Re,ex	523626	
Ma,in	0.0524		q"	1791.7	W/m2
Ma,ex	0.1712		Tu,in	0.124	
Ps,in	97195	Pa	Lu,in	31.6	mm
Ps,ex	95410	Pa	U0,in	19.53	m/s

#	Surface (mm)	T surf (C)	T aw (C)	h (W/m2-C)	St
1	10.96	39.09	24.58	85.97	0.001291
2	18.87	40.29	24.61	99.95	0.001501
3	26.07	40.19	24.63	105.49	0.001584
4	32.97	40.06	24.65	107.83	0.001619
5	40.15	40.51	24.67	105.47	0.001584
6	48.16	40.79	24.71	103.24	0.001550
7	55.63	40.97	24.73	102.70	0.001542
8	64.28	41.24	24.74	101.32	0.001522
9	71.09	41.52	24.74	99.63	0.001496
10	77.95	41.62	24.76	99.44	0.001493
11	86.01	41.75	24.77	99.02	0.001487
12	93.79	41.45	24.77	101.54	0.001525
13	101.60	41.21	24.80	103.62	0.001556
14	109.27	40.81	24.80	106.17	0.001594
15	117.37	39.47	24.81	117.34	0.001762
16	124.58	37.18	24.82	142.29	0.002137
17	132.43	33.90	24.81	199.62	0.002998
18	140.67	33.77	24.79	202.04	0.003034
19	148.74	34.33	24.74	186.81	0.002805
20	157.27	34.05	24.65	190.80	0.002865
21	164.86	33.84	24.51	194.58	0.002922
22	170.62	34.66	24.37	175.49	0.002635
23	177.31	36.06	24.35	150.46	0.002260
24	185.42	38.66	24.36	120.80	0.001814
25	193.00	36.38	24.43	146.62	0.002202
26	200.41	33.28	24.48	209.82	0.003151
27	208.60	32.76	24.51	224.64	0.003373
28	217.46	33.08	24.53	216.49	0.003251
29	223.89	33.39	24.55	209.48	0.003146
30	231.42	33.64	24.56	204.55	0.003072
31	239.23	33.97	24.57	199.12	0.002990
32	246.95	34.35	24.60	192.57	0.002892
33	255.10	34.59	24.60	187.53	0.002816
34	262.48	34.81	24.59	184.15	0.002765
35	269.70	35.03	24.60	180.81	0.002715
36	277.68	35.24	24.59	177.22	0.002661
37	283.57	35.53	24.59	172.59	0.002592
38	293.75	35.78	24.58	167.43	0.002514
39	300.97	34.57	24.58	211.20	0.003172

File:	HTCS100				
Ptot	95220	Pa	Ts,ex	294.55	K
Ttot	25.72	C	Re,ex	791033	
Ma,in	0.0810		q"	2257.3	W/m2
Ma,ex	0.2708		Tu,in	0.083	
Ps,in	94784	Pa	Lu,in	43.4	mm
Ps,ex	90490	Pa	U0,in	29.29	m/s

#	Surface (mm)	T surf (C)	T aw (C)	h (W/m2-C)	St
1	10.96	40.72	25.27	107.39	0.001073
2	18.87	42.18	25.32	117.02	0.001169
3	26.07	42.12	25.38	122.88	0.001227
4	32.97	41.99	25.44	125.83	0.001257
5	40.15	42.56	25.51	122.92	0.001228
6	48.16	42.96	25.58	120.01	0.001199
7	55.63	43.19	25.64	119.40	0.001193
8	64.28	43.53	25.68	117.90	0.001178
9	71.09	43.89	25.68	115.64	0.001155
10	77.95	44.04	25.72	115.39	0.001153
11	86.01	44.22	25.76	114.87	0.001147
12	93.79	43.89	25.80	118.10	0.001180
13	101.60	43.64	25.82	120.34	0.001202
14	109.27	43.21	25.84	123.53	0.001234
15	117.37	41.66	25.85	137.33	0.001372
16	124.58	39.03	25.84	168.35	0.001682
17	132.43	35.40	25.82	238.36	0.002381
18	140.67	35.25	25.79	241.13	0.002408
19	148.74	35.83	25.68	222.39	0.002221
20	157.27	35.41	25.43	226.55	0.002263
21	164.86	35.02	25.09	229.99	0.002297
22	170.62	35.71	24.74	207.37	0.002071
23	177.31	37.18	24.70	178.67	0.001785
24	185.42	40.26	24.77	141.05	0.001409
25	193.00	37.11	24.92	182.01	0.001818
26	200.41	33.21	25.06	287.04	0.002867
27	208.60	32.82	25.14	304.66	0.003043
28	217.46	33.23	25.18	290.42	0.002901
29	223.89	33.55	25.20	280.17	0.002798
30	231.42	33.79	25.22	273.63	0.002733
31	239.23	34.09	25.23	266.80	0.002665
32	246.95	34.48	25.31	258.62	0.002583
33	255.10	34.72	25.31	252.21	0.002519
34	262.48	34.92	25.31	247.98	0.002477
35	269.70	35.16	25.31	242.93	0.002426
36	277.68	35.32	25.30	239.01	0.002387
37	283.57	35.69	25.30	230.76	0.002305
38	293.75	35.94	25.25	224.11	0.002238
39	300.97	34.54	25.25	282.62	0.002823

File:	HTCS200				
Ptot	97212	Pa	Ts,ex	297.31	K
Ttot	25.89	C	Re,ex	517309	
Ma,in	0.0523		q"	1781.6	W/m2
Ma,ex	0.1702		Tu,in	0.080	
Ps,in	97026	Pa	Lu,in	43.4	mm
Ps,ex	95265	Pa	U0,in	19.27	m/s

#	Surface (mm)	T surf (C)	T aw (C)	h (W/m2-C)	St
1	10.96	41.34	25.72	76.50	0.001159
2	18.87	42.69	25.74	90.07	0.001364
3	26.07	42.61	25.76	95.34	0.001444
4	32.97	42.49	25.79	97.46	0.001476
5	40.15	42.97	25.82	95.48	0.001446
6	48.16	43.32	25.85	93.16	0.001411
7	55.63	43.54	25.87	92.56	0.001402
8	64.28	43.87	25.88	91.22	0.001382
9	71.09	44.19	25.87	89.54	0.001356
10	77.95	44.30	25.88	89.43	0.001355
11	86.01	44.43	25.90	89.22	0.001352
12	93.79	44.06	25.89	91.85	0.001391
13	101.60	43.77	25.90	93.85	0.001422
14	109.27	43.26	25.92	96.77	0.001466
15	117.37	41.64	25.92	108.36	0.001641
16	124.58	39.03	25.93	133.56	0.002023
17	132.43	35.54	25.92	188.06	0.002849
18	140.67	35.36	25.91	191.18	0.002896
19	148.74	35.89	25.85	177.77	0.002693
20	157.27	35.59	25.76	181.85	0.002755
21	164.86	35.36	25.62	185.89	0.002816
22	170.62	36.17	25.49	168.64	0.002555
23	177.31	37.63	25.47	144.57	0.002190
24	185.42	40.91	25.48	110.66	0.001676
25	193.00	39.63	25.53	120.77	0.001829
26	200.41	34.60	25.58	205.43	0.003112
27	208.60	33.80	25.63	227.57	0.003447
28	217.46	34.19	25.64	216.95	0.003286
29	223.89	34.57	25.65	207.88	0.003149
30	231.42	34.89	25.66	201.53	0.003053
31	239.23	35.30	25.67	194.99	0.002954
32	246.95	35.69	25.75	189.45	0.002870
33	255.10	35.97	25.75	184.14	0.002789
34	262.48	36.23	25.75	180.30	0.002731
35	269.70	36.49	25.74	176.35	0.002671
36	277.68	36.73	25.74	172.68	0.002616
37	283.57	37.07	25.74	167.52	0.002538
38	293.75	37.38	25.70	161.62	0.002448
39	300.97	36.16	25.69	203.28	0.003079

File:	HTG100				
Ptot	94263	Pa	Ts,ex	299.96	K
Ttot	27.22	C	Re,ex	778606	
Ma,in	0.0821		q"	2152.9	W/m2
Ma,ex	0.2708		Tu,in	0.0775	
Ps,in	93819	Pa	Lu,in	13.6	mm
Ps,ex	89579	Pa	U0,in	30.51	m/s

#	Surface (mm)	T surf (C)	T aw (C)	h (W/m2-C)	St
1	10.96	41.31	26.93	110.76	0.001119
2	18.87	42.49	26.97	122.39	0.001236
3	26.07	42.44	27.03	128.11	0.001294
4	32.97	42.36	27.07	130.63	0.001320
5	40.15	42.82	27.14	127.99	0.001293
6	48.16	43.16	27.21	125.27	0.001265
7	55.63	43.31	27.26	125.29	0.001266
8	64.28	43.60	27.29	123.65	0.001249
9	71.09	43.92	27.29	121.31	0.001225
10	77.95	43.96	27.33	121.83	0.001231
11	86.01	44.10	27.35	121.21	0.001224
12	93.79	43.75	27.35	124.68	0.001259
13	101.60	43.46	27.38	127.68	0.001290
14	109.27	43.07	27.38	130.90	0.001322
15	117.37	41.70	27.41	145.16	0.001466
16	124.58	39.33	27.43	178.06	0.001799
17	132.43	35.96	27.47	256.64	0.002593
18	140.67	35.88	27.41	256.85	0.002595
19	148.74	36.47	27.29	234.38	0.002368
20	157.27	36.13	27.06	237.34	0.002398
21	164.86	35.80	26.73	239.85	0.002423
22	170.62	36.50	26.36	213.73	0.002159
23	177.31	37.90	26.30	182.96	0.001848
24	185.42	40.67	26.37	145.78	0.001473
25	193.00	37.00	26.55	204.22	0.002063
26	200.41	34.14	26.68	298.52	0.003016
27	208.60	34.01	26.76	306.58	0.003097
28	217.46	34.43	26.81	291.05	0.002940
29	223.89	34.73	26.84	281.36	0.002842
30	231.42	34.97	26.86	274.85	0.002776
31	239.23	35.26	26.86	267.50	0.002702
32	246.95	35.64	26.94	259.13	0.002618
33	255.10	35.86	26.96	252.94	0.002555
34	262.48	36.05	26.97	249.30	0.002518
35	269.70	36.27	26.96	243.93	0.002464
36	277.68	36.43	26.96	240.01	0.002425
37	283.57	36.77	26.96	232.10	0.002345
38	293.75	37.01	26.91	224.65	0.002269
39	300.97	35.70	26.91	284.01	0.002869

File:	HTG200				
Ptot	96031	Pa	Ts,ex	298.80	K
Ttot	27.36	C	Re,ex	506077	
Ma,in	0.0534		q"	1761.5	W/m2
Ma,ex	0.1696		Tu,in	0.075	
Ps,in	95840	Pa	Lu,in	11.0	mm
Ps,ex	94123	Pa	U0,in	19.41	m/s

#	Surface (mm)	T surf (C)	T aw (C)	h (W/m2-C)	St
1	10.96	42.46	27.29	78.41	0.001210
2	18.87	43.66	27.29	93.13	0.001437
3	26.07	43.58	27.31	98.40	0.001518
4	32.97	43.54	27.34	99.85	0.001540
5	40.15	43.92	27.36	98.13	0.001514
6	48.16	44.24	27.39	96.00	0.001481
7	55.63	44.38	27.41	95.93	0.001480
8	64.28	44.68	27.43	94.57	0.001459
9	71.09	45.00	27.43	92.77	0.001431
10	77.95	45.01	27.45	93.28	0.001439
11	86.01	45.17	27.46	92.74	0.001431
12	93.79	44.81	27.48	95.46	0.001473
13	101.60	44.48	27.49	97.87	0.001510
14	109.27	43.99	27.50	100.84	0.001556
15	117.37	42.44	27.49	112.90	0.001742
16	124.58	39.88	27.50	139.82	0.002157
17	132.43	36.48	27.50	199.25	0.003074
18	140.67	36.37	27.47	200.79	0.003098
19	148.74	36.94	27.42	185.46	0.002861
20	157.27	36.69	27.34	188.89	0.002914
21	164.86	36.49	27.21	192.65	0.002972
22	170.62	37.38	27.06	172.41	0.002660
23	177.31	38.88	27.05	146.40	0.002259
24	185.42	41.99	27.08	113.14	0.001745
25	193.00	39.77	27.12	134.83	0.002080
26	200.41	35.77	27.19	213.07	0.003287
27	208.60	35.29	27.22	226.70	0.003497
28	217.46	35.76	27.25	214.46	0.003309
29	223.89	36.13	27.27	206.14	0.003180
30	231.42	36.42	27.28	200.41	0.003092
31	239.23	36.81	27.28	194.12	0.002995
32	246.95	37.22	27.30	186.93	0.002884
33	255.10	37.49	27.32	181.97	0.002807
34	262.48	37.74	27.31	178.27	0.002750
35	269.70	37.99	27.31	174.50	0.002692
36	277.68	38.22	27.29	170.70	0.002633
37	283.57	38.55	27.30	166.07	0.002562
38	293.75	38.87	27.29	159.88	0.002467
39	300.97	37.60	27.31	203.59	0.003141

REPORT DOCUMENTATION PAGE

Form Approved
OMB No. 0704-0188

1. AGENCY USE ONLY (*Leave blank*)	2. REPORT DATE	3. REPORT TYPE AND DATES COVERED
	November 1994	Final Contractor Report

4. TITLE AND SUBTITLE

Experimental Study of Vane Heat Transfer and Aerodynamics at Elevated Levels of Turbulence

5. FUNDING NUMBERS

WU-505-62-10
C-NAS3-25950

6. AUTHOR(S)

Forrest E. Ames

7. PERFORMING ORGANIZATION NAME(S) AND ADDRESS(ES)

Allison Gas Turbine
Division of GMC
P.O. Box 420
Indianapolis, Indiana 46206-0420

8. PERFORMING ORGANIZATION REPORT NUMBER

E-9203

9. SPONSORING/MONITORING AGENCY NAME(S) AND ADDRESS(ES)

National Aeronautics and Space Administration
Lewis Research Center
Cleveland, Ohio 44135-3191

10. SPONSORING/MONITORING AGENCY REPORT NUMBER

NASA CR-4633

11. SUPPLEMENTARY NOTES

Project Manager, G. James Van Fossen, Internal Fluids Mechanics Division, NASA Lewis Research Center, organization code 2630, (216) 433-5892.

12a. DISTRIBUTION/AVAILABILITY STATEMENT

Unclassified - Unlimited
Subject Category 34

12b. DISTRIBUTION CODE

13. ABSTRACT (*Maximum 200 words*)

A four vane subsonic cascade was used to investigate how free stream turbulence influences pressure surface heat transfer. A simulated combustor turbulence generator was built to generate high level (13%) large scale (Lu ≈ 44% inlet span) turbulence. The mock combustor was also moved upstream to generate a moderate level (8.3%) of turbulence for comparison to smaller scale grid generated turbulence (7.8%). The high level combustor turbulence caused an average pressure surface heat transfer augmentation of 56% above the low turbulence baseline. The smaller scale grid turbulence produced the next greatest effect on heat transfer and demonstrated the importance of scale on heat transfer augmentation. In general, the heat transfer scaling parameter $U_\infty Tu_\infty Lu_\infty^{-1/3}$ was found to hold for the turbulence. Heat transfer augmentation was also found to scale approximately on $Re_{cx}^{1/3}$ at constant turbulence conditions. Some evidence of turbulence intensification in terms of elevated dissipation rates were found along the pressure surface outside the boundary layer. However, based on the level of dissipation and the resulting heat transfer augmentation, the amplification of turbulence has only a moderate effect on pressure surface heat transfer. The flow field turbulence does drive turbulent production within the boundary layer which in turn causes the high levels of heat transfer augmentation. Unlike heat transfer, the flow field straining was found to have a significant effect on turbulence isotropy. On examination of the one dimensional spectra for u' and v', the effect to isotropy was largely limited to lower wavenumber spectra. The higher wavenumber spectra showed little or no change. The high level large scale turbulence was found to have a strong influence on wake development. The free stream turbulence significantly enhanced mixing resulting in broader and shallower wakes than the baseline case. High levels of flow field turbulence were found to correlate with a significant increase in total pressure loss in the core of the flow. Documenting the wake growth and characteristics provide boundary conditions for the downstream rotor.

14. SUBJECT TERMS	15. NUMBER OF PAGES
Turbulence; Gas turbine heat transfer; Vane aerodynamics	125
	16. PRICE CODE: A06

17. SECURITY CLASSIFICATION OF REPORT	18. SECURITY CLASSIFICATION OF THIS PAGE	19. SECURITY CLASSIFICATION OF ABSTRACT	20. LIMITATION OF ABSTRACT
Unclassified	Unclassified	Unclassified	